Computational Discovery of Solid Electrolytes for Batteries: Interfacial Phenomena and Ion Mobility

by

Kwangnam Kim

A dissertation submitted in partial fulfillment
of the requirements for the degree of
Doctor of Philosophy
(Mechanical Engineering)
in the University of Michigan
2020

Doctoral Committee:

Professor Donald J. Siegel, Chair
Professor Wei Lu
Associate Professor Jeff Sakamoto
Assistant Professor Liang Qi

Kwangnam Kim

kwangnam@umich.edu

ORCID iD: 0000-0003-1149-1733

To 보람, Selena 소월, and Lucia 소휘

Acknowledgements

First of all, I would like to express my sincere gratitude to my advisor Professor Donald J. Siegel for his guidance, patience, and support. He has always welcomed and encouraged me whenever I encountered difficulties during research. His great mentorship enables me to keep moving forward step by step; without which I could not accomplish my PhD work. Also, I am very grateful to my committee members, Professors Wei Lu, Jeff Sakamoto, and Liang Qi, who provided incredibly valuable comments and generous service to my dissertation.

I would like to thank all my colleagues in the Energy Storage and Materials Science (ESMS) Lab. Their precious knowledge and experience gave me insights to make breakthroughs. I would like to give special thanks to Dr. Seungho Yu, who provided academic help for me for more than 10 years, not only for my MS in Korea but also for applying to graduate school and PhD study at the University of Michigan. Also, I thank all Korean friends who enjoyed the Ann Arbor life with me. Especially, I would like to express my great thanks to Dr. Taehoon Han who has been willing to be my mental mentor at the hardest times and Dr. Jeongyong Choi and his family for being my family's best friends.

I am grateful for financial support from the Joint Center for Energy Storage Research (JCESR), an Energy Innovation Hub funded by the U.S. Department of Energy, Office of Science, and Basic Energy Sciences. It was a great opportunity to work with JCESR collaborators from various institutes with different backgrounds.

Most of all, I would like to express my deepest gratitude and admiration to my parents for their endless support and encouragement. Also, I would like to express my infinite thankfulness to my wife Boram; I am greatly indebted to her extreme support and countless sacrifices throughout my entire PhD process. Finally, thank you Selena and Lucia for your smiles.

Table of Contents

List of Tables

List of Figures

Abstract

Solid-state batteries (SSBs) using a solid electrolyte (SE) and Li-metal anode are promising technologies that can increase energy density and minimize safety concerns for applications such as electric vehicles. Although the recent discovery of SEs with high ionic conductivity has advanced the prospects for realizing SSBs, additional study of these materials has unearthed several shortcomings (e.g., interfacial degradation). Thus, the discovery of alternative SE remains an important pursuit. This search has been slowed, however, by incomplete understanding of the elementary features that give rise to high ionic mobility and promote interfacial stability.

In response, this dissertation focuses on several topics that are relevant for the advancement of SSBs: (1) stability and wettability at interfaces between a SE and metal anode, (2) fundamental understanding of ionic transport mechanisms in solids, and (3) the discovery of new SEs. These topics are investigated using first-principles calculations. Anti-perovskites (AP) are adopted as model SEs because they have shown promise for achieving high ionic conductivities while possessing simple structures that enable a comprehensive characterization of their properties. In addition, machine learning (ML) is employed to analyze trends in the computed data.

Investigation of the Li_3OCl/Li interface shows that an oxygen-terminated interface is the most stable. This interface exhibits strong interfacial bonds, suggesting good wettability by Li, low interfacial resistance, and potential for Li dendrite prevention. However, this strong interaction also locally shifts the electronic band edge positions, narrowing the bandgap by 30%. Nevertheless, the conduction band minimum remains more negative than the Li/Li^+ potential, implying stability against charge injection from the anode. These calculations indicate a tradeoff between strong interfacial bonding/wettability and electrochemical stability.

Next, the connections between ion mobility, thermodynamic stability, and symmetry-lowering lattice distortions are characterized across 36 model APs. Compounds with larger lattice distortions exhibit smaller percolating migration barriers because these distortions speed up

migration along a subset of pathways. As larger distortions also correlate with reduced stability, realizing high ionic mobility requires balancing a mobility/stability tradeoff. Li_3SeF, Na_3SeF, Na_3SBr, Na_3SF, K_3SeF, and K_3SBr are identified as new compositions that balance this tradeoff. Differences in ion mobilities across Li, Na, and K based APs is rationalized in terms of differences in ion packing, vibrational frequency, polarizability, and ionic charge.

Next, using data generated for alkali metal-based APs, ML is used to identify elementary features that correlate with ionic mobility. Lattice structure was found to have a greater influence in ion transport than do features based on chemical or electronic properties. For vacancy migration, the migration distance and bottleneck-size are the most important features: migration barriers decrease with shorter hops and with wider migration channels. Therefore, tuning the structure of a SE is the most effective scheme to improve ion mobility in these compounds.

Finally, potential multivalent MV-ion SEs based on the AP structure are examined. SEs with compositions Mg_3NAs, Ca_3NAs, and Ca_3PSb are identified as the most promising. These compounds are predicted to be thermodynamically stable, electronically insulating, stable in contact with metal anodes, and to have relatively low percolating barriers for ion migration. Due to their high formation energies, ionic defects should be introduced artificially.

In total, this study enhances understanding of interfacial phenomena and ion transport in solid electrolytes, while also suggesting new materials. The ultimate goal is to accelerate the introduction of SSBs with improved safety and energy density.

Chapter 1 Introduction

1.1 Motivation

Since the Industrial Revolution, the dramatic increase in the use of fossil fuels has been significantly increasing the CO_2 emission, resulting in the global warming and climate change.[1] The high demand for environmentally friendly renewable energy sources leads to the increasing interest in technologies like wind, solar, tidal, and geothermal energies.[2] However, these technologies have limitations associated with their variable output in time as well as location; thus, energy storage has emerged as a technology that can enable their widespread adoption.[3]

Batteries are one of the most promising energy storage technologies due to their high conversion efficiency and essentially zero emissions.[3] Li-ion batteries (LIBs) have high energy densities and voltages, which lead to their wide use in portable electronic devices.[3,4] Na and K-ion batteries (NIBs and KIBs) are being explored for grid energy storage due to the abundance and low price of Na and K.[4–6] Although at the very early stage of development, multivalent (MV) ions Be, Mg, Ca, Zn, and Al have potential to increase the volumetric capacity of batteries.[7]

Nevertheless, additional improvements in battery technologies are highly desirable – especially related to cost, safety, energy density, and life cycle – to enable widespread application to emerging applications such as electric vehicles.[3] The increase in energy density is required for longer-lasting batteries. The longest driving range among commercial electric vehicles is 390 miles of Tesla Model S with the starting price of $80,000 in early 2020, but Jaguar XF (2.0L diesel engine) can drive up to 731 miles with the price of $52,500 in 2019.[8,9] Comparing different models of Ford 2018 Focus, the driving range and price of an electric version is 115 miles and $29,120, whereas cheaper 'SE Hatch' model ($20,540) can drive up to 471 miles.[10] Enhanced safety is also one of the most sought-after performance improvements LIBs for reliable operations. There have been several explosion and fires from batteries of electric devices and vehicles, including a case of Tesla Model X that caught fire after a crash in 2018.[11]

1.2 Solid Electrolytes for Performance Improvements

Safety concerns in commercial LIBs can originate from the use of liquid electrolytes. These electrolytes have high ionic conductivity, yet are volatile and flammable; moreover, they are amenable to dendrite formation, resulting in internal short-circuiting.[3,12,13] Thus, improvements in cell designs and/or materials that address these safety concerns are desirable. In principle, the use of a solid electrolyte (SE) can circumvent these problems.[3,14–16] SEs are less flammable, non-volatile, and less-sensitive to changes in temperature.[3,16,17] Also, the high stiffness exhibited by some SEs has been projected to suppress dendrite formation.[14] This latter benefit presents the possibility to significantly increase the capacity of the negative electrode by substituting metallic lithium for lithiated carbon.[18] The advantages of SEs may lead to the realization of solid-state Li-metal batteries that are longer-lasting and safer than existing LIBs.

1.3 Challenges in Solid Electrolytes

Electrolytes for batteries are required to have high ionic conductivities at least 10^{-4} S/cm.[3] Historically, the ionic conductivity of solids has been insufficient to supplant liquid electrolytes. Very recently, however, a small-but-growing number of solids with ionic conductivities comparable to that of liquids have been identified, including garnet $Li_7La_3Zr_2O_{12}$,[19] argyrodite Li_6PS_5Br,[20] LISICON-like $Li_{10}GeP_2S_{12}$ and $Li_{9.54}Si_{1.74}P_{1.44}S_{11.7}Cl_{0.3}$,[21,22] LiPON $Li_{2.9}PO_{3.3}N_{0.46}$,[23] LPS glass $75Li_2S•25P_2S_5$,[24] NASICON-like $Li_{1.3}Al_{0.3}Ti_{1.7}(PO_4)_3$,[25] perovskite $Li_{0.34}La_{0.51}TiO_{2.94}$,[26] NASICON $Na_3Zr_2Si_2PO_{12}$,[27] glass-ceramic Na_3PS_4,[28] Na sulfides $Na_{10}SnP_2S_{12}$ and $Na_{11}Sn_2PS_{12}$,[29,30] complex hydrides $Na_2(BH_4)(NH_2)$, $LiCB_{11}H_{12}$, and $NaCB_{11}H_{12}$,[31,32] and beta alumina (β"-Al_2O_3) conducting numerous cations like Na, Ag, K, Li, and Rb. The discovery of these fast ion conductors has advanced the prospects for realizing solid-state batteries (SSBs).[13,33] Nevertheless, subsequent investigations on these SE have shown that a high ionic conductivity alone is insufficient for realizing a viable solid-state cell. These materials, in essentially all cases, are not stable with electrode materials, have very low viable voltages, and/or show dendrite penetrations.[34–37] Therefore, the discovery of alternative SE remains an important pursuit. The discovery of new SEs, however, has been slowed due to a lack of fundamental understanding of fast ion transport in solids. Current SEs have mostly been discovered by trial-and-error Edisonian

approaches. Thus, it is desirable to understand important features that describe a high ion mobility in solids for the systematic design of SEs.

1.3.1 Ion Mobility in Solids

A fundamental question in the identification of new SEs is 'what chemical, mechanical, and/or structural features promote high ion mobility?'[38–41] Recent studies suggested several features that may have effects on the ion transport.[38,40,42–46] Lower phonon frequencies enhances the phonon amplitude and assist the jump of mobile ions.[42] Also, fast Li conductors have low Li vibration frequencies.[43] Increasing polarizability of halide anion (from Cl to I in Group 17) softens the lattice, resulting in lower activation energy of ion migration (argyrodite system as an example).[44] The migration barrier is influenced by the preferred insertion site and the anion coordination preference of cations in intercalation host structures; for example, barriers can increase when a cation has a preferred anion coordination at a preferred insertion site.[45] Low energy barriers can be achieved by adopting the bcc framework because it allows a direct hopping between tetrahedral sites.[38] Also, larger volume per anion can decrease the energy barrier.[38,40,46]

Although previous literature has been improving our understanding of ion transport in solids, individual studies do not explicitly explain the relative importance between features. It is also probable that some important properties might be veiled so far. Therefore, a comprehensive analysis is required to establish the design principles for fast ion-conducting solids. This is a challenging goal because it is believed that several features are entangled and affect to ionic motions simultaneously.[47]

1.3.2 Interfacial Properties

Interfacial interactions of SEs with electrodes are critical for battery performance and life time.[47] Two examples of important interfacial properties involving SE are stability[3,34,48–50] and wettability.[51–53] Insufficient interfacial stability manifests though the formation of new phases (from reactions between the SE and electrode, or through decomposition of the SE itself) or through electron transfer between the electrode and SE. Both processes can yield undesirable outcomes. In the former case, the product phases can limit Li-ion mobility and thus increase interfacial resistance.[48,49] In the latter mechanism, electron transfer to/from the SE can precipitate

additional chemical reactions or impart undesirable electrical conductivity to the SE: for example, reduction of a SE by the negative electrode can inject electrons into the conduction band.[54,55]

Figure 1.1 presents an energy level diagram for a SE and the electrodes in a battery.[3,54] To minimize electron transfer to/from a SE, the anode electrochemical potential, μ_A, should be located below (i.e., at a lower energy than) the conduction band minimum (CBM) of the SE, while the electrochemical potential of the cathode, μ_C, should be at a higher energy than the SE's valence band maximum (VBM). Prior studies have demonstrated that these levels can be predicted computationally for an interface-free (i.e., bulk) SE, providing an estimate of a SE's susceptibility to undesirable electron transfer.[46,55,56] Nevertheless, the electrochemical window of an electrolyte can be influenced by interfacial interactions with the electrodes. For example, a previous report revealed that the highest occupied molecular orbital (HOMO) and lowest unoccupied molecular orbital (LUMO) levels of electrolyte solvent molecules shift due to interactions with electrode surfaces, narrowing the electrochemical window relative to that of the isolated molecules.[54] To the best of our knowledge, the impact of interface interactions on the CBM/VBM positions of a SE have not been reported.

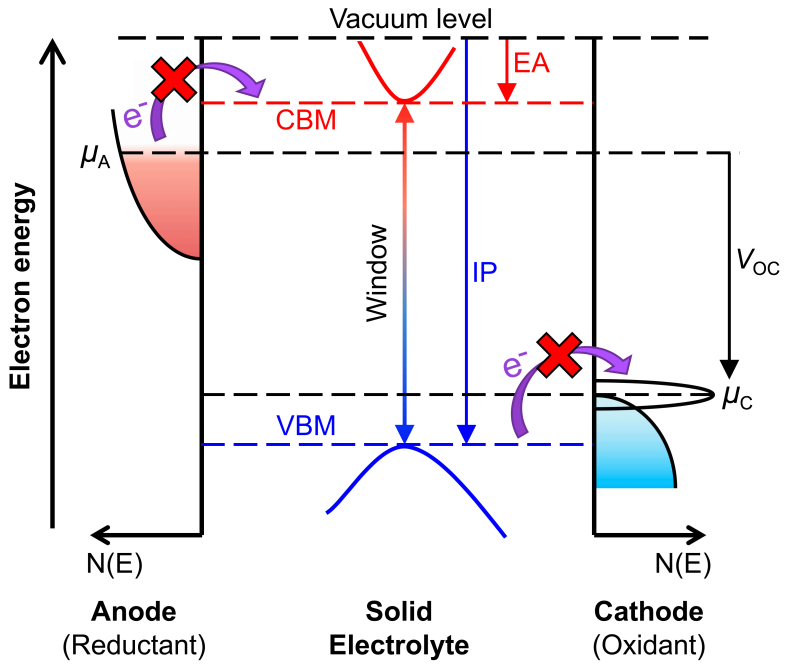

Figure 1.1 Energy levels of a SE with respect to the density of states, N(E), of the electrodes. Red and blue bands represent the conduction and valence bands of the SE, respectively. The electrolyte is susceptible to reduction by the anode when the electrochemical potential of the anode, μ_A, is located at a higher energy than the conduction band minimum, CBM, of the SE. Similarly, oxidation of the SE can occur when the energy of the valence band maximum, VBM, is higher than the electrochemical potential of the cathode, μ_C. The open circuit voltage (V_{OC}), ionization potential (IP), and electron affinity (EA) are also shown.

Regarding interfacial bonding, recent studies have identified the wettability of a SE by Li metal as a key factor in predicting performance.[57,58] Low wettability results in poor contact between Li and a SE, resulting in current focusing, high interfacial resistance, and/or dendrite formation.[51,52,59–61] For $Li_7La_3Zr_2O_{12}$, improved wetting by Li can be achieved through interface coatings[51,59,62,63] or surface cleaning treatments.[53,60] Despite the importance of wettability to SE performance, few computational studies of wettability have been reported.[53]

1.4 Anti-perovskite Compounds

The anti-perovskite (AP) system was recently suggested as SE.[64,65] APs adopt the well-known structure of the perovskites, but interchange the positions of the anions and cations. APs of interest for SEs adopt the formula X_3AB, where X is a monovalent cation and A and B are anions with respective charges of 2- and 1-. The AP crystal structure consists of vertex-sharing X_6A octahedra (A anion at the octahedron center) enclosed by a cubic framework with B anions at vertices of cubic (space group 221; Pm-3m), so A and B form a bcc framework and X are at the center of the cubic face. APs have high alkali-ion contents and large band gaps as well as high ionic conductivities. Included in these candidates is the so-called 'Li-rich' AP, Li_3OCl (LOC, Figure 1.2), which exhibits a high ionic conductivity of ~10^{-3} S/cm at room temperature and was predicted to have a very large band gap over 6 eV.[64,66] A LOC-based cell with a graphitic anode and $LiCoO_2$-based cathode operates at voltages up to 4.2 V.[67] Also, a Li/LOC/Li symmetric cell and SEM images show that LOC is stable and compatible with a Li-metal anode.[67,68]

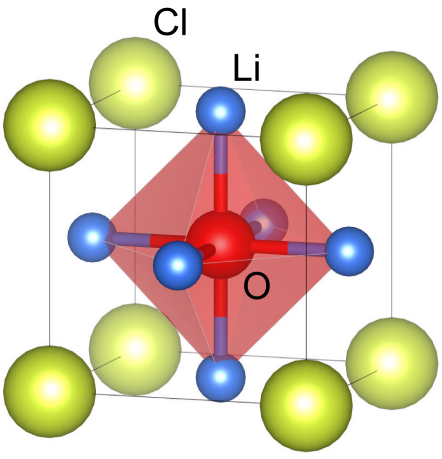

Figure 1.2 Unit cell of anti-perovskite Li_3OCl in the cubic Pm-3m structure. Cl ions form the cubic framework and enclose Li_6O octahedron.

Previous studies have described two mechanisms for Li-ion transport in LOC.[56,66,69–72] These include a vacancy mechanism involving Li-ion hop ing along the edges of the Li-octahedra, Figure 1.3(a),[56] and hopping of a Li interstitial dumbbell, Figure 1.3(b).[66] The interstitial process has a barrier that is roughly half that of the vacancy mechanism.[66] The relative importance of these mechanisms remains a matter of debate. Mouta et al. suggested that Li vacancies are responsible for the high conductivity in pristine and divalent-metal doped LOC, owing to their higher vacancy concentration compared to Li interstitials.[69] On the other hand, interstitials were predicted to dominate in samples synthesized under LiCl-deficient conditions,[70] where an elevated concentration of oxygen substitutional defects on Cl-sites (O'_{Cl}) is anticipated. Others have argued, however, that the high binding energy between Li interstitials and O'_{Cl}, will hinder interstitial hopping.[71] In addition, Stegmaier et al. have proposed that Li vacancies are present in LOC near the cathode, whereas Li interstitials dominate near the interface with the anode.[72]

Composition variation has been explored as a means to increase the ionic conductivity of AP SEs. For example, the mixed-halogen phase, $Li_3OCl_{0.5}Br_{0.5}$, exhibits a conductivity that is approximately twice that of LOC at room temperature.[56,64] Zhao et al. proposed that this is due to a wider channel for Li-ion migration, which was made possible by an enlarged unit cell.[64] Similarly, a computational study reported that Cl–Br substitutional disorder results in a spectrum of activation barriers, with some barriers being lower than those in LOC and Li_3OBr (LOB).[66] Deng et al. predicted $Li_3OCl_{0.75}Br_{0.25}$ to be the optimal mixed phase, with maximum ionic

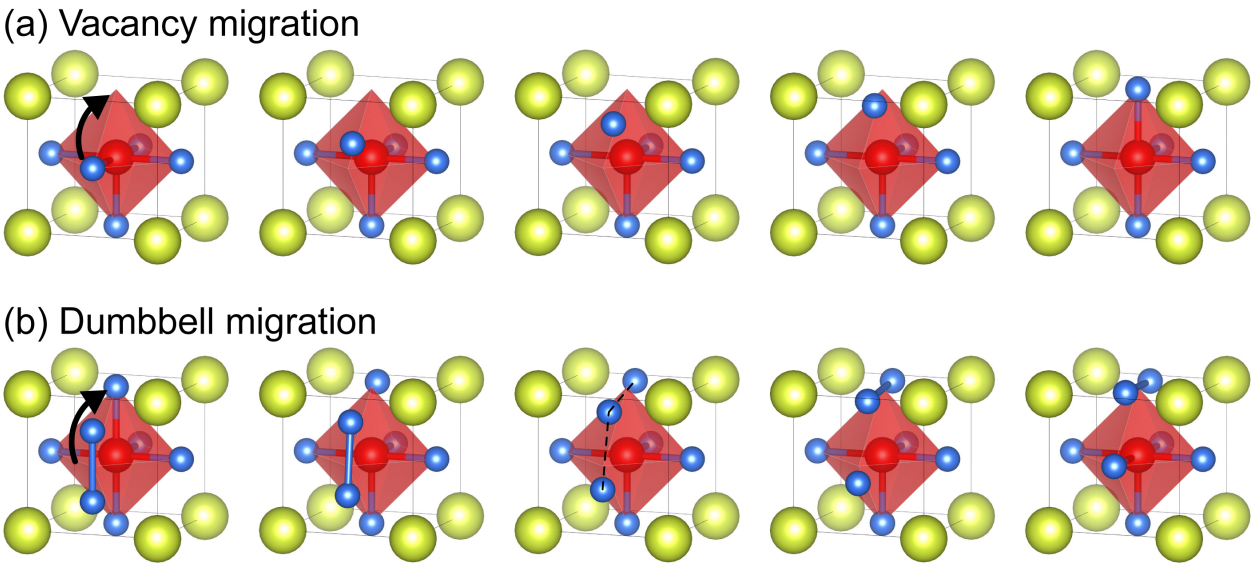

Figure 1.3 Migration mechanisms for (a) vacancies and (b) interstitial dumbbells.

conductivity.[73] The sodium analogues of LOC – Na_3OCl (NOC), Na_3OBr (NOB), Na_3OI (NOI), and their respective mixed-halogen phases – have also been synthesized.[65] Of these, $Na_3OBr_{0.6}I_{0.4}$ was reported to have a higher conductivity than either NOC or NOB.[65] Several other strategies have also been explored to increase the ionic conductivity of the APs.[65,74,83–85,75–82]

Previous density functional theory calculations predicted that LOC and LOB are thermodynamically unstable at zero Kelvin, i.e., they are prone to decompose into lithium chalcogenide and halide.[56,66] Following studies revealed that LOC becomes stable at elevated temperatures around 500 K.[81,86] Chen et al. suggested that vibrational entropies are contributed by Li – Cl bonds in LOC that are softer than the bonds in LiCl.[86,87] Thus, other AP compounds with moderate instabilities might also be stabilized at elevated temperatures. Stabilized metastable phases at certain thermodynamic conditions (e.g., high temperatures or pressures) can be kinetically retained at metastable conditions.[88]

1.5 Goals and Scope of Dissertation

As discussed in this chapter, additional improvements in battery technologies are driven by demanding applications: the increase in energy density and enhanced safety. The development of SSBs using a SE with a metal anode will be the key to solve these problems. To address this topic, this dissertation focuses on the interfacial phenomena at interfaces between Li metal and SEs, fundamental understanding of ion transport in inorganic solid materials, and the discovery of potential compounds for monovalent and MV-ion conducting SEs for secondary batteries, using the AP lattice system. First-principles calculations and machine learning approaches were used to perform atomic-scale simulations and feature engineering.

Chapter 3 investigates the interfacial interaction at Li metal/SE interfaces using LOC as a model SE. The wettability and electrochemical stability at the interfaces were examined. Chapter 4 reveals the connections between ionic mobility, thermodynamic stability, and symmetry-lowering lattice distortions across a series of 36 model APs, and suggests potential Li, Na, and K-ion conducting AP SEs. Descriptors that characterize the difference in mobilities between Li, Na, and K ions in solids will also be discussed. Chapter 5 delves deeper into systematic understanding of chemical, physical, and structural features that describe the ion transport in solids. Machine learning (ML) approaches will be used with a large number of ion-migration data to find effective

features, their relative importance, and how they promote a high ion mobility. Finally, Chapter 6 explores MV-ion containing APs and suggests possible compounds for SEs of MV-ion SSBs.

In total, this study aims to improve our understanding of interfacial phenomena and ion transport in solids, while also suggesting new candidate SEs for SSBs. The ultimate goal is to accelerate the design of optimal SEs for use in safe and long-lasting SSBs.

Chapter 2 Methodology

2.1 First-principles Calculations

2.1.1 Many-body Problem

The Schrödinger equation is the wave equation that describes the quantum-mechanical behaviors of quantized particles given by[89]

$$i\hbar\frac{d\Psi}{dt} = \hat{H}\Psi, \tag{2.1}$$

where $\hbar$ is the reduced Planck constant, Ψ is the many-body wave function, and $\hat{H}$ is the Hamiltonian operator. In the non-relativistic assumption, the Hamiltonian can be expressed as

$$\hat{H} = -\frac{\hbar^2}{2m}\nabla^2 + V(\mathbf{r}, t), \tag{2.2}$$

where m is the mass of particle. The first and the other terms are the operators for kinetic and potential energies, respectively. In the time-independent system with electrons and nuclei, the wave function is a function of positions particles as

$$\Psi = \Psi(\mathbf{r}_1, \mathbf{r}_2, \cdots, \mathbf{r}_n; \mathbf{R}_1, \mathbf{R}_2, \cdots, \mathbf{R}_N), \tag{2.3}$$

where **r** and **R** are position vectors of electrons and nuclei, respectively. The wave equation can be further simplified with the Born-Oppenheimer (BO) approximation which enables the separate treatment between electrons and nuclei.[90] Proton is about 1800 times heavier than electron (by rest mass), thus nuclei will have much slower motions than electrons. In other words, electrons are always at the ground state with respect to the potential energy surface arisen by nuclei at fixed positions.[91] Nuclei will be treated classically and only electrons will behave quantum-mechanically under this approximation. Consequently, the electron wave equation in the time-

independent non-relativistic system with electrons and nuclei under the BO approximation becomes

$$\hat{H}\Psi = E\Psi, \tag{2.4}$$

where E is the total energy of the system, and the wave function and Hamiltonian (in atomic unit) are

$$\Psi = \Psi(\mathbf{r}_1, \mathbf{r}_2, \cdots, \mathbf{r}_n), \tag{2.5}$$

$$\hat{H} = -\frac{1}{2}\sum_{i=1}^{n} \nabla_i^2 + \sum_{i=1}^{n}\sum_{j=1}^{N} \frac{-Z_j}{|\mathbf{R}_j - \mathbf{r}_i|} + \sum_{i=1}^{n}\sum_{j>i}^{n} \frac{1}{|\mathbf{r}_j - \mathbf{r}_i|}. \tag{2.6}$$

The equation is now a function of only electron positions; the kinetic energy of nuclei is neglected and the Coulomb interaction energy between nuclei can be treated separately. The terms in the Hamiltonian are, in order, the kinetic energy of electrons, the Coulombic interaction between nuclei and electrons, and the Coulombic interaction between electrons.

2.1.2 Non-interacting Electron Approximation

The exact solution of the wave function can be achievable only for single-particle problems like a hydrogen atom.[92] It is even impossible to solve it numerically with the increased number of particles.[93] To solve many-body problems, Hartree assumed the independent electron approximation with an *ansatz* that the wave function can be expressed by the product of orthonormal single-electron wave functions (Hartree product) as[94–96]

$$\Psi(\mathbf{r}_1, \mathbf{r}_2, \cdots, \mathbf{r}_n) = \psi_1(\mathbf{r}_1)\psi_2(\mathbf{r}_2)\cdots\psi_n(\mathbf{r}_n). \tag{2.7}$$

This approximation significantly reduces the complexity that the $3n$-dimension wave equation becomes n number of 3-dimension wave equations for each electron,

$$\hat{H}_i\psi_i = E_i\psi_i, \tag{2.8}$$

where E_i is the energy of electron *i*. Each electron is assumed to interact with the mean field, i.e., electron density $\rho(\mathbf{r}) = \sum_i \psi_i^*(\mathbf{r}_i)\psi_i(\mathbf{r}_i)$, which replaces the electron-electron interaction term in the Hamiltonian to the Hartree potential expressed as

$$V_{\mathrm{H}}(\mathbf{r}) = \sum_{i=1}^{n} \int \frac{\psi_i^*(\mathbf{r}')\psi_i(\mathbf{r}')}{|\mathbf{r} - \mathbf{r}'|} d\mathbf{r}' \,. \tag{2.9}$$

The single-electron wave equations can be solved by the self-consistent field (SCF) iterative method. Initial single-electron wave functions can be used to solve the equations (2.8) and obtain new wave functions which will be used as trial inputs in the next iterative step. The iteration will be implemented until the wave functions and energies of electrons converge.

The Hartree method is a very valuable achievement since it is one of the earliest approaches to solve many-body problems. However, there are several defects to describe real systems due to its oversimplification:[93] The non-interacting assumption omits the repulsive Coulomb interaction between particles with different spins (i.e., correlation energy). The self-interaction is included in the total energy because all electrons contribute to the electron density. Also, this method does not obey the Pauli exclusion principle and the antisymmetry principle, thus it fails to include the exchange interaction between identical particles with the same spin and does not include the exchange energy (the total system energy will be higher than the exact value).[97,98] The Hartree-Fock (HF) method solves this problem by improving the wave function with the Slater determinant as[99]

$$\Psi(\mathbf{r}_1, \mathbf{r}_2, \cdots, \mathbf{r}_n) = \frac{1}{\sqrt{n!}} \begin{vmatrix} \psi_1(\mathbf{r}_1) & \psi_2(\mathbf{r}_1) & \cdots & \psi_n(\mathbf{r}_1) \\ \psi_1(\mathbf{r}_2) & \psi_2(\mathbf{r}_2) & \cdots & \psi_n(\mathbf{r}_2) \\ \vdots & \vdots & \ddots & \vdots \\ \psi_1(\mathbf{r}_n) & \psi_2(\mathbf{r}_n) & \cdots & \psi_n(\mathbf{r}_n) \end{vmatrix}. \tag{2.10}$$

For example, $\Psi(\mathbf{r}_1, \mathbf{r}_2) = [\psi_1(\mathbf{r}_1)\psi_2(\mathbf{r}_2) - \psi_2(\mathbf{r}_1)\psi_1(\mathbf{r}_2)]/\sqrt{2}$ and so $\Psi(\mathbf{r}_1, \mathbf{r}_2) = -\Psi(\mathbf{r}_2, \mathbf{r}_1)$, thus it satisfies the antisymmetry principle. Also, the wave function becomes zero when two electrons occupy the same spin orbital, i.e., $\Psi(\mathbf{r}_1, \mathbf{r}_1) = 0$, thus it also satisfies the Pauli exclusion principle. Therefore, the HF method includes the exchange energy. Also, the exchange energy automatically cancels out the self-interaction energy. However, this improved method still cannot include the correlation energy and the calculation is complicated to deal with large systems.

2.1.3 Density Functional Theory

The density functional theory (DFT) is a SCF iterative method with the non-interacting electron approximation and can simulate many-body systems much larger than the HF limit by

virtue of the Hohenberg-Kohn (HK) theorems.[100] The first theorem is that *the ground-state energy of the system is a unique functional of the electron density*. In other words, the ground-state electron density uniquely determines all properties, including the energy and wave function at the ground state.[91] Next, the second theorem states that *the electron density that minimizes the energy functional is the true electron density that corresponds to the solution of the Schrödinger equation*. Therefore, we can use the variational principle to find the ground state of electrons iteratively.

Based on the HK theorem, Kohn and Sham suggested the formula for the energy functional as[101]

$$E[\rho(\mathbf{r})] = -\frac{1}{2}\sum_{i=1}^{n}\psi_i^*(\mathbf{r}_i)\nabla^2\psi_i(\mathbf{r}_i) + \int V_{\text{ext}}(\mathbf{r})\rho(\mathbf{r})d\mathbf{r} + \frac{1}{2}\iint\frac{\rho(\mathbf{r})\rho(\mathbf{r}')}{|\mathbf{r}-\mathbf{r}'|}d\mathbf{r}d\mathbf{r}' + E_{\text{XC}}[\rho(\mathbf{r})], \quad (2.11)$$

where the first term is the sum of kinetic energies of independent electrons (different from the kinetic energy of the real system), the second term is the classical Coulomb interaction energy between electron and the external potential V_{ext} arisen by stationary nuclei, the third term is the classical Coulomb interaction energy between electrons (i.e., Hartree energy E_{H}), and the last term is the exchange-correlation (XC) energy. This last term contains all quantum-mechanical behavior of electron, i.e., exchange and correlation energies as well as the kinetic energy error.[102] The Kohn-Shan (KS) equation can be derived from the energy functional, i.e.,

$$\left\{-\frac{1}{2}\nabla^2 + V_{\text{ext}}(\mathbf{r}) + V_{\text{H}}[\rho(\mathbf{r})] + V_{\text{XC}}[\rho(\mathbf{r})]\right\}\psi_i(\mathbf{r}) = E_i\psi_i(\mathbf{r}), \quad (2.12)$$

where

$$V_{\text{H}}[\rho(\mathbf{r})] = \frac{\delta E_{\text{H}}[\rho(\mathbf{r})]}{\delta\rho(\mathbf{r})} = \int\frac{\rho(\mathbf{r}')}{|\mathbf{r}-\mathbf{r}'|}d\mathbf{r}', \quad (2.13)$$

$$V_{\text{XC}}[\rho(\mathbf{r})] = \frac{\delta E_{\text{XC}}[\rho(\mathbf{r})]}{\delta\rho(\mathbf{r})}. \quad (2.14)$$

The SCF iteration can be implemented with trial initial electron density to calculate single-electron wave functions using the equation (2.12). The wave functions can be used to calculate the new electron density that will be used in the next step. The iteration can be terminated if the electron density as well as the total energy converges.

2.1.4 Exchange-Correlation Functional

The difficulty of DFT comes from the XC energy functional, $E_{\mathrm{XC}}[\rho(\mathbf{r})]$, whose exact form is unknown. Thus, the accuracy of DFT simulations depends on the validity of the functional form. The functional can be expressed as[101,102]

$$E_{\mathrm{XC}}[\rho(\mathbf{r})] = \{T[\rho(\mathbf{r})] - T_0[\rho(\mathbf{r})]\} + \int \varepsilon_{\mathrm{XC}}[\rho(\mathbf{r})]\rho(\mathbf{r})d\mathbf{r}\,, \tag{2.15}$$

where $T[\rho(\mathbf{r})]$ and $T_0[\rho(\mathbf{r})]$ are the exact and non-interacting kinetic-energy functionals and $\varepsilon_{\mathrm{XC}}[\rho(\mathbf{r})]$ is the XC energy functional per electron. The XC energy can be decomposed as $E_{\mathrm{XC}} = E_{\mathrm{X}} + E_{\mathrm{C}}$. Note that $T[\rho(\mathbf{r})]$ is unknown whereas $T_0[\rho(\mathbf{r})]$ is already discussed above, and the difference between them is the correction to the kinetic energy. The simplest form of the XC functional is the local-density approximation (LDA) that uses the analytic solution of the homogeneous electron gas (HEG).[101] It assumes that the local distribution of electrons is uniform with a certain density, like a mosaic art with small pieces of different colors. The exact solutions of the kinetic energy and exchange energy ($\varepsilon_{\mathrm{X}}^{\mathrm{LDA}}$) of HEG are known,[103–105] and the correlation energy ($\varepsilon_{\mathrm{C}}^{\mathrm{LDA}}$) can be determined by empirical models (e.g., Vosko-Wilk-Nusair[106] and Perdew-Wang[107]) parametrized by fitting to the quantum Monte-Carlo simulation result.[108]

More sophisticated XC functional is the generalized gradient approximation (GGA) that also includes the gradient of electron density to the exchange and correlation energies (i.e., semi-local model), which leads to higher accuracy than LDA functionals.[109] One of the most widely used XC functionals is the Perdew-Burke-Ernzerhof (PBE) parametrization model.[110] The brief expression of the GGA-PBE XC functional is

$$E_{\mathrm{XC}}^{\mathrm{PBE}}[\rho(\mathbf{r}); \nabla\rho(\mathbf{r})\,] = \int \varepsilon_{\mathrm{XC}}^{\mathrm{PBE}}[\rho(\mathbf{r});\ \nabla\rho(\mathbf{r})]\rho(\mathbf{r})d\mathbf{r}\,. \tag{2.16}$$

One of the drawbacks of the GGA as well as LDA functionals is the weak electron localization, which results in less accurate predictions of electron structure and narrower band gaps (or even metallic) than actual properties.[111] The hybrid functional suggested by Heyd, Scuseria, and Ernzerhof (HSE) can improve the accuracy by adopting the exact HF exchange energy:[112,113]

$$E_{\mathrm{XC}}^{\mathrm{HSE}} = \alpha E_{\mathrm{X}}^{\mathrm{HF,SR}}(\omega) + (1-\alpha)E_{\mathrm{X}}^{\mathrm{PBE,SR}}(\omega) + E_{\mathrm{X}}^{\mathrm{PBE,LR}}(\omega) + E_{\mathrm{C}}^{\mathrm{PBE}}, \tag{2.17}$$

where SR and LR stand for 'short-range' and 'long-range', respectively, α is the mixing parameter that determines the contribution of the HF exchange energy to the total exchange energy in the short range, and ω is the screening parameter that defines the separation between SR and LR. The HSE06 model with α = 0.25 and ω = 0.2 Å have shown to product good results for many cases. However, the computational cost increases dramatically since the HF calculations should be involved in the computation.

2.1.5 Quasi-particle GW method

It is the inherent nature that the standard DFT cannot correctly describe the excited states of electrons because the DFT formalism is based on the HK theorem that leads to the KS equation with the XC functional designed for the ground-state Hamiltonian and the excited-state functional in general may not have the same dependence on the electron density as it has for the ground state.[114] The higher level of theory than the standard DFT is the quasi-particle GW method based on the many-body perturbation theory with the GW approximation by virtue of Hedin's rigorous theoretical framework.[115] Prior studies have shown that GW calculations yield ionization potentials (IP), electron affinities (EA), and band gaps in good agreement with (inverse) photoemission experiments.[116–120] The quasi-particle energies (i.e., single-particle excitation energies) can be calculated by[111,121]

$$\left\{-\frac{1}{2}\nabla^2 + V_{\text{ext}}(\mathbf{r}) + V_{\text{H}}[\rho(\mathbf{r})]\right\}\psi_i(\mathbf{r}) + \int \sum(\mathbf{r}, \mathbf{r}'; E_i)\psi_i(\mathbf{r}')\boldsymbol{d}\mathbf{r}' = E_i\psi_i(\mathbf{r}), \qquad (2.18)$$

where the non-local and energy-dependent potential $\sum(\mathbf{r}, \mathbf{r}'; E_i)$ is the self-energy containing the effects of exchange and correlations. Within the GW approximation, the self-energy operator can be expressed by[111,115]

$$\sum \approx iGW, \qquad (2.19)$$

where W is the screened coulomb interaction and G is Green's function that describes the propagations of an extra/missing electron. Detail descriptions of the self-energy operator can be found in the literature.[111,121] The operator is expressed by the wave function and quasi-particle energies, thus the SCF iteration can be implemented for the GW method. The standard DFT is used to obtain the single-particle wave functions and energies, which can be used as initial guesses of quasi-particle wave-functions and energies to solve the equation (2.18) iteratively. There are

many types of GW methods based on the iteration scheme: non-self-consistent G_0W_0 and (partially) self-consistent GW_0 and GW calculations, where the subscription 0 means that the designated term is not updated but fixed on the KS DFT level of theory. In this study, the eigenvalues are updated while the wave functions are kept fixed.[116]

2.2 Phonons and Thermodynamics

2.2.1 Harmonic Approximation

Phonon is the elastic wave that propagates through solid lattices due to vibrational thermal excitations of atoms.[122,123] The vibrations can be described by atoms connected by springs with force constants. The potential energy can be expressed by the Taylor expansion around the equilibrium with small displacements as[87,123]

$$\Phi = \Phi_0 + \sum_{li\alpha} \left.\frac{\partial \Phi}{\partial d_{i\alpha}^{l}}\right|_0 d_{i\alpha}^{l} + \frac{1}{2}\sum_{li\alpha}\sum_{l'j\beta} \left.\frac{\partial^2 \Phi}{\partial d_{i\alpha}^{l}\partial d_{j\beta}^{l'}}\right|_0 d_{i\alpha}^{l} d_{j\beta}^{l'} + \cdots, \tag{2.20}$$

where Φ_0 is the equilibrium potential energy and $d_{i\alpha}^{l}$ is the displacement along direction α of atom i in the unit cell l. The second term is zero at the equilibrium since it is the first-order derivative of the total energy. The truncation of the series above the second-order term leads to the harmonic approximation (HA), assuming that atomic vibrations are on the parabolic potential-energy surface within small perturbations near its equilibrium position. The second-order derivative in the equation (2.20) is the force constant matrix

$$\Gamma_{\alpha\beta}\binom{j\ \ j'}{l\ \ l'} = \left.\frac{\partial^2 \Phi}{\partial d_{i\alpha}^{l}\partial d_{j\beta}^{l'}}\right|_0, \tag{2.21}$$

which describes a set of the force constants between an atom j in the unit cell l the other atom j' in the unit cell l' within HA. This matrix can be converted to the dynamical matrix by the Fourier transform as[123,124]

$$D_{\alpha\beta}(jj', \mathbf{q}) = \frac{1}{\sqrt{M_j M_{j'}}}\sum_{l\,l'} \Gamma_{\alpha\beta}\binom{j\ \ j'}{l\ \ l'} \exp\{-i\mathbf{q}\cdot[\boldsymbol{x}(jl) - \boldsymbol{x}(jl)]\}, \tag{2.22}$$

where M_j is the mass of the atom j and $\mathbf{q}$ is the phonon wave vector. The phonon modes can be obtained by solving the eigenvalue problem for the dynamical matrix by diagonalization, i.e., the eigenvalues are the vibrational frequencies of phonon modes.

For insulators with a long-range Coulomb interaction by dipole-dipole contribution (especially ionic solids), the dynamical matrix is non-analytical. Thus, the non-analytic term should also be added in the analytic expression of dynamical matrix (i.e., the form that does not include Coulomb interaction) to account for the splitting between transverse and optical phonons at the Γ-point.[125–127] the dynamical matrix at the Γ-point can be expressed as[124]

$$D_{\alpha\beta}(jj', \mathbf{q} \to \mathbf{0}) = D_{\alpha\beta}(jj', \mathbf{q} = \mathbf{0}) + D^{\mathrm{NA}}_{\alpha\beta}(jj', \mathbf{q} \to \mathbf{0}), \tag{2.23}$$

$$D^{\mathrm{NA}}_{\alpha\beta}(jj', \mathbf{q} \to \mathbf{0}) = \frac{1}{\sqrt{M_j M_{j'}}} \frac{4\pi}{V} \frac{\left(\sum_\gamma q_\gamma Z^*_{j,\gamma\alpha}\right)\left(\sum_{\gamma'} q_{\gamma'} Z^*_{j',\gamma'\beta}\right)}{\sum_{\alpha\beta} q_\alpha \varepsilon^\infty_{\alpha\beta} q_\beta}, \tag{2.24}$$

where the second term in the right-hand side in the equation 2.23 is the non-analytic (NA) term, V is the unit cell volume, $\varepsilon^\infty_{\alpha\beta}$ is the electronic dielectric constant tensor, and $Z^*_{j,\gamma\alpha}$ is the Born effective charge tensor of the atom j. The NA term is treated by the approach that Parlinski et al. suggested.[127]

2.2.2 Vibrational Free Energy

Using the partition function with discrete phonon microstates, the statistical mechanics leads to the vibrational contribution (including zero-point energy) of a harmonic system to the free energy as[128]

$$F_{\mathrm{H}}(T, V) = k_B T \int_0^\infty d\omega \; g(\omega) \; \ln\left[2 \sinh\left(\frac{\hbar\omega}{2k_B T}\right)\right], \tag{2.25}$$

where k_{B} is the Boltzmann constant, $\hbar$ is the Planck constant, and the integral is over all phonon frequencies ω using the phonon density of states (PDOS) $g(\omega)$ at a certain volume V. A small amount of negative frequencies in PDOS, if any, was neglected following a previous analysis.[86] This is due to the well-known dynamical instability in the AP lattice system, due to rotational vibrations of octahedra.[129] The phonon analysis is implemented by the PHONON software[130] using forces and properties obtained by DFT calculations.

2.2.3 Quasi-harmonic Approximation

The quasi-harmonic approximation (QHA) is an extension of the harmonic approximation, which accounts for the thermal expansion of lattice (i.e., the dependence of the phonon modes on the cell volume is explicitly accounted for).[87] The Gibbs free energy within QHA is expressed as:[87,131]

$$G(T,p) = \min_{V}[F(T,V) + pV]\,, \tag{2.26}$$

$$F(T,V) = E_0(V) + F_H(T,V), \tag{2.27}$$

where E_0 is the electronic energy at zero Kelvin (without vibrational contributions) and $\min_{V}[\cdots]$ indicates that G is a minimum with respect to variations in volume V at a specified temperature, T, and pressure, p. The equilibrium volume was found by fitting free energy data as a function of volume to the Murnaghan equation of states (EOS).[132] The pV term is negligible for solid phases;[133] in this case the free energy can be expressed as a function of T and V only.

Chapter 3 Predicting Wettability and the Electrochemical Window of Lithium-Metal/Solid Electrolyte Interfaces

3.1 Introduction

The present chapter investigates stability and wettability at a Li metal/SE interface. The AP LOC is adopted as a model SE.[64] LOC is one example of several AP compositions that have been reported as potential SEs; others include LOB, NOC, NOB, and NOI.[64,65] LOC has a simple crystal structure, making it attractive for computationally-expensive electronic-structure calculations. Furthermore, LOC has been reported to have a high ionic conductivity (~10^3 S/cm), a large band gap implying a wide electrochemical window, and the compatibility with a Li-metal anode.[56,66–68] Nevertheless, there is a lack of fundamental understanding of interface phenomena, especially for stability and wettability, at Li metal/LOC interfaces.

First-principles calculations were used to assess the electronic and thermodynamic properties of Li and LOC surfaces/interfaces. Vibrational contributions to the enthalpy and entropy were evaluated to estimate surface/interface energies at near-ambient temperatures. Interface wettability was characterized according to the Li contact angle on LOC, derived from the Young-Dupré equation and the calculated interfacial work of adhesion. Stability against reduction by the Li electrode was predicted by determining the absolute positions of the band edges of LOC (via GW calculations) in relation to the Li/Li^+ level.

These calculations suggest that the oxygen-terminated Li/LOC interface is the most thermodynamically stable. The calculated work of adhesion implies that Li will wet LOC with a low contact angle, suggesting the possibility for strong interfacial bonding and low interfacial resistance. On the other hand, this strong interfacial interaction significantly narrows the bandgap of LOC in the interfacial region by shifting both the CBM and VBM: in the vicinity of the interface the bulk bandgap of ~8 eV is reduced to ~5.6 eV, implying a tradeoff between strong interfacial bonding/wettability and electrochemical stability. Despite this interface-induced reduction in

electrochemical window, the CBM in LOC remains ~1 V more negative than the Li/Li^+ redox potential, denoting stability against reduction by the anode. In total, the present study demonstrates how first-principles computational methods can be used to comprehensively characterize interfacial properties that are relevant to the operation of SSBs.

3.2 Methodology

3.2.1 First-principles Calculations

DFT calculations were performed using the Vienna *ab initio* Simulation Package (VASP).[134] Exchange-correlation effects were treated within the generalized gradient approximation (GGA), as parameterized by Perdew-Burke-Ernzerhof (PBE).[110] Interactions between core and valence electrons were treated using the projector augmented wave (PAW) method.[135,136] The valence electron configurations were $1s^2 2s$ for Li, $2s^2 2p^4$ for O, and $3s^2 3p^5$ for Cl. A plane-wave basis set with cutoff energy of 550 eV was used for calculations involving ionic relaxations and total-energy evaluations. More computationally-expensive GW calculations (described below) used a 2s valence configuration for Li and a lower cutoff energy of 475 eV. The energy of the electronic ground state was converged to within 10^{-5} eV, and the force criterion for atomic relaxations was set to 0.01 eV/Å. At least a 17 × 17 × 17 k-point sampling is required for BCC Li metal for total energy convergence to within 1 meV at the equilibrium volume, whereas only a 4 × 4 × 4 k-point sampling is needed for bulk Li_3OCl, Li_2O, and LiCl.

Surface energies for LOC were calculated for fully relaxed slab models with 11 layers and within a supercell containing a 12 Å vacuum region. A Γ-centered 4 × 4 × 1 k-point mesh was used for all surface calculations. The effects of number of slab layers (7 – 15 layers) and vacuum thicknesses (6 – 24 Å) were tested; it was determined that the surface energy was well converged using the parameters described above. The work of adhesion was calculated for fully relaxed interface models with 7 layers of LOC and 7 layers of Li. Convergence testing revealed that the work of adhesion did not change significantly upon increasing the number of Li and LOC layers (tests were done with 5 – 13 Li layers and 7 – 23 LOC layers). A Γ-centered 4 × 4 × 1 k-point mesh was also used for interface calculations; this sampling converged the total energy of the interface to within 1 meV/atom. Spin-polarized calculations were used for gas-phase molecules

and for atoms; these systems used a simulation cell of dimensions 10 Å × 11 Å × 12 Å, with reciprocal space sampled at the Γ point.

Free energies were evaluated within the harmonic approximation using the direct method.[137] Atomic displacements of ±0.02 Å and ±0.04 Å were used in conjunction with 3 × 3 × 3 expansions of the conventional unit cells, corresponding to supercells containing 135 atoms for LOC, 54 atoms for BCC Li, 324 atoms for Li_2O, and 216 atoms for LiCl. A Γ-centered 4 × 4 × 4 k-point mesh was used for the Li supercell, whereas a single k-point was used for the other systems. Phonon calculations on slab models of LOC employed a 3 × 3 expansion within the surface plane for (100) surfaces, a 3 × 2 expansion for (110) surfaces, and a 2 × 1 expansion for (111) surfaces. A single k-point was used for these slab models. Interface models used a 2 × 2 expansion within the interfacial plane (dimensions of 15.6 Å × 15.6 Å) and a Γ-centered 2 × 2 × 1 k-point mesh. Convergence testing revealed that increases to system size or the number of k-points did not significantly alter the vibrational properties.

3.2.2 Band Edge Positions

The absolute positions of the VBM and CBM (relative to vacuum) in bulk LOC were obtained following the procedure described in Ref.[138] Figure 3.1 summarizes this approach, which involves aligning the planar averaged electrostatic potential (V_{ref}) in the bulk region of an LOC surface slab

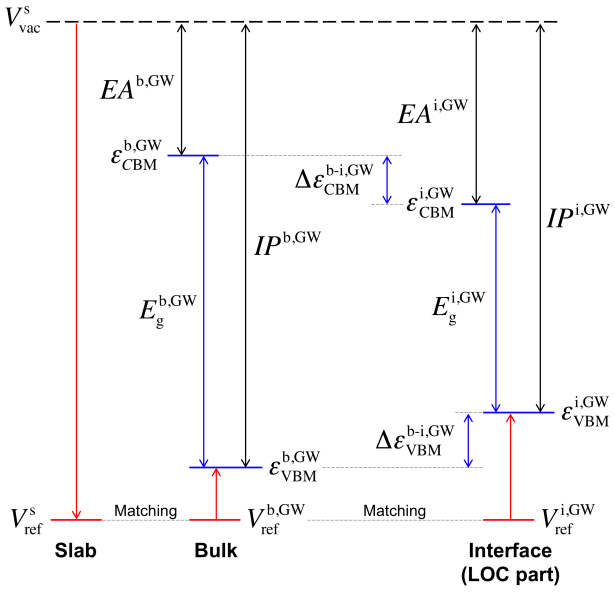

Figure 3.1 Determination of the absolute band edge positions of a solid electrolyte. The method is based on aligning the reference potentials V_{ref} of the slab (s), bulk (b), and interface (i) systems.

with that from a bulk cell.[55,119,120] VBM and CBM positions in the bulk cell (given by $\varepsilon_{\mathrm{VBM}}$ and $\varepsilon_{\mathrm{CBM}}$) are evaluated using GW calculations, while the position of the vacuum level (V_{vac}) is determined from the slab system at a lower level of theory (GGA or HSE06). Aligning the electrostatic potentials in these two systems provides a common reference from which the absolute VBM/CBM positions can be inferred. Following this procedure, the IP of bulk LOC is expressed as:

$$IP^{\mathrm{b,GW}} = (V_{\mathrm{vac}}^{\mathrm{s}} - V_{\mathrm{ref}}^{\mathrm{s}}) - \left(\varepsilon_{\mathrm{VBM}}^{\mathrm{b,GW}} - V_{\mathrm{ref}}^{\mathrm{b,GW}}\right), \tag{3.1}$$

where $V_{\mathrm{vac}}^{\mathrm{s}}$ and $V_{\mathrm{ref}}^{\mathrm{s}}$ are the planar-averaged electrostatic potentials in the vacuum region and at the center of the LOC slab, respectively, and $\varepsilon_{\mathrm{VBM}}^{\mathrm{b,GW}}$ and $V_{\mathrm{ref}}^{\mathrm{b,GW}}$ are the VBM energy and reference electrostatic potential of bulk LOC evaluated with the GW method, respectively. $V_{\mathrm{ref}}^{\mathrm{b,GW}}$ for the bulk cell should be evaluated at an atomic plane similar to that found in the center of the LOC slab. The absolute CBM position (i.e., $EA^{\mathrm{b,GW}}$) can be determined by combining $IP^{\mathrm{b,GW}}$ with the bulk band gap (i.e., $E_{\mathrm{g}}^{\mathrm{b,GW}}$). Since the wavefunctions input to a GW calculation (from a preceding GGA or HSE06 calculation) are unchanged during the GW calculation, the Hartree potential is also unchanged. Thus, the reference potential from the slab supercell (evaluated using the GGA or HSE06 functional) and the bulk (evaluated using GW) can be aligned without difficulty.[119,120]

In a similar fashion, the absolute positions of the LOC band edges can be determined when LOC is interfaced with a Li anode. In this case the electrostatic potential at the center of LOC slab (now a sub-component of the interface supercell) is used as the reference potential (i.e., $V_{\mathrm{ref}}^{\mathrm{i,GW}}$). Band edge shifts are obtained as the difference in VBM or CBM positions between the bulk and interface systems as

$$\Delta\varepsilon_{\mathrm{VBM/CBM}}^{\mathrm{b\text{-}i,GW}} = \left|\varepsilon_{\mathrm{VBM/CBM}}^{\mathrm{i,GW}} - \varepsilon_{\mathrm{VBM/CBM}}^{\mathrm{b,GW}}\right|. \tag{3.2}$$

3.2.3 Gibbs Free Energy

The Gibbs free energy, *G*, for several phases relevant for the Li-O-Cl system was evaluated using the following expression:[139–141]

$$G(T,P) = E(0\ \mathrm{K}) + E^{\mathrm{vib}}(T) + E^{\mathrm{rot}}(T) + E^{\mathrm{trans}}(T) + pV - T\left[S^{\mathrm{vib}}(T) + S^{\mathrm{conf}}(T)\right]. \tag{3.3}$$

Here $E(0\text{ K})$ is the static energy at 0 K (i.e., the DFT total energy) and $E^{\text{vib}}(T)$ is the vibrational energy, including the zero-point energy. For molecular systems, the rotational energy, $E^{\text{rot}}(T)$, translational energy, $E^{\text{trans}}(T)$, and the pV term sum to $\frac{7}{2}k_{\text{B}}T$ ($4k_{\text{B}}T$) for linear (non-linear) molecules, where k_{B} is the Boltzmann constant. These three terms do not significantly contribute to the free energy of solids under the conditions examined here. $S^{\text{vib}}(T)$ and $S^{\text{conf}}(T)$ are the vibrational and configurational entropy; the latter term can be neglected for the ordered solid systems examined here.[133,141] For gas-phase molecules the total entropy $S^{\text{vib}}(T) + S^{\text{conf}}(T)$ was obtained from experimental data.[142] Vibrational contributions to the energy and entropy within the harmonic approximation can be expressed as:[139]

$$E^{\text{vib}}(T) = \sum_i \frac{1}{2}\hbar\omega_i + \hbar\omega_i \left(e^{\frac{\hbar\omega_i}{k_{\text{B}}T}} - 1 \right)^{-1}, \tag{3.4}$$

$$S^{\text{vib}}(T) = k_{\text{B}} \sum_i \frac{\frac{\hbar\omega_i}{k_{\text{B}}T}}{e^{\frac{\hbar\omega_i}{k_{\text{B}}T}} - 1} - \ln\left(1 - e^{-\hbar\frac{\omega_i}{k_{\text{B}}T}}\right), \tag{3.5}$$

where the sums are over vibrational modes ω_i and $\hbar$ is the reduced Planck constant.

The dependence of the chemical potentials of the gas-phase species upon temperature and pressure were evaluated assuming ideal gas behavior:

$$\mu(T, p) = \frac{1}{2}\left[G(T, p^\circ) + k_{\text{B}}T \ln\left(\frac{p}{p^\circ}\right) \right], \tag{3.6}$$

where p° is the standard pressure. The calculated vibrational modes for the various molecular species are 1572 cm^{-1} for O_2, 538 cm^{-1} for Cl_2, 1062, 916, and 424 cm^{-1} for ClO_2 and 642, 577 and 278 cm^{-1} for Cl_2O, are in reasonable agreement with experimental data.[142] Corrections to the chemical potentials of oxygen and chlorine, due to the overbinding tendency of DFT,[143] were done by using empirical binding energy as[144]

$$E_{\text{O}_2 \text{ or } \text{Cl}_2}(0\text{ K}) = 2E_{\text{O or Cl}}(0\text{ K}) + E_{\text{Binding}}, \tag{3.7}$$

where $E_i(0\text{ K})$ on the right side is the DFT energy of species i and E_{Binding} is 5.12 and 2.48 eV at 0 K per O_2 and Cl_2 molecules, respectively.[142] The free energies of compounds and other molecules can be corrected by

$$G_{\mathrm{c,\,X}} = G_{\mathrm{X}} - \Delta G_{\mathrm{c,\,X}}, \tag{3.8}$$

$$\Delta G_{\mathrm{c,\,X}} = \left(G_{\mathrm{X}} - \sum_i n_i^{\mathrm{X}} \mu_i^{\mathrm{ref}}\right) - \Delta G_{\mathrm{f,\,X}}^{\mathrm{expt}}, \tag{3.9}$$

where G_{X} is the predicted Gibbs free energy of a compound or molecule X predicted by DFT calculations, $G_{\mathrm{c,\,X}}$ is the corrected Gibbs free energy, and $\Delta G_{\mathrm{c,\,X}}$ is the correction value, i.e., the difference in formation energies between the prediction $\left(G_{\mathrm{X}} - \sum_i n_i^{\mathrm{X}} \mu_i^{\mathrm{ref}}\right)$ and experiment $\Delta G_{\mathrm{f,\,X}}^{\mathrm{expt}}$ (-5.82/-5.49 eV for Li_2O, -3.98/-3.77 eV for LiCl, 1.09/1.24 eV for Cl_2O and 1.27/1.43 eV for ClO_2, per formula unit at 300/550 K)[142].

3.3 Results and Discussion

3.3.1 Bulk Li_3OCl

Bulk properties. The low-energy structures of LOC, BCC Li, Li_2O, and LiCl were determined at zero Kelvin using the Murnaghan EOS:

$$E(V) = \frac{B_0 V}{B_0'(B_0' - 1)}\left[B_0'\left(1 - \frac{V_0}{V}\right) + \left(\frac{V_0}{V}\right)^{B_0'} - 1\right] + E_0, \tag{3.10}$$

where B_0 is the bulk modulus, B_0' is the pressure derivative of the bulk modulus, V_0 is the equilibrium volume, and E_0 is a constant.

Table 3.1 summarizes the band gap predictions as a function of the calculation method and input wavefunction flavor (based on either a self-consistent GGA or hybrid-functional calculation). Note that GW calculations were preceded by extensive convergence tests by increasing the number of bands, frequency points, and GW steps up to 2024, 256, and 8,

Table 3.1 Calculated band gaps (in eV) for LOC as a function of the calculation method. Two different exchange-correlation functionals – GGA-PBE and HSE06 – were used to generate the input wavefunctions used in the GW calculations.

Wavefunction type	Non-GW	G_0W_0	GW_0	GW
GGA-PBE	4.84	7.29	7.84	8.65
HSE06	6.41	8.04	8.32	8.80

respectively. Of the GW methods reported in Table 3.1, prior studies have shown that the HSE06+G_0W_0 method and the GGA+GW_0 method yield band gaps that are in very good agreement with experiments.[116,117,145] In the case of LOC, these two methods suggest that the band gap lies within the range 7.8 to 8.1 eV. This large bandgap compares favorably with those reported for other solid electrolytes, which are typically smaller: for example, 6.4 eV for $Li_7La_3Zr_2O_{12}$ (HSE06+G_0W_0),[55] 2.1 eV for Li_6PS_5Br (GGA),[146] and 3.7 eV for $Li_{10}GeP_2S_{12}$ (HSE).[46]

Bulk stability. Figure 3.2(a) illustrates the stability range for bulk LOC at 300 K as a function of the chemical potentials for oxygen, $\mu_{\mathrm{O}}^{\mathrm{LOC}}$, and chlorine, $\mu_{\mathrm{Cl}}^{\mathrm{LOC}}$, in LOC. This stability plot was generated by expressing the Gibbs free energy of LOC in terms of the chemical potentials of its constituents, as:

$$G_{\mathrm{Li_3OCl}}^{\mathrm{bulk}} = 3\mu_{\mathrm{Li}}^{\mathrm{LOC}} + \mu_{\mathrm{O}}^{\mathrm{LOC}} + \mu_{\mathrm{Cl}}^{\mathrm{LOC}}. \tag{3.11}$$

To avoid decomposition of LOC into the elements or binary compounds, the range of allowable values for its chemical potentials must satisfy the following constraints:[147]

$$\begin{aligned}
\mu_{\mathrm{Li}}^{\mathrm{LOC}} &\leq G_{\mathrm{Li}}^{\mathrm{BCC\ bulk}} = \mu_{\mathrm{Li}}^{\mathrm{ref}} \\
\mu_{\mathrm{O}}^{\mathrm{LOC}} &\leq 0.5 G_{\mathrm{O_2}}^{\mathrm{gas}} = \mu_{\mathrm{O}}^{\mathrm{ref}} \\
\mu_{\mathrm{Cl}}^{\mathrm{LOC}} &\leq 0.5 G_{\mathrm{Cl_2}}^{\mathrm{gas}} = \mu_{\mathrm{Cl}}^{\mathrm{ref}} \\
2\mu_{\mathrm{Li}}^{\mathrm{LOC}} + \mu_{\mathrm{O}}^{\mathrm{LOC}} &\leq G_{\mathrm{Li_2O}}^{\mathrm{bulk}} \\
\mu_{\mathrm{Li}}^{\mathrm{LOC}} + \mu_{\mathrm{Cl}}^{\mathrm{LOC}} &\leq G_{\mathrm{LiCl}}^{\mathrm{bulk}} \\
x\mu_{\mathrm{Cl}}^{\mathrm{LOC}} + y\mu_{\mathrm{O}}^{\mathrm{LOC}} &\leq G_{\mathrm{Cl}_x\mathrm{O}_y}^{\mathrm{gas}},
\end{aligned} \tag{3.12}$$

where the superscript "ref" refers to standard conditions, and Cl_xO_y refers to Cl_2O and ClO_2 gases at STP.[142] $\mu_{\mathrm{Li}}^{\mathrm{LOC}}$ can be eliminated in the equation (3.12) using the equation (3.11), allowing the constraints to be expressed only as functions of $\mu_{\mathrm{O}}^{\mathrm{LOC}}$ and $\mu_{\mathrm{Cl}}^{\mathrm{LOC}}$.

The narrow blue region in Figure 3.2(a) identifies the range of chemical potentials (satisfying the above constraints) for which LOC is stable at 300 K and 1 atm. Four constraints define the region's boundaries: at the left and right edges two parallel lines demark decomposition into Li_2O and LiCl, while boundaries above and below mark the chemical potentials at which decomposition into O_2 gas or to Li metal is expected. Red lines and arrows in Figure 3.2(a) indicate the chemical potential values at which other decomposition products are predicted to form.

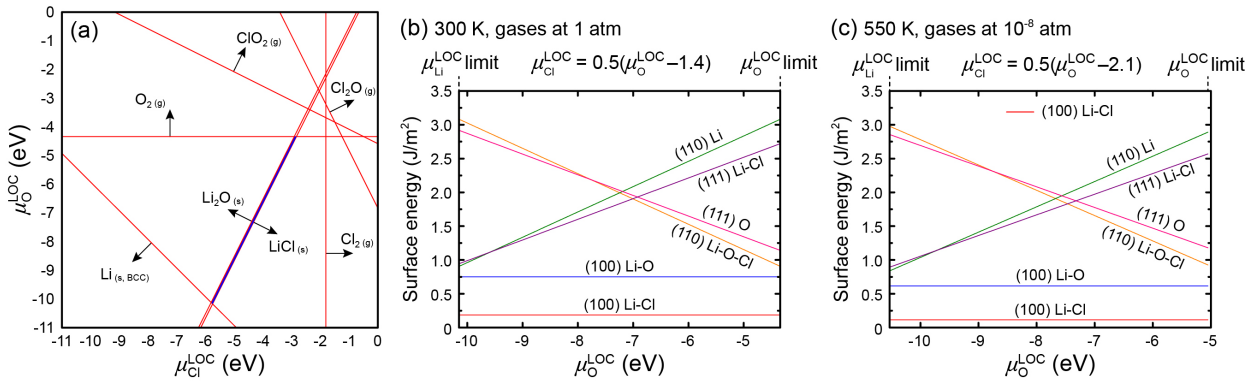

Figure 3.2 (a) Stability of bulk LOC at 300 K and 1 atm as a function of the chemical potentials of oxygen (μ_O^{LOC}) and chlorine (μ_{Cl}^{LOC}) in LOC. The thin blue region indicates the combination of chemical potentials that satisfy the thermodynamic constraints in the equation (3.12), resulting in the stability of LOC. Outside of this region LOC is expected to decompose into other phases; red lines and arrows indicate boundaries in chemical potential space where other phases are predicted to form. (b-c) Calculated surface energies of LOC as a function of chemical potential of oxygen at 300 K and 1 atm [panel (b), STP] and at 550 K and 10^{-8} atm [panel (c), comparable to the synthesis conditions of LOC]. In the surface energy plots the chemical potentials μ_{Cl}^{LOC} and μ_O^{LOC} are related by the equation (3.12), and are restricted to the range determined in panel (a) for which LOC is stable with respect to decomposition.

Although not shown, the stability range for LOC at 550 K and 10^{-8} atm, conditions typical for its synthesis,[64] is very similar to that shown in Figure 3a at 300 K and 1 atm.

The combination of chemical potential values [parallel lines in Figure 3.2(a)] that bound the stability regime of LOC can be expressed generally as $\mu_O^{LOC} - 2\mu_{Cl}^{LOC} = C$, where C is a constant. At 300 K and 1 atm LOC is stable for $1.39 \leq \mu_O^{LOC} - 2\mu_{Cl}^{LOC} \leq 1.42$. Since the stability region is very narrow, μ_O^{LOC} and μ_{Cl}^{LOC} can be related by assuming $C = 1.4$, e.g., $\mu_{Cl}^{LOC} = 0.5(\mu_O^{LOC} - 1.4)$. With this approximation, the constraints in the equation (3.12) can be expressed only in terms of μ_O^{LOC}.

3.3.2 Li_3OCl Surface Modeling

The stability of 6 low-index surfaces of LOC were examined (Figure 3.3): two (100) surfaces, one with Li-Cl termination and one with Li-O termination; two (110) surfaces, one terminated by Li, and one terminated by a plane containing all of Li, O, and Cl; and two (111) surfaces, one with Li-Cl termination and one O-termination. To ensure both surfaces of each LOC slab were identical, it was necessary to construct non-stoichiometric slabs. The surface energy was evaluated as

$$\sigma = \frac{1}{A}\left(G_{\text{Slab}} - \sum_i n_i^{\text{slab}} \mu_i^{\text{LOC}}\right), \tag{3.13}$$

where A is the surface area, G_{Slab} is the Gibbs free energy of the slab supercell, n_i^{slab} is the number of atoms of type i in the slab, and μ_i^{LOC} is the chemical potential of species i in bulk LOC. The chemical potential of Li ($\mu_{\text{Li}}^{\text{LOC}}$) in the above expression for σ can be eliminated using the Gibbs

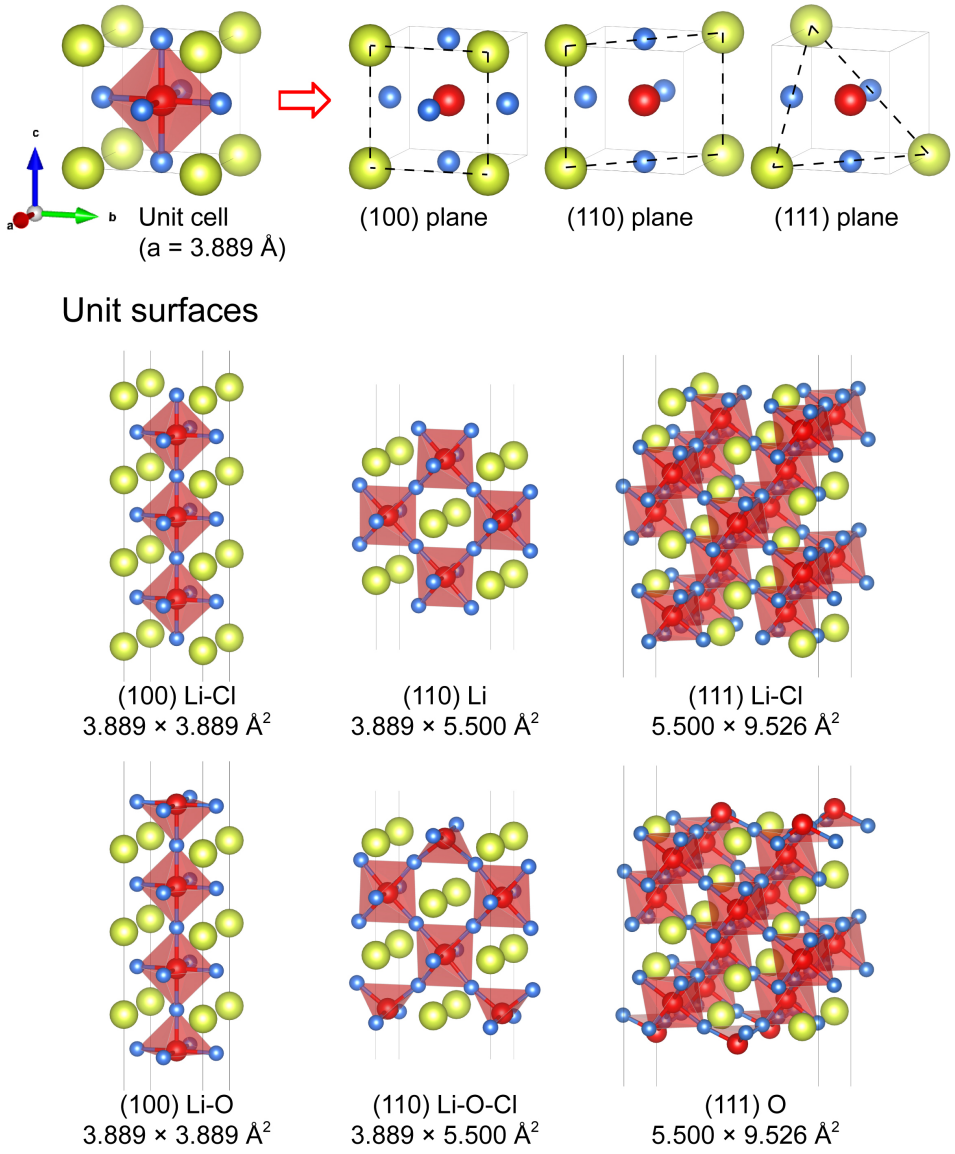

Figure 3.3 (Top) Cleavage planes used to construct Li_3OCl surfaces. Each plane has two possible surface terminations. (Bottom) Configurations of the elementary surface slab models. The name of surface consists of its cleavage plane and terminating species, e.g., the surface (100) Li-Cl is cleaved along the (100) plane and is terminated by a plane containing Li and Cl ions. Surface area is also shown. Truncation of the Li_6O octahedra occurs when O ions are exposed on the surface (bottom three slabs).

free energy of LOC [the equation (3.11)]; furthermore, the chemical potential of Cl ($\mu_{\mathrm{Cl}}^{\mathrm{LOC}}$) can also be eliminated using the relation $\mu_{\mathrm{Cl}}^{\mathrm{LOC}} = 0.5\left(\mu_{\mathrm{O}}^{\mathrm{LOC}} - C\right)$, so that the surface energy can be expressed as a function of $\mu_{\mathrm{O}}^{\mathrm{LOC}}$:

$$\sigma = \frac{1}{A}\left\{G_{\mathrm{Slab}} - \left[\frac{1}{3}n_{\mathrm{Li}}^{\mathrm{slab}}G_{\mathrm{Li_3OCl}}^{\mathrm{bulk}} - \frac{1}{2}\left(n_{\mathrm{Cl}}^{\mathrm{slab}} - \frac{1}{3}n_{\mathrm{Li}}^{\mathrm{slab}}\right)C + \left(n_{\mathrm{O}}^{\mathrm{slab}} + \frac{1}{2}n_{\mathrm{Cl}}^{\mathrm{slab}} - \frac{1}{2}n_{\mathrm{Li}}^{\mathrm{slab}}\right)\mu_{\mathrm{O}}^{\mathrm{LOC}}\right]\right\}, \quad (3.14)$$

where C = 1.4 at 300 K and 1 atm.

Figures 3.2(b) and (c) compare the energies of the six examined surfaces of LOC as a function of oxygen chemical potential at STP [Figure 3.2(b)] and at conditions typical of LOC synthesis [550 K, low pressure, Figure 3.2(c)]. Compared to the (111) and (110) surfaces, the (100) planes have the lowest surface energies regardless of their chemical termination. Calculated surface energies for the (100) surfaces are 0.19 and 0.75 J/m^2 at 300 K, and 0.11 and 0.62 J/m^2 at 500 K, for the Li-Cl and Li-O terminations, respectively. Assuming thermodynamic equilibrium holds, this implies that the (100) surfaces are the most plausible; indeed, the equilibrium crystallite shapes predicted by the Wulff construction and the calculated surface energies exhibit only (100) planes.[148] Given their low energies, the (100) surfaces were adopted for additional interfacial analyses, as described below. Note that surface energies of (100) planes are independent of $\mu_{\mathrm{O}}^{\mathrm{LOC}}$.

3.3.3 Li/Li$_3$OCl Interfaces

Interface modeling. LOC/Li interfaces were constructed by joining either Li-Cl-terminated (100) or Li-O-terminated (100) surfaces of LOC with the (100) surface of Li metal. The minimum-energy interface geometry was determined by searching over a series of rigid displacements of the adjoining slabs in directions within, and normal to, the interface plane. The equilibrium interfacial distance (assuming rigid slabs) was determined by fitting energy vs. interface distance data to the universal binding energy relation (UBER).[149] Starting from this interface distance, all atoms were subsequently fully relaxed to generate the final interface geometry.

Hereafter we refer to the (100) LOC surface or interface with either Li-Cl or Li-O termination as the 'Cl-terminated' or 'O-terminated' surface, respectively. Interfaces involving each of these two LOC surfaces and the (100) surface of BCC Li were modeled to predict the interfacial thermodynamics, wettability, and electrochemical stability of LOC in contact with a Li-

metal anode. The (100) surface of Li has the lowest energy among low-index facets of BCC Li: 29.1, 30.5 and 31.2 meV/Å^2 for (100), (110) and (111) planes similar to previous reports.[150–152] Interfaces were constructed by matching the 2 × 2 Cl- or O-terminated LOC (100) surface to a $\sqrt{5}$ × $\sqrt{5}$ (100) BCC Li surface containing 5 Li atoms per layer. This interfacial orientation relationship minimizes the interfacial strain while allowing for moderate supercell sizes. The Li surface was strained by 1.1% in its in-plane directions to match the dimensions of the LOC slab. The interface models contained 103 and 107 atoms, respectively, for supercells based on Cl- and O-terminated LOC.

To identify the minimum-energy interface geometry, the total energy of the interface was evaluated as a function of displacements within, and normal to, the interface plane. One hundred interfacial displacements in the interfacial plane were sampled using a uniform grid with a 10 × 10 mesh. This grid search was performed at several interlayer distances. In all cases the atom positions were fixed. The interfacial work of adhesion W_{ad} at each interfacial separation, d, was calculated for this 'rigid' interface according to:

$$W_{\text{ad}}(d) = \frac{1}{A}\left[E_{\text{interface}}(d) - \left(E_{\text{Li}_3\text{OCl}} + E_{\text{BCC-Li}}\right)\right], \tag{3.15}$$

where A is the interface area and $E_{\text{interface}}$, E_{LOC} and $E_{\text{BCC-Li}}$ are the total energies of the interface, the isolated LOC slab, and the isolated BCC Li slab, respectively. (The dimensions and the number of layers contained in the isolated slabs were identical to those in the interface system.) The W_{ad} values obtained at different interfacial separations were fit using the UBER:[149]

$$W_{\text{ad}}(d) = -W_{\text{ad}}^0\left(1 + \frac{d - d_0}{l}\right)e^{-(d-d_0)/l}, \tag{3.16}$$

where W_{ad}^0 is the work of adhesion for the rigid interface at the equilibrium separation, d_0, and l is a scaling length. The equilibrium separations for the Cl- and O-terminated interfaces were 3.11 and 2.61 Å, respectively.

Subsequently, all atoms in the interface cells were relaxed starting from interface models positioned at their rigid-body equilibrium interface distances, d_0. These relaxations yield the minimum-energy interface structures. Figure 3.4 shows the interface models that result from this process. The Cl-terminated interface has a relatively undisturbed interfacial structure, which resembles that of bulk Li and LOC. Li_6O octahedra in LOC at this interface remain intact. On the

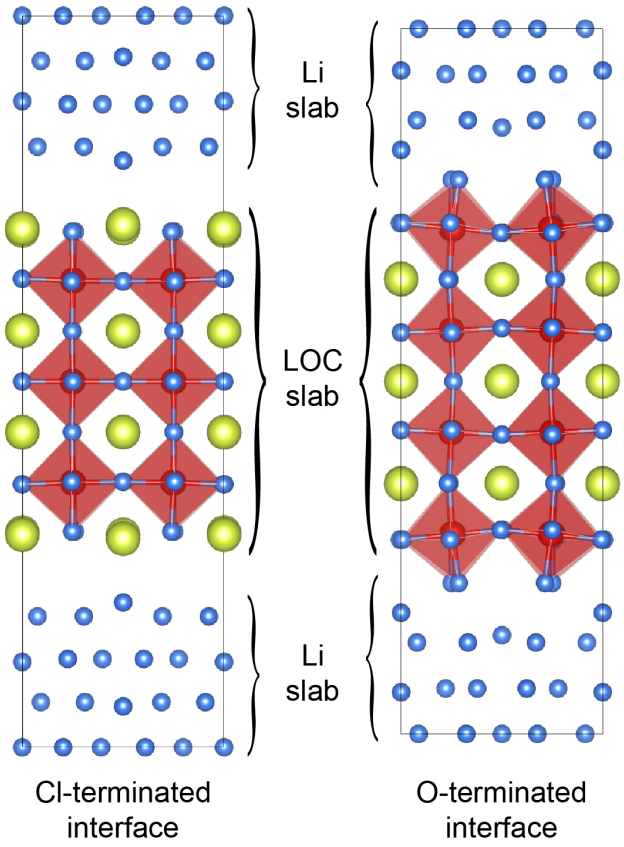

Figure 3.4 Relaxed structure of Cl- and O-terminated interfaces, which consist of 7 layers of LOC (100) and BCC-Li (100) planes (103 and 107 atoms, respectively). The O-terminated interface is shorter in height than the Cl-terminated interface due to shorter interlayer distance. A weak interaction is found at the Cl-terminated interface, whereas O ions strongly attract Li-metal atoms and form octahedron to make up for the missing part at the O-terminated interface.

other hand, large interfacial atomic rearrangements are observed for the O-terminated system. In this case truncated Li_6O octahedra at the interface (these octahedra are missing a Li atom at the octahedron vertex closest to the Li slab) are re-formed by attracting Li atoms from the Li slab. These models were used to calculate thermodynamic properties and the work of adhesion, as described below.

Interface thermodynamics. We first consider the thermodynamic properties of the LOC/Li interface. These are summarized in Table 3.2, and include the interface formation energy, the strain energy, and the interface energy. The interface formation energy, G_f, was calculated as:[153]

$$G_{\mathrm{f}} = G_{\mathrm{Interface}} - n_{\mathrm{Li}}^{\mathrm{Li\ slab}}\mu_{\mathrm{Li}}^{\mathrm{ref}} - \left[\frac{1}{3}n_{\mathrm{Li}}^{\mathrm{LOC\ slab}}G_{\mathrm{Li_3OCl}}^{\mathrm{bulk}} + \left(n_{\mathrm{O}}^{\mathrm{LOC\ slab}} - \frac{1}{3}n_{\mathrm{Li}}^{\mathrm{LOC\ slab}}\right)\mu_{\mathrm{O}}^{\mathrm{LOC}} + \left(n_{\mathrm{Cl}}^{\mathrm{LOC\ slab}} - \frac{1}{3}n_{\mathrm{Li}}^{\mathrm{LOC\ slab}}\right)\mu_{\mathrm{Cl}}^{\mathrm{LOC}}\right], \qquad (3.17)$$

Table 3.2 Calculated Li/LOC interface formation energy, strain energy, and interface energy as a function of interface composition at ambient conditions and at conditions that mimic the temperature and pressure used during synthesis of LOC.

Interface	300 K at 1 atm			550K at 10^{-8} atm		
	Formation energy (eV)	Strain energy (eV)	Interface energy (J/m^2)	Formation energy (eV)	Strain energy (eV)	Interface energy (J/m^2)
Cl-termination	3.80	0.03	0.50	2.84	0.03	0.37
O-termination	3.21	0.03	0.42	2.12	0.03	0.28

where the allowable range of chemical potentials, $\mu_{\mathrm{O}}^{\mathrm{LOC}}$ and $\mu_{\mathrm{Cl}}^{\mathrm{LOC}}$, are the same as in the surface energy calculations. Here, the 2nd and 3rd terms on the right of the above expression [equation (3.17)] refer to the bulk free energies per atom (Li) or per formula unit (LOC) under zero-strain conditions. Thus, the interface formation energy reflects the energetic cost to form the Li/LOC interface from (unstrained) bulk Li and bulk LOC.

At STP, the calculated formation energies of the Cl- and O-terminated interfaces are 3.80 and 3.21 eV, respectively. (To place these values in context, we note that the formation energies of β"-Mg_5Si_6/α-Al interfaces were reported to fall within that range 0.7 – 4.5 eV.[153]) These data indicate that the O-termination is energetically favored compared to the Cl-termination. The relative ordering of the formation energies is the same under conditions that mimic LOC synthesis (2.84 vs. 2.12 eV for Cl- and O-terminations, respectively, Table 3.2). Similar to the surface energies, the interfacial formation energies are constant values, i.e., they are independent of the oxygen chemical potential.

The interface formation energy can be expressed as a sum of two terms. These include a strain energy incurred to form a coherent interface (in this case applied only to Li metal), and the interfacial energy:[153]

$$G_{\mathrm{f}} = A\gamma + \zeta. \tag{3.18}$$

Here γ is the interface energy evaluated for the coherent LOC/Li junction, assuming strained Li metal. The interface energy is a measure of the interfacial bonding strength. ζ is the strain energy associated with matching the Li in-plane surface lattice constants to that of LOC. The calculated interface energies of Cl- and O-terminated interfaces are 0.50 and 0.42 J/m^2 at STP and 0.37 and 0.28 J/m^2 at the LOC synthesis conditions, respectively. As the interface energy is measured

relative to the average bonding in LOC and Li metal, the positive values predicted for γ imply that bonding at both interfaces is slightly weaker than on average in the bulk materials. Although the Cl-terminated *surface* is more stable than the O-terminated variant, the smaller magnitude of the *interface* energy obtained for the O-terminated interface suggests that the O-terminated interface is preferred relative to the Cl-terminated variant. It is possible that O-terminated interfaces may be formed from Cl-terminated LOC surfaces through segregation of oxygen to the interface. Regarding the strain energy, the computed value is small, only 0.03 eV. This follows from the small size of the strain and the softness of Li metal. Given that the interface energies of both terminations are comparable, we extend our characterization of their properties to both variants.

Interface adhesion and wettability. Using the relaxed interface geometries shown in Figure 3.4, Table 3.3 summarizes the interfacial work of adhesion, W_{ad}, and the contact angle, θ_c, for Li wetting of LOC. A large difference is observed in the W_{ad} values for the two interface terminations. First, adhesion at the Cl-terminated interface is relatively weak, W_{ad} = 0.09 J/m^2. This weak interaction is consistent with this interface's relatively undistorted atomic structure (Figure 3.4), and likely reflects the low reactivity (with Li metal) of the intact Li_6O octahedra

Table 3.3 Calculated work of adhesion and contact angle as a function of interface composition for the Li/LOC interface.

Interface	Work of adhesion (J/m^2)	Contact angle (°)
Cl-termination	0.09	143.4
O-termination	0.75	52.6

present at the interface. In contrast, adhesion at the O-terminated interface is much stronger, W_{ad} = 0.75 J/m^2. In this case the stronger adhesion arises from stronger interactions between the Li metal slab and the truncated Li_6O octahedra at the LOC surface, Figure 3.4. Re-forming the Li_6O octahedra and extending the LOC crystal structure by scavenging Li from the metal slab provides a driving force for stronger interfacial adhesion.

Prior studies have argued that the wettability of a SE by Li metal is desirable for achieving low interfacial resistance and for suppressing the formation of dendrites.[51–53] Wettability is typically evaluated using sessile drop experiments wherein the contact angle, θ_c, of molten Li on a SE substrate is measured.[53,154] $\theta_c > 90°$ is associated with weak, non-wetting interfacial

interactions, while $\theta_c < 90°$ implies strong interfacial adhesion.[154] The contact angle can be calculated from W_{ad} and the surface energy of Li, σ_{Li}, via the Young-Dupré equation:[155]

$$W_{ad} = \sigma_{Li}(1 + \cos\theta_c). \quad (3.19)$$

Table 3 shows the calculated contact angles for Li metal on the Cl- and O-terminated surfaces of LOC. Consistent with their relative W_{ad} values, Li is predicted to not wet the Cl-terminated surface, θ_c = 143.4°, but is expected to wet the O-terminated surface, θ_c= 52.6°. The possibility for achieving good Li wettability for the most stable (O-terminated) Li/LOC interface may underlie the good cyclability reported for this system in previous experiments.[67,68] Nevertheless, since the O-terminated surface of LOC has a higher surface energy (compared to the Cl-terminated version, Figure 3.4), it will be more reactive, for example, toward gas phase species potentially encountered during its synthesis and handling. New surface compounds formed by these reactions could reduce its wettability by Li, as shown recently for LLZO.[53] Thus, realizing the benefits of the O-terminated interface may require additional care in materials handling.

Interfacial electronic structure and electrochemical window. Stability against undesirable electron transfer to or from a SE depends upon the positions of the SE's band edges (CBM and VBM) in relation to the electrochemical potentials of the electrodes. Toward predicting this stability, the spatial distribution of the VBM and CBM of LOC in contact with a Li metal electrode were identified. Figure 3.5 shows charge density isosurfaces for the VBM and CBM of the O-terminated LOC/Li interface. These distributions were determined by analyzing the band- and k-point-decomposed partial charge density. Specifically, the VBM was identified as the highest occupied electronic state having the majority of its density located on the LOC slab; similarly, the CBM was identified by searching for the lowest energy unoccupied state with majority weight on the SE.

Figure 3.6 illustrates the predicted band edge positions and the corresponding electrochemical window for bulk LOC and for Li/LOC interfaces terminated with Cl or O. Band edge positions for bulk LOC were determined with the aid of a vacuum/slab supercell of LOC; this procedure predicts the behavior of bulk LOC far from surfaces/interfaces, and thus does not account for possible changes to the positions of the VBM or CBM due to interfacial interactions near electrodes (in this case a Li-metal anode). (Bulk band edge positions for a different SE, LLZO, were reported in a prior study.)[55] Importantly, the present study also quantifies the extent to which

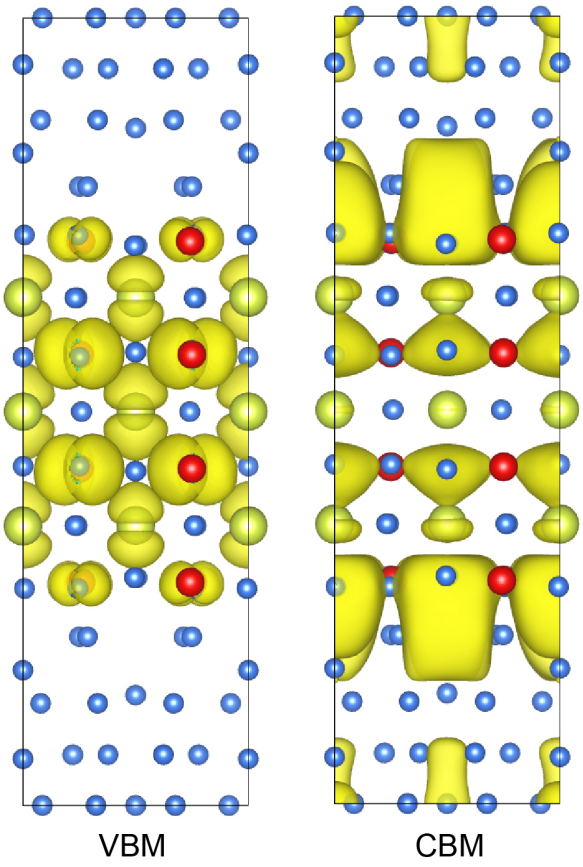

Figure 3.5 Charge density isosurfaces for the VBM (left) and CBM (right) of the O-terminated Li/LOC interface. Li atoms are blue, oxygen is red, and chlorine is yellow.

band edge positions change near interfaces (described below). This is done for the two explicit interface models shown in Figure 3.4.

Assuming a Cl-terminated (100) surface, Figure 3.6 shows that 'isolated' bulk LOC has band edge positions that are well outside of the operating window of a hypothetical Li metal/4.5 V battery. The CBM is located 0.4 eV above the vacuum level, and is separated by the bulk bandgap (8.04 eV) from the VBM, the latter 7.6 eV below the vacuum level. These band edge positions suggest that, in the limit of isolated/bulk LOC where all interfacial effects are ignored, there is negligible driving force for electron transfer to/from LOC from either an anode operating at the Li/Li^+ potential,[156] or to a cathode operating at 4.5 V.

Assuming the surface of LOC remains Cl-terminated, Figure 3.6 also shows that interfacing LOC with Li has little effect on the band edge positions. In this case only minor shifts in the VBM (+0.43 eV) and CBM (+0.04 eV) are predicted; these shifts reduce the band gap

slightly, to 7.65 eV. The relatively small shifts introduced by interfacial interactions at the Cl-terminated interface may be explained by the weak interactions present there. As mentioned above, the work of adhesion for this interface is small, only 0.09 J/m^2. Such weak interactions do not strongly perturb the electronic structure of LOC, leaving the band edge positions relatively unchanged from their positions in the bulk.

Turning to the O-terminated model of LOC, Figure 3.6 shows that the band edges for the bulk system do not differ significantly from those obtained for the Cl-terminated case: the band edges undergo only a small, 0.3 eV rigid shift to higher energies. Nevertheless, large differences are predicted for the explicit interface model. In contrast to the limited shifts observed for the Cl-terminated interface, the VBM and CBM of LOC at the O-terminated interface shift by +1.29 eV and -1.15 eV, respectively. These shifts narrow the LOC band gap by 2.4 eV, resulting in a smaller near-interface bandgap of 5.60 eV.

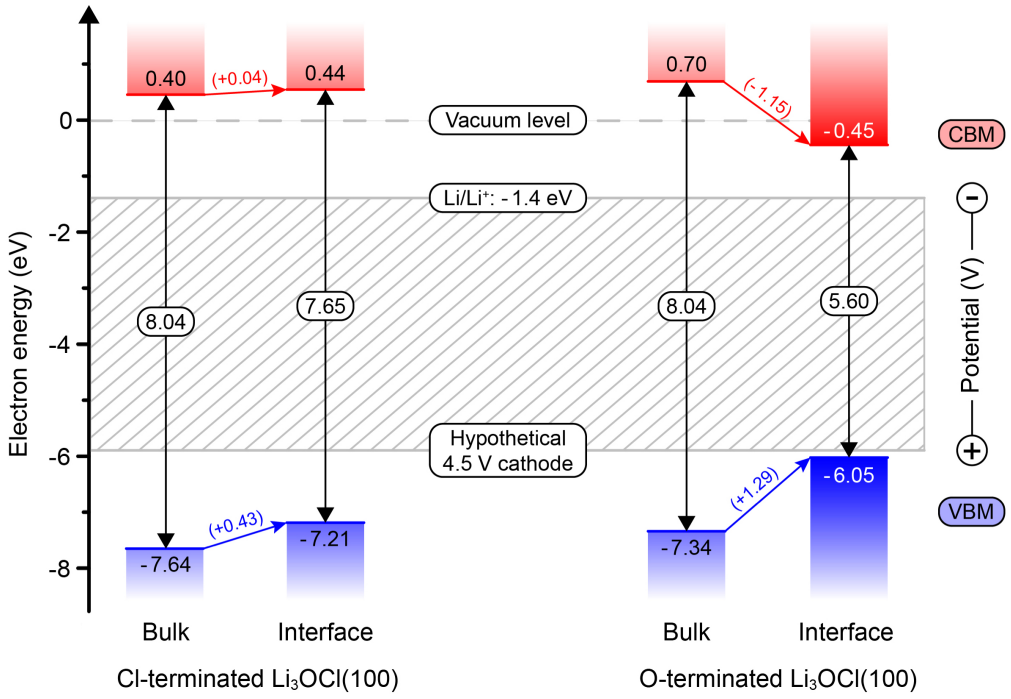

Figure 3.6 Electrochemical window bulk LOC and for Li/LOC interfaces. Both Cl- and O-terminated interfaces are investigated. Red and blue bands indicate the positions of the CBM and VBM, respectively. Numbers in parenthesis indicate the amount (in eV) by which the band edges shift (with respect to the bulk positions) at an interface with Li metal. The Li/Li$^+$ level and corresponding presumed 4.5 V cathode level are also shown (fading area). An energy of zero is assigned to the vacuum level, and the Li/Li$^+$ level is located 1.4 eV below the vacuum level.[156] The electrochemical potential for a hypothetical 4.5 V (relative to Li/Li$^+$) cathode is also plotted.

The relatively larger changes to the CBM & VBM that occur at the O-terminated interface are a consequence of the stronger bonding present there. Recalling the adhesion and contact angle data from Table 3.3, this interface is predicted to have a work of adhesion that is 8 times larger than the Cl-terminated case. Consequently, Li metal is expected to wet the O-terminated surface of LOC, but not the Cl-terminated one. It is likely that these stronger interfacial interactions induce significant perturbations to the LOC interfacial electronic structure (i.e., formation of new bonds), which in turn shift the band edges more substantially.

Despite the strong interactions present at the O-terminated interface, Figure 6 shows that the CBM for this system remains approximately 1 eV higher in energy (~ 1 V more negative) than the Li/Li^+ level. This positioning implies that electron transfer to LOC from a Li metal electrode is energetically unfavorable for the O-terminated interface (as well as for the Cl-terminated case, as discussed above) – a situation which is desirable from the standpoint of electrochemical stability. A previous study of the chemical stability of LOC using the grand potential phase diagram approach concluded that LOC will not decompose into other compounds when in contact with Li metal.[34] In total, the present and prior calculations suggest that LOC is both chemically and electrochemically stable against Li metal. This conclusion is in agreement with prior experiments showing that a Li/LOC/Li symmetric cell exhibited stable operation over many cycles, while SEM imaging of the Li/LOC interface found no evidence of new phase formation.[67]

Regarding oxidative stability, the resistance of LOC to electron withdrawing reactions depends upon the position of its VBM relative to the electrochemical potential of the cathode. An initial estimate of this stability can be gleaned from the position of the VBM for isolated/bulk LOC, as shown in Figure 3.6. In this approximation LOC appears to be stable for voltages exceeding 5.5 V. However, this stability limit is very likely overestimated; an explicit calculation of the LOC/cathode interface is needed – as done here for the Li/LOC interface – to position the VBM accurately. (In the limit of isolated/bulk LLZO, accounting for changes to the electrochemical potential of Li at the cathode was shown to shift the VBM to higher energies.[157]) Regarding chemical reactivity, a previous DFT calculation suggested that LOC will decompose into $LiClO_3$ and LiCl when in contact with an $LiCoO_2$ cathode.[34] In contrast, earlier full-cell experiments using the same cathode reported stable operating voltages up to 4.2 V.[67] Nevertheless, capacity fade observed in these experiments for the early stages of cycling could imply the formation of a solid electrolyte interphase (SEI) that prevents further reactions and preserves high

voltage operation. Under this scenario, which is commonly observed at the anode of conventional liquid electrolytes, there would be no inconsistency between the calculations and the experiments. Nevertheless, the possibility for SEI formation highlights the need to go beyond stability assessments that are based on thermodynamics alone: kinetic passivation should also be considered.

Examining the data from Tables 3.2 and 3.3 and Figure 3.6 more broadly, it appears that a tradeoff exists between the 'interfacial compatibility' of LOC with Li and its electrochemical window (as determined by the position of the LOC CBM). Specifically, Tables 3.2 and 3.3 show that the O-terminated interface is the most favorable system based on thermodynamics, adhesion, and Li wettability. On the other hand, Figure 3.6 shows that these favorable interfacial properties come at a cost to expected electrochemical performance; a more substantial shift of the CBM is observed for the O-terminated interface, resulting in reduced resistance to electron transfer with the negative electrode. Fortunately, for the present LOC-based system this tradeoff appears to be insufficient in magnitude to impact battery performance, as the bulk CBM starts several eV above the Li/Li^+ level, and interfacial effects do not push the CBM below that level. Nevertheless, it is reasonable to speculate that this trend should apply generally, as the formation of relatively stronger (interfacial) bonds generally coincides with larger perturbations to the electronic structure of a bonding couple.[158] Thus, other SEs whose bulk band edges lie closer to the electrochemical potentials of the electrodes may be more susceptible to electrochemical instability that is induced by strong interfacial bonding. Stated differently, solid electrolytes having excellent wettability by Li may not be optimal choices for minimizing undesirable electron transfer.

It is important to recognize that defects at the interface could influence interfacial properties. However, since neither the identities (interstitials, vacancies, anti-site defects, voids, etc.) nor the concentrations of these defects are known, it is not possible to speculate about even the qualitative nature of their impact – for example, do defects increase or decrease adhesion? As a first step in modeling any complex system (such as a realistic interface) it is helpful to have a clear understanding of an appropriate baseline. By examining the defect-free Li/LOC interface the present study provides such a baseline.

3.4 Conclusions

The present study has probed several properties of a model SE/Li metal interface at the atomic scale. In particular, the interfacial energy, work of adhesion, wettability, band edge shifts, and the electrochemical window were predicted computationally for a system based on the AP SE LOC. Vibrational contributions to the enthalpy and entropy were evaluated to estimate surface/interface energies at near-ambient temperatures. Interface wettability was characterized according to the Li contact angle on LOC, derived from the Young-Dupré equation and the calculated interfacial work of adhesion. Stability against reduction by the Li electrode was predicted by determining the positions of the band edges of LOC via GW calculations relative to the Li/Li^+ level.

These calculations suggest that the oxygen-terminated Li/LOC interface is the most thermodynamically stable. The calculated work of adhesion implies that Li will wet LOC with a low contact angle of ~53°, reflecting strong interfacial bonding and the possibility for low interfacial resistance. On the other hand, this strong interfacial interaction significantly narrows the bandgap of LOC in the interfacial region by shifting both the CBM and VBM: in the vicinity of the interface the size of the bulk bandgap, ~8 eV, is reduced to ~5.6 eV, implying a tradeoff between strong interfacial bonding/wettability and electrochemical stability. Despite this interface-induced reduction in electrochemical window, the CBM in LOC remains ~1 V more negative than the Li/Li^+ redox potential, denoting stability against reduction by the anode.

In total, the present study demonstrates how first-principles computational methods can be used to comprehensively characterize interfacial properties that are relevant to the operation of solid-state batteries.

Chapter 4 Correlating Lattice Distortions, Ion Migration Barriers, and Stability in Solid Electrolytes

4.1 Introduction

Building materials 'from the bottom up' is the most efficient and target-aiming way to explore new materials. This approach is in principle applicable for all research fields, including energy technologies, photonics, biosciences, pharmaceuticals, solid-state electronics, nanoscience, etc., where developing novel materials for desirable properties is important. The bottom-up method can be realized when we fully understand chemical, mechanical, and/or structural features that govern target properties to build materials atom by atom and molecule by molecule.

Fast ion-conducting solids have been studied for more than a half century, but still the prediction of ionic conductivity is not easy due to a lack of fundamental understanding of ionic mobility in solids. This is one of the key factors that limits our ability to build functional materials from the bottom up—from energy storage devices to sensors and conversion devices where the prediction of ion mobility in solids is necessary. The discovery of materials from the bottom up will accelerate the development of new functional materials, which requires the deep understanding of features that enable tuning ion mobility.

A fundamental question in the identification of new SEs is 'what chemical, mechanical, and/or structural features promote high ion mobility?'[38–41] Here we hypothesize that distortions of a solid's crystal structure are one such feature. These distortions include tilting/rotations of a crystal's polyhedral building blocks (octahedra, tetrahedra, etc.), variations in the length of the bonds that comprise these units, and a lowering of the crystalline (space group) symmetry, such as a distortion from cubic to orthorhombic symmetry.

The AP family of compounds presents an ideal venue to explore the impact of lattice distortions on ion mobility.[64] The degree of lattice distortion in the APs can be systematically tuned via atom substitution,[159,160] yet the relative simplicity of the structure allows for a comprehensive

characterization of ion mobility. Moreover, since the extent of lattice distortions present in a compound can correlate with its thermodynamic stability, the APs also present a vehicle for probing how changes to stability impact the rates of ion migration.

The degree of lattice distortion in the APs can be controlled through isoelectronic composition variation.[159] The degree of distortion in APs (X_3AB formula unit) is described by the Goldschmidt tolerance factor, t:[160] $t = (R_X + R_B)/\left[\sqrt{2}(R_X + R_A)\right]$, where R_X refers to the atomic radius of the cation (X), R_B refers to the radius of the framework halogen (B), and R_A is the same quantity for the chalcogenide ion (A) at the octahedron center. When $t \sim 1$ the ions fill space nearly perfectly, resulting in a highly symmetric structure with a cubic (or nearly-cubic) unit cell. To date, the APs that have been examined as SEs generally fall into this category.[64,65]

Lattice distortions in the AP structure emerge for compositions comprised of ions having with mis-matched sizes. For example, in LOC, chalcogens such as S and Se can be substituted for oxygen, while halogens such as F, Br, and I can replace Cl. These compounds exhibit a greater mismatch in atomic sizes, characterized by a decrease in the tolerance factor, $t < 1$, and an increase in lattice distortions. These distortions manifest as tilting of the cation octahedra, variations in the bond lengths of the octahedra, and deviations from cubic symmetry, Figure 4.1.[159,161,162] APs with tolerance factors close to unity crystallize with in the cubic Pm-3m space group. By analogy with the regular perovskites, in the APs as t decreases lower-symmetry space groups are expected to successively emerge (orthorhombic Pnma, hexagonal $P6_3cm$, and cubic Ia-3).[163,164] Moreover, t has also been correlated with thermodynamic stability, with smaller t values typically indicating a greater tendency for decomposition.[165–167]

Here, we systematically probe the connection between ionic mobility, thermodynamic stability, and symmetry-lowering lattice distortions across a series of 36 model APs. The degree of lattice distortion, quantified by the tolerance factor, t, is varied via isovalent composition variations involving the cation (X = Li, Na, or K) and anion sublattices (A = O, S, or Se, and B = F, Cl, Br, or I). DFT calculations were used to evaluate energetically preferred structures, energy barriers for all relevant ion migration pathways (assuming both vacancy and interstitial mechanisms), thermodynamic stability at zero Kelvin by the concept of convex hull (i.e., decomposition energies), stabilization temperature at which AP becomes stable with respect to chalcogenide and halide by predicting Gibbs free energy within QHA, and properties of AP

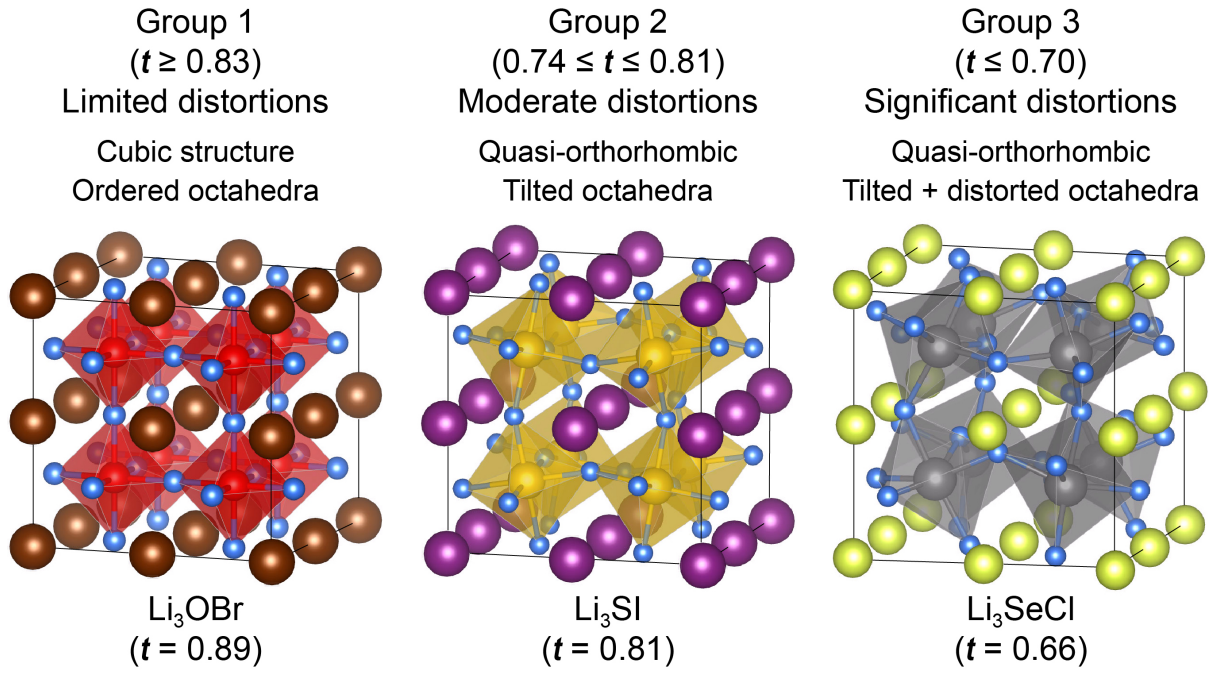

Figure 4.1 Classification scheme for Li- and Na-based AP SEs based on their degree of lattice distortion. Compounds in Group 1 have a high tolerance factor, exhibit highly ordered octahedra, and adopt the cubic Pm-3m structure. Groups 2 and 3 have quasi-orthorhombic structures, and are characterized by successively smaller tolerance factors and increasingly larger distortions to the Li/Na-octahedra. Three representative structures (Li_3OBr, Li_3SI, and Li_3SeCl) illustrate the increasing degree of distortion from Group 1 to Group 3.

compounds. We also characterized the difference in mobilities between Li, Na, and K in solids by comparing APs with the same anions [e.g., between LOC, NOC, and K_3OCl (KOC)]. This comparison is confined within the same structural/chemical/mechanical system with the same degree of lattice distortions (i.e., similar *t* factors).

Our calculations reveal that 'distortion tuning' can provide a pathway to higher ionic mobility. More specifically, a strong correlation is observed between the degree of lattice distortion and the minimum energy barrier for percolating ion migration: compounds with the largest lattice distortions exhibit the lowest migration barriers, independent of the migration mechanism. The energetic spread between the largest and smallest migration barriers for a given compound increases with the extent of distortion. Thus, lattice distortions slow migration along some pathways, while speeding up others. Fast pathways result from a combination of channel widening and destabilization of the potential energy surface. At the same time, larger distortions also correlate with diminished thermodynamic stability. Therefore, realizing high ionic mobility in this class of conductors requires balancing a tradeoff with stability.

Although thermodynamically unstable at zero Kelvin, most of APs indeed can be stabilized by thermal effects at elevated temperatures. We found a linear correlation that compounds with greater distortions have higher stabilization temperatures. The comparison between stabilization temperatures and long-range percolating barriers indicates that Li_3SeF, Na_3SeF, Na_3SBr, Na_3SF, K_3SeF and K_3SBr are 'Goldilocks' materials that satisfy relatively low stabilization temperatures as well as low limiting barriers. The predicted melting temperatures confirm that stabilization temperatures of these compounds (except K_3SBr) are upper limits of actual values. Also, we expect that AP compounds with stabilization temperatures about 1000 K could be realized. In addition, AP compounds are predicted to be stable against metal anodes, so AP SEs are advantageous to use the metal anode. The voltage limitations by the chemical stability window are in a range of 1.9 ~ 2.9 V for Li APs, 1.6 ~ 1.9 V for Na APs, and 1.2 ~ 1.4 V for K APs.

Contrary to expectations based on ionic radii, generally larger alkali ion has lower percolating barriers than smaller one in the AP lattice. The result reveals that 'packing fraction', 'frequency' of low-energy optical phonon, 'polarizability', and 'Bader charge' characterize the difference in ion mobilities between alkali ions. It implies that larger alkali ions transport through flexible and wider channels with larger vibration amplitudes and weaker electrostatic attractions to anions. We believe that our findings will elaborate design principles for superionic solid conductors.

4.2 Methodology

4.2.1 First-principles Calculations

Density functional theory. DFT calculations were performed with the Vienna *ab initio* Simulation Package (VASP).[134] The Perdew-Burke-Ernzerhof (PBE)[110] exchange-correlation functional was used in combination with the projector augmented wave (PAW) method.[135,136] The following valence electron configurations were adopted: $2s^1$ for Li, $3s^1$ for Na, $3s^23p^64s^1$ for K, $2s^22p^4$ for O, $2s^22p^5$ for F, $3s^23p^4$ for S, $3s^23p^5$ for Cl, $4s^24p^4$ for Se, $4s^24p^5$ for Br and $5s^25p^5$ for I. The plane-wave basis included functions with kinetic energies up to 450 eV for Li and Na compounds, and up to 500 eV for K compounds (K APs require higher cutoff energy to obtain accurate elastic properties). The energy cutoff was increased to 520 eV and $1s^22s^1$ for Li and $2p^63s^1$ for Na valence electrons were considered when chemical stability window calculations were

performed, the same to the Materials Project database. The Brillouin zone was sampled with a Γ-centered k-point mesh, and sampling was performed on grids ranging from 8 × 8 × 8 for the smallest computational cells (alkali-metal halides) to 2 × 2 × 2 for the largest systems (quasi-cubic systems with space group Ia-3, containing 80 atoms per cell). These sampling densities yielded energy convergence to within 1 – 2 meV/atom. The energy criterion for convergence of the self-consistency loop was set to 10^{-5} eV, and the force criterion for the relaxation of geometric degrees of freedom (ion positions and cell geometry) was 0.01 eV/Å.

Phonon calculations. Phonon properties require higher DFT accuracy than usual calculations. The plane-wave basis included functions with kinetic energies up to 600 eV for Li and Na compounds and 700 eV for K compounds. The Brillouin zone was sampled on an 8 × 8 × 8 grid for alkali halides (2 atoms), a 6 × 6 × 6 grid for alkali chalcogenides (3 atoms) and cubic APs (5 atoms), and a 4 × 4 × 3 grid for quasi-orthorhombic APs (20 atoms), with a Γ-centered k-point mesh. These k-point sampling densities yielded energy convergence to within 1 meV/atom. Our tests showed that K APs require finer k-point meshes to achieve accurate elastic constants: a 15 × 15 × 15 grid for cubic K APs and a 6 × 6 × 4 grid for quasi-orthorhombic APs were used when calculating elastic constants. The energy criterion for convergence of the self-consistency loop was set to 10^{-7} eV. The projection operators are evaluated in reciprocal space (LREAL tag in VASP) and an additional support grid for the evaluation of the augmentation charges was used (ADDGRID tag in VASP) to calculate very accurate forces enough to obtain smooth free energy data as a function of volume.

Hellman-Feynman forces were calculated using enlarged supercells based on a 3 × 3 × 3 replication with a single k-point (the Γ-point) for Li and Na cubic APs (135 atoms), Li and Na chalcogenides (324 atoms), and Li and Na halides (216 atoms), a 2 × 2 × 1 replication with a Γ-centered 1 × 1 × 2 k-point mesh for Li and Na quasi-orthorhombic APs (80 atoms), a 3 × 3 × 3 replication with a Γ-centered 2 × 2 × 2 k-point mesh for K cubic APs (135 atoms), a 2 × 2 × 1 replication with a Γ-centered 2 × 2 × 2 k-point mesh for K quasi-orthorhombic APs (80 atoms), and a 2 × 2 × 2 replication with a Γ-centered 4 × 4 × 4 k-point mesh for K chalcogenides (96 atoms) and K halides (64 atoms). These k-point sampling densities yielded energy convergence to within 1 – 2 meV/atom. Note that smaller replications were used for K chalcogenides and halides due to their larger unit cell sizes than those of Li and Na analogues, and K compounds requires denser k-point meshes to achieve accurate free energies. The atomic displacements of 0.03, 0.05,

and 0.20 Å were used for APs, chalcogenides, and halides, respectively. Born effective charges and static dielectric constants, required to include the non-analytic term in the dynamical matrix, were calculated by the Hessian matrix from the density functional perturbation theory, as implemented in VASP.

Migration energy barrier. The nudged elastic band (NEB) method[168,169] was used to evaluate energy barriers for cation migration via vacancy and interstitial 'dumbbell' mechanisms. NEB calculations were performed on enlarged supercells based on a 3 × 3 × 3 replication (135 atoms) of the unit cell for the cubic Pm-3m phase, and a 2 × 2 × 1 replication (80 atoms) for the quasi-orthorhombic phase, for Li and Na APs. Larger replications were used for K APs due to a relaxation issue: a 4 × 4 × 4 replication (320 atoms) of the unit cell for cubic Pm-3m compounds, and a 3 × 3 × 2 replication (360 atoms) for quasi-orthorhombic (Pnma) compounds (the valence electron configuration of K is reduced to $3p^6 4s^1$). K-point sampling was performed at the Γ-point for cubic supercells, and with a Γ-centered 1 × 1 × 2 k-point mesh for the quasi-orthorhombic systems (only the Γ-point was used for supercells of K APs due to their large sizes). Three intermediate NEB images were used, and the force convergence criterions for defect-structure relaxations and NEB calculations were set to lower than 0.02 and 0.04 eV/Å, respectively. It was assumed that the interstitial dumbbells do not rotate during migration, as the barrier for rotation has been reported to be more than twice that for translation.[66]

4.2.2 Thermodynamic Properties

Thermodynamic stability. The thermodynamic stability of the AP phases was assessed using the convex hull concept.[170] The energy relative to the convex hull, E_{H}, was calculated as:

$$E_{\mathrm{H}} = \left[E_{\mathrm{AP}} - \left(E_{\mathrm{Chalcogenide}} + E_{\mathrm{Halide}}\right)\right]/N, \tag{4.1}$$

where E_{AP} is the total energy per formula unit (f.u.) of the X_3AB AP phase, and $E_{\mathrm{Chalcogenide}}$ & E_{Halide} represent, respectively, the total energies (per f.u.) of the appropriate chalcogenide or halide end members. (For example, in the case of LOC, these end members would be Li_2O and LiCl.) $N = 5$ is the number of atoms per f.u. for the APs. A negative value for E_{H} indicates that a given AP is thermodynamically stable with respect to decomposition into a mixture of the end members; conversely, a positive E_{H} indicates a metastable (50 meV > E_{H} > 0),[171] or unstable phase (E_{H} > 50 meV).

Stability at finite temperature. The stabilization temperature is a point at which the free energy of an unstable compound at zero Kelvin (e.g., AP compounds) becomes lower than the sum of free energies of competing phases (e.g., corresponding chalcogenide and halide, into which unstable APs are prone to decompose)[56,66], i.e.,

$$\Delta G \leq G_{\mathrm{AP}} - \left(G_{\mathrm{Chalcogenide}} + G_{\mathrm{Halide}}\right). \tag{4.2}$$

The competing phases are chosen from the fact that unstable APs are prone to decompose into corresponding chalcogenide and halide. Because the calculation is based on solid phases, ΔG is evaluated up to the predicted melting temperature of APs. Then, the stabilization temperature was found by extrapolating last three data points of ΔG graph as a function of temperature until ΔG becomes zero.

Chemical stability window. The chemical stability window of APs (i.e., stable voltage range with respect to a metal anode) was investigated by following the method for the grand potential phase diagram with the Materials Project database (*pymatgen* code).[37,133,172,173] The decomposition energy of a given phase into the phase equilibria in a contact with Li, Na, or K metal reservoir at an applied voltage ϕ (at zero Kelvin without vibrational contributions and the pV term)[133] can be expressed as[36]

$$E_{\mathrm{D,open}}(\phi) = E_{\mathrm{Phase\ equilibria}}(\phi) - [E_{\mathrm{AP}} + \Delta n_{\mathrm{M}} \cdot \mu_{\mathrm{M}}(\phi)], \tag{4.3}$$

where $E_{\mathrm{Phase\ equilibria}}(\phi)$ is the sum of total energies of phases at the equilibrium, E_{AP} the total energy of AP, Δn_{M} is the change in the number of atom M = Li, Na, or K metal (denoting reduction/oxidation when Δn_{M} is positive/negative), and μ_{M} is the chemical potential of M described as[36]

$$\mu_{\mathrm{M}}(\phi) = \mu_{\mathrm{M}}^{0} - ze\phi, \tag{4.4}$$

where μ_{M}^{0} is the chemical potential of M without external potential, z is the charge number of M (+1 for alkali metals), and e is the electron charge. The window is the range where APs are not reduced nor oxidized.[36]

Melting temperature. The Lindemann's law treats melting as a vibrational instability, expressed as $T_m = c\langle M\rangle T_{\mathrm{D}}^2 d^2$, where c is a constant, $\langle M\rangle$ is the average atomic mass, T_{D} is the

Debye temperature, and d is a characteristic length ($d^3 = V_a$ is the average volume per atom).[174,175] The Debye temperature is calculated by elastic properties as[176,177]

$$T_{\mathrm{D}} = \frac{2\pi\hbar}{k_B}\left[\frac{3n}{4\pi}\left(\frac{N_{\mathrm{A}}\rho}{M}\right)\right]^{1/3} v_m, \tag{4.5}$$

$$v_m = \left[\frac{1}{3}\left(\frac{2}{v_t^3} + \frac{1}{v_l^3}\right)\right]^{-1/3}, \tag{4.6}$$

$$v_l = [(B + 4S/3)/\rho]^{1/2}, \tag{4.7}$$

$$v_t = (S/\rho)^{1/2}, \tag{4.8}$$

where n is the number of atoms in a unit cell, N_{A} is the Avogadro's number, ρ is the density, M is the molecular weight, v_m is the average sound velocity, v_l and v_t are the longitudinal and transverse mode velocities, and B and S are the bulk and shear moduli. The Voigt[178] and Reuss[179] formulas estimate theoretical maximum and the minimum values of the moduli, respectively, using the stiffness tensor C_{ij}.[180] We used the Voigt equations

$$B = [(C_{11} + C_{22} + C_{33}) + 2(C_{12} + C_{13} + C_{23})]/9, \tag{4.9}$$

$$S = [(C_{11} + C_{22} + C_{33}) - (C_{12} + C_{13} + C_{23}) + 3(C_{44} + C_{55} + C_{66})]/15, \tag{4.10}$$

from the fact that predicted Voigt bulk moduli are almost the same to the values obtained by the Murnaghan EOS fitting (see Table 4.1). DFT calculations were used to obtain elastic properties.

Table 4.1 Predicted bulk and shear moduli of anti-perovskite compounds using the Voigt equations. Values in parentheses are the bulk moduli using the Murnaghan EOS.

Li APs	Moduli (GPa)		Na APs	Moduli (GPa)		K APs	Moduli (GPa)	
	Bulk	Shear		Bulk	Shear		Bulk	Shear
Li_3OF	58.3 (59.7)	42.2	**Na_3OF**	37.2 (36.8)	24.4	**K_3OF**	25.9 (24.0)	9.8
Li_3OCl	52.6 (52.9)	39.7	**Na_3OCl**	30.2 (32.4)	21.9	**K_3OCl**	19.5 (20.6)	10.5
Li_3OBr	49.3 (48.6)	37.3	**Na_3OBr**	29.1 (31.2)	21.2	**K_3OBr**	20.5 (19.7)	12.9
Li_3OI	44.0 (43.4)	33.0	**Na_3OI**	27.3 (28.9)	19.8	**K_3OI**	17.5 (18.7)	11.9
Li_3SF	42.2 (43.2)	32.4	**Na_3SF**	30.6 (31.8)	20.1	**K_3SF**	20.1 (20.7)	11.8
Li_3SCl	29.4 (29.7)	18.6	**Na_3SCl**	21.5 (21.6)	11.5	**K_3SCl**	13.5 (14.0)	6.4
Li_3SBr	29.0 (28.8)	17.9	**Na_3SBr**	20.8 (21.0)	11.1	**K_3SBr**	13.6 (13.6)	5.8
Li_3SI	27.4 (27.7)	17.1	**Na_3SI**	19.8 (20.0)	10.5	**K_3SI**	13.2 (12.9)	6.0
Li_3SeF	46.4 (47.5)	36.1	**Na_3SeF**	34.4 (34.2)	24.8	**K_3SeF**	17.5 (19.1)	11.0
Li_3SeCl	25.2 (25.4)	15.6	**Na_3SeCl**	18.5 (18.3)	9.3	**K_3SeCl**	12.2 (12.1)	5.3
Li_3SeBr	24.4 (24.7)	14.6	**Na_3SeBr**	18.0 (18.3)	9.1	**K_3SeBr**	12.4 (12.0)	5.2
Li_3SeI	23.6 (24.0)	14.3	**Na_3SeI**	17.4 (17.6)	8.8	**K_3SeI**	11.6 (11.4)	5.3

The finite differences were used for stiffness tensor calculations to include cell distortions as well as ionic contributions, as implemented in VASP. The constant *c* in the Lindemann's relation was empirically estimated using reported melting temperatures of previously synthesized APs: the *c* value for Li APs was obtained by averaging empirical *c* values of LOC and LOB,[5] and the same method was used for Na APs using empirical *c* values of NOC, NOB, and NOI.[6] Note that the maximum difference between the empirical *c* values of these 5 APs is only 8.5%.

4.3 Results and Discussion

4.3.1 Structure

LOC, LOB, and their Na and K analogues have been synthesized previously.[64,65,181–183] These compounds adopt a cubic structure with space group Pm-3m (KOC undergoes the phase transformation between low-T orthorhombic and high-T cubic at 364 K). Isoelectronic composition variation on the cation (X = Li, Na, or K) and anion sublattices (A = O, S, or Se, and B = F, Cl, Br, or I) results in 28 additional (hypothetical) AP compositions. The ion substitution results in a change to the tolerance factor, and potentially convert the cubic Pm-3m structure (generally present for $0.9 < t < 1.0$) into one of three other structure types: orthorhombic (Pnma, for tolerance factors roughly between 0.75 and 0.9), hexagonal ($P6_3cm$, $t \lesssim 0.75$), and cubic (Ia-3, for tolerance factors beyond the hexagonal regime).[163,164] Initial structures adopting the 4 structure types were generated for each of the 24 possible compositions. These structures were based on the following prototypes: Li_3OCl[64] (Pm-3m), $CaTiO_3$[184] (Pnma), $HoMnO_3$[185] ($P6_3cm$), and $ScFeO_3$[186] (Ia-3). All structures were fully relaxed, with the resulting energy-volume data fit to the Murnaghan EOS.[132]

In addition to deviations from cubic symmetry, additional distortions in the perovskite can occur via perturbations to the octahedral building blocks. These include: octahedron tilting, displacement of the octahedron's central ion, and distortion of the octahedron shape, resulting in deviations to the octahedron's bond lengths and angles.[159,161,162] These distortions can occur independently or simultaneously.[161] For example, a previous DFT study predicted that LOC ($t = 0.84$)[187] should undergo a minor orthorhombic distortion at $T = 0$ K.[86] However, the tilting angle (< 2°) and the energy difference (0.2 meV/atom) relative to the cubic (Pm-3m) system were

extremely small. Thus, the predicted structure is approximately cubic, as observed experimentally at ambient conditions.[64]

Table 4.2 lists the tolerance factors of all 36 compounds examined. The tolerance factors were evaluated using the reported ionic radii.[187] The tolerance factor approaches unity upon substitution of larger halogen ions and smaller chalcogen ions. Conversely, *t* is generally smallest for substitutions of large chalcogens and small halogens, e.g., Li_3SeCl ($t = 0.66$). In the case of the initially orthorhombic and cubic (Ia-3) cells, upon relaxation the lattice vectors of these systems exhibit slight distortions from their original orthogonal orientations (deviations are less than 0.1° and 5.3°, respectively); thus, we refer to these structures as 'quasi-orthorhombic' and 'quasi-cubic.' No distortions to the lattice vector angles were observed in the hexagonal structures. Surprisingly, during relaxation of the F-containing compounds Li_3SF, Li_3SeF, Na_3SF, Na_3SeF, K_3SF and K_3SeF, the chalcogen and halogen ions interchanged positions via rearrangement of the Li-ion sublattice. This rearrangement positions F at the center of the Li octahedra, and increases the tolerance factor significantly.

Table 4.2 Calculated limiting barriers (meV) along preferred pathways for vacancy/dumbbell migrations. The tolerance factor (*t*) and Group are also given for each compound.

Li-based Compounds	*t* (Group)	Barrier	Na-based Compounds	*t* (Group)	Barrier	K-based Compounds	*t* (Group)	Barrier
Li_3OF	0.68 (3)	129/24	**Na_3OF**	0.69 (3)	201/50	**K_3OF**	0.69 (3)	134/32
Li_3OCl	0.84 (1)	325/138	**Na_3OCl**	0.83 (1)	240/101	**K_3OCl**	0.81 (2)	214/81
Li_3OBr	0.89 (1)	370/167	**Na_3OBr**	0.87 (1)	355/125	**K_3OBr**	0.85(1)	203/87
Li_3OI	0.97 (1)	297/225	**Na_3OI**	0.94 (1)	426/165	**K_3OI**	0.91 (1)	355/122
Li_3SF	0.88 (2)	109/60	**Na_3SF**	0.86 (2)	166/79	**K_3SF**	0.84 (2)	198/45
Li_3SCl	0.70 (3)	115/34	**Na_3SCl**	0.70 (3)	112/36	**K_3SCl**	0.70 (3)	59/35
Li_3SBr	0.74 (2)	191/64	**Na_3SBr**	0.74 (2)	184/52	**K_3SBr**	0.73 (2)	144/81
Li_3SI	0.81 (2)	270/114	**Na_3SI**	0.80 (2)	270/99	**K_3SI**	0.79 (2)	220/70
Li_3SeF	0.93 (1)	138/68	**Na_3SeF**	0.90 (1)	202/76	**K_3SeF**	0.88 (2)	203/70
Li_3SeCl	0.66 (3)	100/48	**Na_3SeCl**	0.67 (3)	95/68	**K_3SeCl**	0.67 (3)	76/69
Li_3SeBr	0.70 (3)	122/42	**Na_3SeBr**	0.70 (3)	111/30	**K_3SeBr**	0.70 (3)	71/36
Li_3SeI	0.76 (2)	201/70	**Na_3SeI**	0.76 (2)	205/72	**K_3SeI**	0.75 (2)	186/60

The calculations predict that the quasi-orthorhombic structures are generally the lowest in energy. For a few compositions the energy of the quasi-orthorhombic structure is nearly identical to (< 5 meV/atom difference) that of the cubic (Pm-3m) or quasi-cubic (Ia-3) variants. These cases include LOC, LOB, NOC, NOB, NOI, K_3OBr (KOB), and K_3OI (KOI) which, based on

experiments, crystallize in the Pm-3m structure.[64,65,181,182] Given the computational and experimental preference for the Pm-3m and quasi-orthorhombic structures, these two systems were adopted for subsequent calculations of migration barriers. The structural parameters for all low-energy structures are listed in Table 4.3.

The AP examined here were further classified into three groups based on their tolerance factor and the degree of octahedral distortions. Figure 4.1 illustrates this classification. 'Group 1' includes cubic Pm-3m compounds having well-ordered octahedra and tolerance factors $t \geq 0.83$. This behavior is similar to that of the cubic perovskite oxides, whose tolerance factors typically fall between 0.9 and 1.0.[161] As the tolerance factor decreases, mismatch in atomic radii leads to moderate distortions via tilting of the octahedra, and a change in symmetry to quasi-orthorhombic, 'Group 2'. Here, $0.73 \leq t \leq 0.81$, and the degree of octahedron tilting (11.5 – 21.7°) increases with decreasing t. Finally, in 'Group 3', $t \leq 0.70$, and the system remains quasi-orthorhombic. These systems have significant distortions to the octahedra, including tilting (21.0 – 29.0°) and X–A–X bond angle distortions (7.3 – 12.9°).

4.3.2 Ion Transport

Migration pathway. Under equilibrium conditions, the formation energies of charge carriers (vacancies or interstitials) can impact mobility and conductivity. Earlier studies have shown that these formation energies can be high.[66,69,71,72] However, experiments have shown that the concentrations of these species in the AP ion conductors can be controlled during synthesis by employing non-stoichiometric ratios of the precursors. For example, 6.66% Li vacancies were achieved in $Li_{2.8}OCl_{0.8}$ by depleting the amount of LiCl during synthesis.[64] The 'baked in' nature of these concentrations suggests that migration energies, and not the activation energies, are of paramount importance in understanding ionic mobility in the APs. This observation motivates our emphasis on migration barriers. (In addition, we found that the formation energy of neutral cation vacancies is not strongly correlated with the tolerance, and that the presence of a defect increases the magnitude of local distortions.)

The simplicity of the AP structure allows for a comprehensive sampling of the activation energies and minimum energy pathways associated with ion migration. NEB calculations were used to evaluate these pathways for both the vacancy and interstitial dumbbell mechanisms. The

Table 4.3 Structural parameters for the anti-perovskites X_3AB (X = Li, Na or K, A = O, S or Se and B = F, Cl, Br or I). Values in parentheses represent previous experiment data.[64,65,181–183]

Compound	Symmetry	a (Å)	b (Å)	c (Å)	α (°)	β (°)	γ (°)
Li_3OF	Quasi-orthorhombic	5.038	5.112	7.178	89.999	89.999	89.999
Li_3OCl	Cubic	3.900 (3.91)					
Li_3OBr	Cubic	3.989 (4.02)					
Li_3OI	Cubic	4.161					
Li_3SF	Quasi-orthorhombic	5.571	5.527	7.849	89.998	90.000	89.992
Li_3SCl	Quasi-orthorhombic	6.276	6.321	8.932	89.994	90.008	89.991
Li_3SBr	Quasi-orthorhombic	6.440	6.499	9.191	89.998	90.004	90.010
Li_3SI	Quasi-orthorhombic	6.689	6.684	9.458	90.000	90.000	90.000
Li_3SeF	Cubic	4.011					
Li_3SeCl	Quasi-orthorhombic	6.453	6.485	9.160	90.000	89.998	90.004
Li_3SeBr	Quasi-orthorhombic	6.651	6.677	9.464	89.999	90.014	90.000
Li_3SeI	Quasi-orthorhombic	6.908	6.906	9.781	89.998	90.000	90.001
Na_3OF	Quasi-orthorhombic	5.844	6.044	8.286	89.999	89.999	89.999
Na_3OCl	Cubic	4.549 (4.491)					
Na_3OBr	Cubic	4.618 (4.564)					
Na_3OI	Cubic	4.746 (4.707)					
Na_3SF	Quasi-orthorhombic	6.312	6.269	8.918	89.998	90.002	90.001
Na_3SCl	Quasi-orthorhombic	7.045	7.157	10.013	90.002	89.999	89.995
Na_3SBr	Quasi-orthorhombic	7.190	7.345	10.264	90.024	90.067	89.993
Na_3SI	Quasi-orthorhombic	7.442	7.492	10.548	90.000	90.000	90.000
Na_3SeF	Cubic	4.509					
Na_3SeCl	Quasi-orthorhombic	7.180	7.342	10.179	90.008	89.998	89.998
Na_3SeBr	Quasi-orthorhombic	7.414	7.510	10.525	90.007	90.004	90.009
Na_3SeI	Quasi-orthorhombic	7.625	7.744	10.852	90.000	90.000	90.000
K_3OF	Quasi-orthorhombic	6.801	6.985	9.683	90.000	90.000	90.000
K_3OCl	Quasi-orthorhombic	7.411 (7.239)	7.282 (7.239)	10.346 (10.277)	89.998 (90.000)	89.999 (90.000)	90.088 (90.000)
K_3OBr	Cubic	5.270 (5.213)					
K_3OI	Cubic	5.374 (5.283)					
K_3SF	Quasi-orthorhombic	7.094	7.544	10.202	90.000	90.000	90.000
K_3SCl	Quasi-orthorhombic	7.984	8.153	11.317	90.003	90.000	89.996
K_3SBr	Quasi-orthorhombic	8.070	8.408	11.557	90.013	90.057	89.996
K_3SI	Quasi-orthorhombic	8.321	8.574	11.872	89.971	90.000	89.987
K_3SeF	Quasi-orthorhombic	7.369	7.365	10.418	90.000	90.000	90.000
K_3SeCl	Quasi-orthorhombic	8.077	8.375	11.397	90.003	90.003	90.013
K_3SeBr	Quasi-orthorhombic	8.339	8.520	11.822	89.995	89.997	90.010
K_3SeI	Quasi-orthorhombic	8.546	8.794	12.115	89.971	89.947	90.011

elementary migration events that comprise these two mechanisms involve ion hopping along the 12 edges of the Li/Na octahedra. Due to the high symmetry of the cubic AP, the 12 pathways in

this system are degenerate; it is therefore sufficient to evaluate a single path for each of the two mechanisms. In contrast, in the lower-symmetry quasi-orthorhombic systems the presence of lattice distortions implies that all 12 elementary migration paths are distinct. These quasi-orthorhombic compounds contain four distinct octahedra per unit cell. Nevertheless, these octahedra exhibit very similar structures – the maximum structural deviations between octahedra are in all cases less than 2.4%: X–A bond lengths (< 0.2% deviation), X–A–X bond angles (< 1.3%), distances between alkali-metal ions ($d_{X\text{-}X}$ < 1.0%), and distances between alkali-metal ions and framework anions ($d_{X\text{-}B}$ < 2.4%). Due to the near-equivalence of the octahedra, it is sufficient to map out migration mechanisms along the 12 pathways that orbit a single octahedron. This assertion was tested by calculating all 48 barriers for the vacancy mechanism in Li_3SI, the AP having the largest structural deviations between octahedra. As expected, the differences between elementary barriers on distinct octahedra were found to be small, less than 1.4%.

Figure 4.2 shows the connectivity between octahedra in a representative Group 3 distorted AP structure, Li_3SeCl (t = 0.66). Mobile cations are located at the octahedron vertices, which are shared by adjacent octahedra. The cations in each octahedron are labeled 1 through 6; equivalent labels are shown at the shared vertices for selected ions. Using this labeling scheme, a percolating

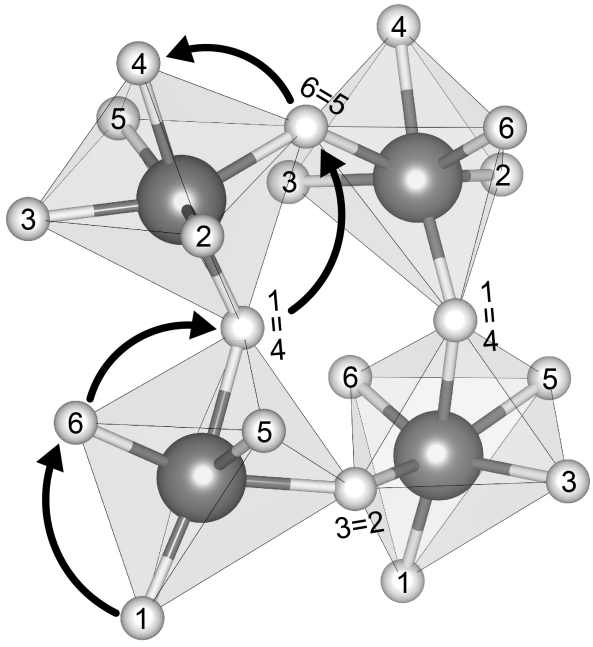

Figure 4.2 Connectivity between octahedra in distorted APs. Atomic sites of mobile ions are numbered; identical sites in different octahedra adopt the same number. (Selected shared vertex sites are indicated with an equals sign.) Arrows illustrate an example of a migration pathway resulting in long-range ion transport.

pathway (i.e., one which allows for macroscopic ion migration) can be identified by the numerical sequence of sites visited during the migration process. For example, the arrows in Figure 4.2 depict a pathway that starts at the bottom of the bottom-left octahedron and terminates at the top edge of the top-left octahedron: 1 → 6 → 4 (= 1) → 6 → 4 (= 1).

We aim to find low-energy migration pathways that contribute to long-range (percolating) ion transport. These pathways were identified by combining multiple elementary migration events. Here, an elementary migration event corresponds to the hop of a vacancy or an interstitial dumbbell to an adjacent octahedral site along an octahedron edge. The following procedure was employed to find percolating pathways: (1) One of the six cation sites on an octahedron is selected as the initial position for a vacancy or interstitial. (2) The defect migrates to an adjacent site along the path having the lowest barrier. (3) At the new site, the barriers for the non-reversing paths are compared to those for the discarded paths from the previous step(s). If all barriers out of the current site are larger than the smallest of the previously-discarded barriers, then the search reverts to the previous site and migrates along the discarded pathway with the smallest barrier. Alternatively, the defect continues along the path having the lowest barrier. (4) Step 3 is repeated until a pathway is identified that does not contain closed loops or revisit sites. The pathway should terminate at a site that is crystallographically-equivalent to the initial site. (5) Return to step 1; repeat the process for all possible initial locations of the mobile species. Stitching together multiple elementary migration events will yield a percolating pathway with multiple maxima. The procedure described above identifies the percolating pathway having the *smallest maximum* migration barrier. We refer to this pathway as the *preferred pathway* and its associated barrier as the *limiting barrier*.

Percolating barrier. Table 4.2 lists the limiting barriers of preferred pathways for all 36 AP candidates. The limiting barriers fall within 59 – 426 meV for the vacancy mechanism, and within 24 – 165 meV for the interstitial dumbbell. The relatively lower barriers observed for the interstitial mechanism are consistent with prior reports on selected AP SE.[66] Importantly, the range of limiting barriers for all-but-one of the compounds fall below the ~400 meV threshold estimated assuming a SE with 10 μm thickness and C/2 rate.[45] Other reports have suggested activation energies in the range of 200 – 300 meV as being desirable for a viable SE;[188] all but five of the APs considered here – all operating via vacancy migration – satisfy this criterion. Moreover, a significant fraction of the APs exhibit migration barriers that are smaller than or comparable to those reported in the literature for state-of-the-art solid electrolytes: $Li_{10}GeP_2S_{12}$ (250 meV),

$Li_7La_3Zr_2O_{12}$ (310 meV), Li_6PS_5Cl (110 meV) and Li_2S-P_2S_5 glass (390 meV).[19,21,189,190] (These literature values may, in some cases, refer to *activation energies*, which can include contributions from formation energies and from defects such as grain boundaries. Consequently, direct comparisons with the *migration energies* reported in the present study should be undertaken with care.) In total, high ionic conductivity could be possible in these APs if they could be synthesized in a form having high carrier concentrations. Nevertheless, it should be emphasized that a complete assessment of the viability of a SE should include factors beyond intrinsic (bulk) migration energies. For example, recent studies have highlighted contributions from grain boundaries[82,191] and electrolyte/electrode interfaces[53] in the performance of solid electrolytes.

Can the size of an AP's limiting barrier be related to a fundamental property? Figure 4.3 probes the connection between barrier size and the magnitude of the lattice distortion by plotting the limiting barrier as a function of the tolerance factor; the barriers and *t* values for all compounds are summarized in Table 4.2. These data show that the barrier size exhibits a strong linear correlation with the tolerance factor, independent of the migration mechanism (vacancy or dumbbell): larger tolerance factors, indicative of limited distortions, yield higher migration barriers, while smaller values of *t* (greater distortion) yield lower barriers. Thus, ionic mobility can be maximized by 'distortion tuning': substitution of larger chalcogen and smaller halogen ions within the AP structure results in lower limiting barriers. Interestingly, the F-centered compounds do not follow this trend; they have lower barriers than other compounds with similar *t*.

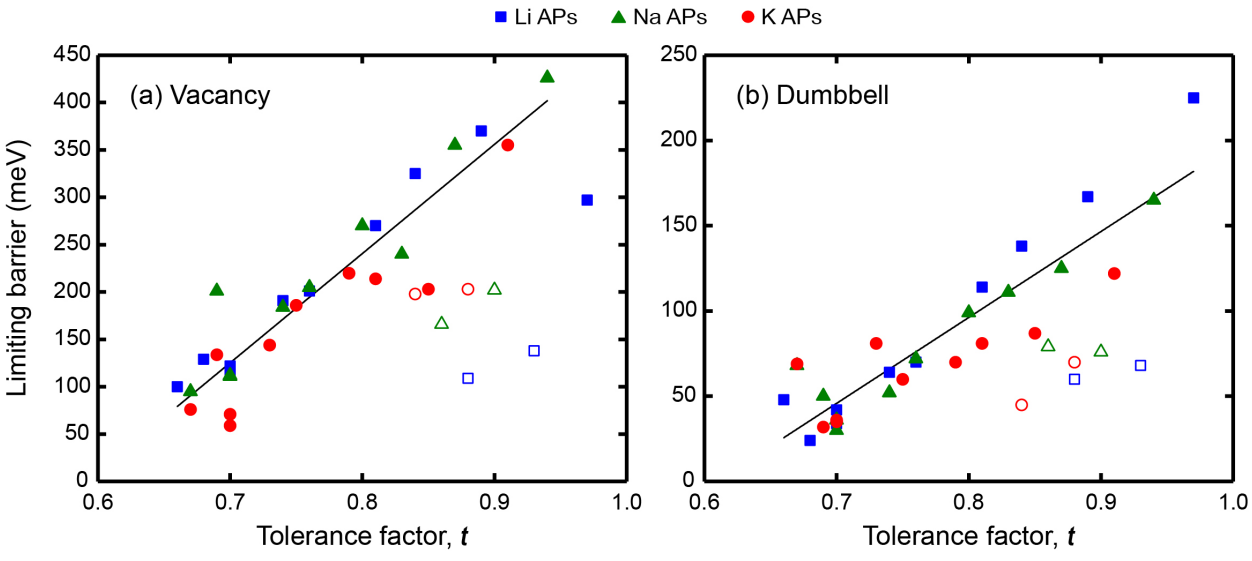

Figure 4.3 Correlation between the tolerance factor and limiting barriers of (a) vacancy and (b) dumbbell mechanisms. The linear fitting is implemented excluding the 'F-centered' compounds (unfilled shapes).

An earlier study found that substitution of larger, more polarizable chalcogen anions in $Li_{10\pm1}GeP_2X_{12}$ (via the substitutions X = O → S → Se) lowered activation energies by increasing the width of the cation migration channel.[46] This trend is also present in our data, and will be described in more detail below. In yet another example, increasing the polarizability (and size) of the halogen anions in the argyrodites Li_6PS_5X via the substitutions X = Cl → Br → I resulted in decreasing lattice stiffness, which in turn yielded lower activation energies.[44] This trend is absent in the AP systems studied here: activation energies increase with increasing polarizability of the framework halogen anion. This discrepancy could result from a larger impact from distortion-related effects, which could overshadow effects arising from differences in the size and polarizability of the halogens.

Figure 4.4 plots the distribution of the energy barriers for all elementary migration paths as a function of the degree of lattice distortion, as measured by the tolerance factor. The barriers are obtained by averaging forward and backward hops. As described above, in the cubic Pm-3m systems all elementary paths are equivalent, and are therefore described by a single barrier. This degeneracy is broken in the non-cubic compounds, resulting in a widening distribution of energy barriers with increasing distortions, or equivalently, decreasing *t*. Taking vacancy migration as an

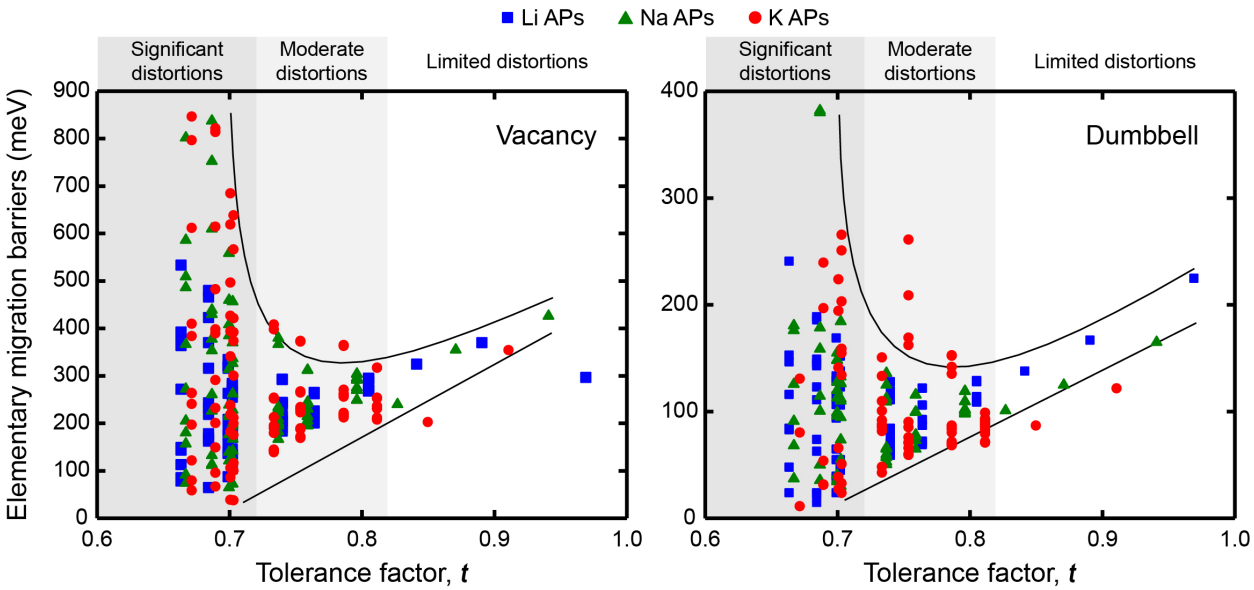

Figure 4.4 Dispersion of elementary migration barriers as a function of the tolerance factor. The lattice distortion breaks the degeneracy between elementary barriers, resulting in a wider distribution with greater distortions. The smallest barriers become lower linearly while the largest barriers increase exponentially with smaller tolerance factor. The preferred pathway can be established by connecting low elementary barriers. 'F-centered' compounds are not included.

example, compounds with moderate tolerance factors, $t \sim 0.8$, exhibit a relatively narrow range (<100 meV) of barrier energies. This range increases rapidly with decreasing t, reaching a spread of ~900 meV for compounds having the smallest tolerance factors. Our results generalize the findings of an earlier study on $Li_3OCl_{0.5}Br_{0.5}$, which found that Cl–Br substitutional disorder results in a spectrum of activation barriers.[66] In addition, the largest and smallest barriers vary distinctly with respect to t: the smallest barriers shrink in roughly linear proportion to t, while the largest barriers grow super-linearly. Thus, an increase in lattice distortion facilitates migration along some elementary pathways, while slowing others. If these lower-barrier hops can be connected in a percolating network, then ionic mobility can increase.

4.3.3 Thermodynamic Stability

Stability at zero Kelvin. While our emphasis thus far has been on clarifying the connection between lattice distortions and ionic mobility, the linkage between mobility and thermodynamic stability is also of fundamental interest. Moreover, the observation that several of the compounds examined exhibit low limiting barriers raises the question: can these materials be made? To answer, the thermodynamic stability of the APs was assessed using the convex hull concept.[170] More specifically, the decomposition energy, E_d, of each AP at zero Kelvin was calculated assuming decomposition into a two-component mixture of alkali chalcogenides and halides. Per literature convention,[171] the APs were grouped into three categories based on their decomposition energies: (i.) Stable, $E_d < 0$, (ii.) Metastable, E_d within 0 – 50 meV/atom, and (iii.) unstable, $E_d >$ 50 meV/atom.

Figure 4.5 plots the decomposition energy for each AP as a function of its tolerance factor (E_d are listed in Table 4.4). As expected, the data show a rough correlation between stability and t: compounds having larger lattice distortions (smaller t) tend to be less stable.[165–167] We recall from the preceding discussion that larger limiting barriers correlate with larger t; thus, a tradeoff exists between ionic mobility and stability: increasing the degree of lattice distortion enhances mobility, but comes at a cost to stability. While it is unlikely a compound such as Li_3SeCl with a very low limiting barrier (48 meV) would be stable (E_d = 73 meV/atom), compounds that balance stability with the barrier height could be promising. Na_3SI represents one such 'Goldilocks' material: it possesses both a moderate decomposition energy of 27 meV/atom and small limiting barrier heights of 99 and 270 meV for the interstitial and vacancy mechanisms, respectively, Table

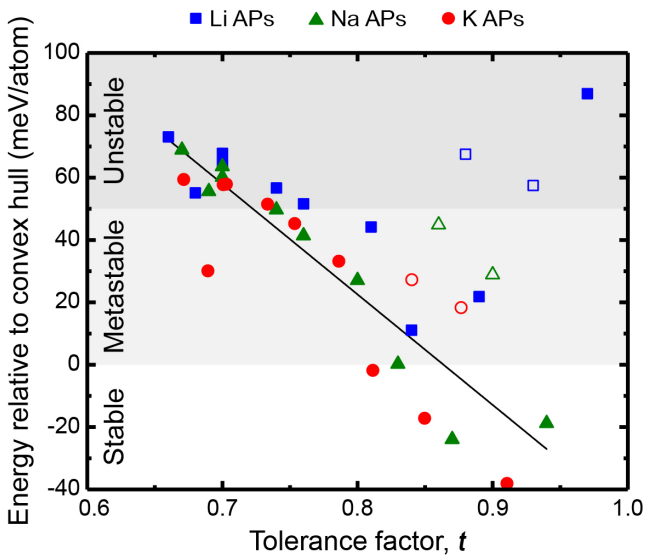

Figure 4.5 Correlation between the tolerance factor and the energy relative to convex hull (equivalent to the decomposition energy) of APs. The linear fitting is implemented excluding 'F-centered' compounds (unfilled shapes).

4.2. Notably, E_d for Na_3SI is similar to that of Li_3OBr (22 meV/atom), a compound which has been experimentally synthesized, yet whose barriers are up to 100 meV larger. Consequently, Na_3SI is proposed as a target for experimental study. We note that the structure of Na_3SI is similar to that of the anti-perovskite mixed conductor β-Ag_3SI.[192]

Table 4.4 Calculated decomposition energies, E_d, of the APs at zero Kelvin. Positive values imply that decomposition into a mixture of chalcogenide and halide is favored. Values in parentheses represent previous DFT predictions.[56]

Li-based Compounds	E_d (meV/atom)	Na-based Compounds	E_d (meV/atom)	K-based Compounds	E_d (meV/atom)
Li_3OF	55.1	**Na_3OF**	55.6	**K_3OF**	30.1
Li_3OCl	11.1 (13.9)	**Na_3OCl**	0.2	**K_3OCl**	-1.7
Li_3OBr	21.9 (25.8)	**Na_3OBr**	-23.9	**K_3OBr**	-17.1
Li_3OI	87.0	**Na_3OI**	-18.7	**K_3OI**	-38.0
Li_3SF	67.6	**Na_3SF**	44.9	**K_3SF**	27.3
Li_3SCl	67.7	**Na_3SCl**	63.6	**K_3SCl**	57.7
Li_3SBr	56.7	**Na_3SBr**	49.7	**K_3SBr**	51.4
Li_3SI	44.1	**Na_3SI**	27.1	**K_3SI**	33.2
Li_3SeF	57.5	**Na_3SeF**	28.9	**K_3SeF**	18.4
Li_3SeCl	73.1	**Na_3SeCl**	68.9	**K_3SeCl**	59.4
Li_3SeBr	64.3	**Na_3SeBr**	60.2	**K_3SeBr**	57.9
Li_3SeI	51.6	**Na_3SeI**	41.4	**K_3SeI**	45.3

Thermal stabilization. Previous studies showed that LOC unstable at zero Kelvin can becomes stable at elevated temperatures around 500 K.[81,86] Indeed, most of unstable APs also can

be stabilized by thermal effects at elevated temperatures. Predicted stabilization temperatures of APs are listed in Table 4.5. The predicted stabilization temperature of LOC is 500 K, very close to the previous predictions (480 and 532 K).[81,86] However, the stabilization temperature of Li_3SI (1121 K) does not agree with a previous prediction (520 K).[81] We believe that the difference arises from different lattice structures: the previous report treated Li_3SI with the cubic Pm-3m symmetry, whereas our study adopted the lower-energy structure with the quasi-orthorhombic structure with lattice distortions (i.e., broken symmetry with octahedra tilting). The stabilization temperature of LOB and LOI could not be predicted since the ΔG plot is almost flat with respect to the change in temperature.

Table 4.5 Predicted stabilization and melting temperatures of AP compounds (T_s and T_m, respectively). Values in parentheses are melting temperatures of corresponding alkali chalcogenide and halide, respectively.[303] Values in italics indicate the stabilization temperatures are guaranteed as its upper limit of actual values. Values with asterisk are experimental melting temperatures of existing APs.[64,65] Na_3OB and K_3OB (B = Cl, Br, I) are stable at zero Kelvin. See main discussions regarding stabilization temperatures of Li_3OB (B = Br, I).

Li APs	T_s (K)	T_m (K)	Na APs	T_s (K)	T_m (K)	K APs	T_s (K)	T_m (K)
Li_3OF	2827	460 (1711, 1121)	**Na_3OF**	2441	450 (1407, 1269)	**K_3OF**	2917	284 (1013, 1131)
Li_3OCl	*500*	555* (1711, 883)	**Na_3OCl**	0	528* (1407, 1075)	**K_3OCl**	0	364 (1013, 1044)
Li_3OBr	-	553* (1711, 823)	**Na_3OBr**	0	528* (1407, 1020)	**K_3OBr**	0	463 (1013, 1007)
Li_3OI	-	561 (1711, 742)	**Na_3OI**	0	513* (1407, 934)	**K_3OI**	0	451 (1013, 954)
Li_3SF	1928	461 (1645, 1121)	**Na_3SF**	*1139*	447 (1445, 1269)	**K_3SF**	1335	397 (1221, 1131)
Li_3SCl	2595	391 (1645, 883)	**Na_3SCl**	2169	368 (1445, 1075)	**K_3SCl**	2668	291 (1221, 1044)
Li_3SBr	1535	410 (1645, 823)	**Na_3SBr**	*1037*	383 (1445, 1020)	**K_3SBr**	1191	285 (1221, 1007)
Li_3SI	1121	431 (1645, 742)	**Na_3SI**	*576*	393 (1445, 934)	**K_3SI**	*831*	315 (1221, 954)
Li_3SeF	*997*	548 (1575, 1121)	**Na_3SeF**	*688*	570 (1148, 1269)	**K_3SeF**	*733*	381 (1073, 1131)
Li_3SeCl	3099	355 (1575, 883)	**Na_3SeCl**	2477	319 (1148, 1075)	**K_3SeCl**	2718	254 (1073, 1044)
Li_3SeBr	2287	367 (1575, 823)	**Na_3SeBr**	1891	338 (1148, 1020)	**K_3SeBr**	2396	275 (1073, 1007)
Li_3SeI	1641	398 (1575, 742)	**Na_3SeI**	*946*	360 (1148, 934)	**K_3SeI**	1162	302 (1073, 954)

Figure 4.6 shows the strong linear correlation between the stabilization temperature and the tolerance factor. It implies that higher instability induced by greater lattice distortions increases the stabilization temperature. Although located in a different *t* factor range from normal APs, F-centered compounds (having F anion at octahedron center) also show the same trend. We expect that compounds with lower stabilization temperatures would be easier to be meta-stabilized at low temperatures, because metastable solid phases may be achieved by controlled rapid cooling to room temperature.[64,81,193,194] Stabilized phases at high temperatures might be kinetically retained as metastable phases at lower temperatures.[88]

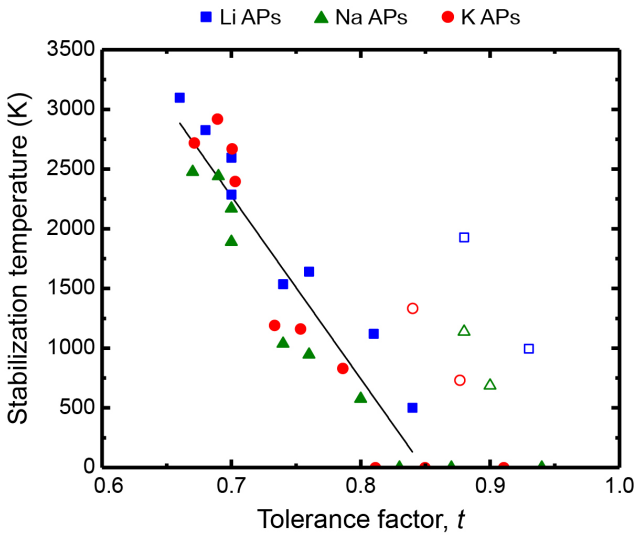

Figure 4.7 Correlation between the tolerance factor and the stabilization temperature of APs. The linear fitting is implemented excluding 'F-centered' compounds (unfilled shapes) and also compounds stable at zero Kelvin.

A previous study on the thermodynamic stability of (anti-)perovskite crystals gives a clue to estimate the threshold limit for a realizable stabilization temperature. Schmidt et al. suggested that among (anti-)perovskite compounds in the Materials Project database with an ICSD number, 41% of them are metastable and 63% of metastable phases have a distance to convex hull below 50 meV/atom (i.e., $E_d \leq 50$ meV/atom).[195] It implies that compounds with $E_d < 50$ meV/atom have a high chance to be synthesized. Figure 4.7 shows the stabilization temperature as a function of the decomposition energy E_d. The stabilization temperature increases slowly when $E_d < 50$

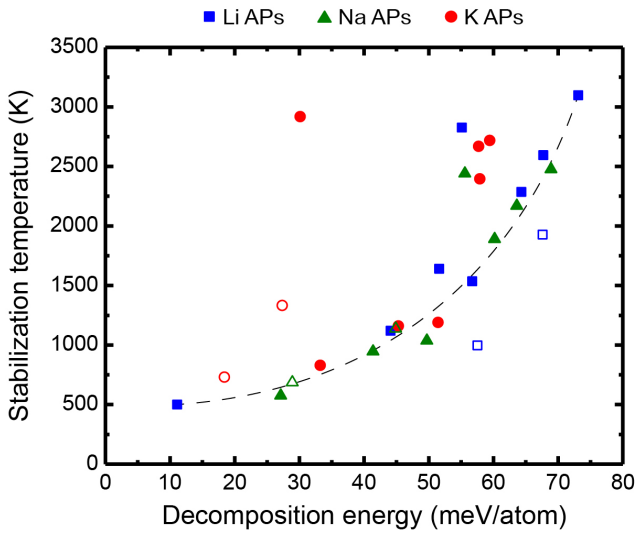

Figure 4.6 Stabilization temperatures of AP compounds as a function of the decomposition energy at zero Kelvin. Unfilled shapes denote 'F-centered' compounds. The dashed curve is a guide.

meV/atom, and APs with E_d = 40 ~ 50 meV/atom have stabilization temperatures about 1000 K. Therefore, we assume that the threshold limit of realizable stabilization temperatures is about 1000 K. Thermal effects at this temperature can overcome 50 meV/atom with a ΔS = 5 J/mol·K (actual order of magnitude between thermodynamically competing phases).[88] However, the stabilization temperature increases rapidly with larger E_d. It indicates that the synthesis probability decreases significantly with E_d > 50 meV/atom. This is coincident to the previous result that the number of metastable compounds with E_d > 50 meV/atom reduces rapidly.[195]

Chemical stability window. Most of APs are not stable at 0 K as shown in Figure 4.5. Thus, the decomposition of AP into chalcogenide and halide is assumed to be kinetically suppressed within the chemical stability window.[66] Figure 4.8 shows the stable voltage range relative to chemical reduction/oxidation reactions. The result agrees with a previous study that LOC is thermodynamically stable against Li metal in a range of voltage between 0 – 3 V.[34] Also, experiments using a Li-LOC-Li symmetric cell and SEM images reported that LOC is compatible with a Li-metal anode.[67,68] All AP compounds are stable at 0 V, implying no reduction against the direct contact to aa metal anode. Therefore, AP system is advantageous to use a metal anode and build all-solid-state batteries with high energy densities, whereas most of SEs, including $Li_{10}GeP_2S_{12}$, Li_6PS_5Cl, $Li_{0.34}La_{0.51}TiO_{2.94}$, and $Li_{1.3}Al_{0.3}Ti_{1.7}(PO_4)_3$, are inherently unstable against a Li-metal anode.[36] Viable voltage ranges are 1.9 – 2.9 V for Li APs, 1.1 – 1.9 V for Na APs, and 1.1 – 1.4 V for K APs; the range is lower with larger alkali cation.

Potential compounds for SE. The predicted stabilization temperatures were compared to the limiting barriers of vacancy and dumbbell to discover promising APs for SEs with low percolating barriers as well as low instabilities (Figure 4.9). It shows that compounds with low

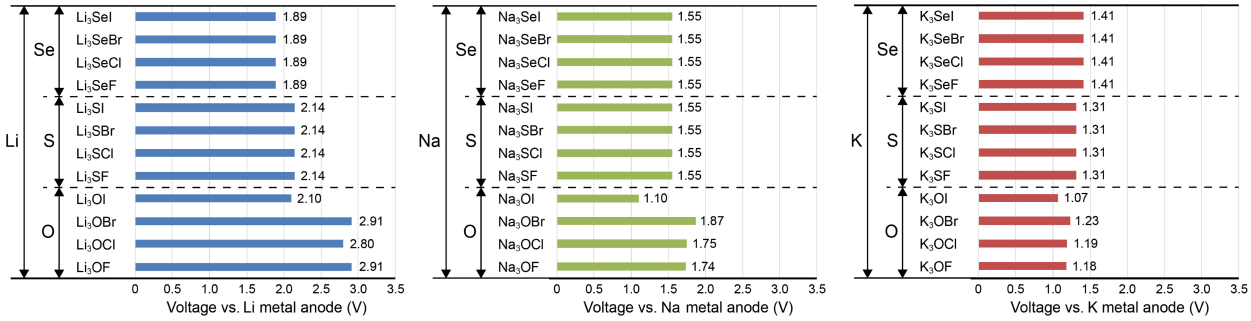

Figure 4.8 Chemical stability window of AP compounds. All APs are stable against metal anode without applied potential. Values on bars are viable voltages as SEs.

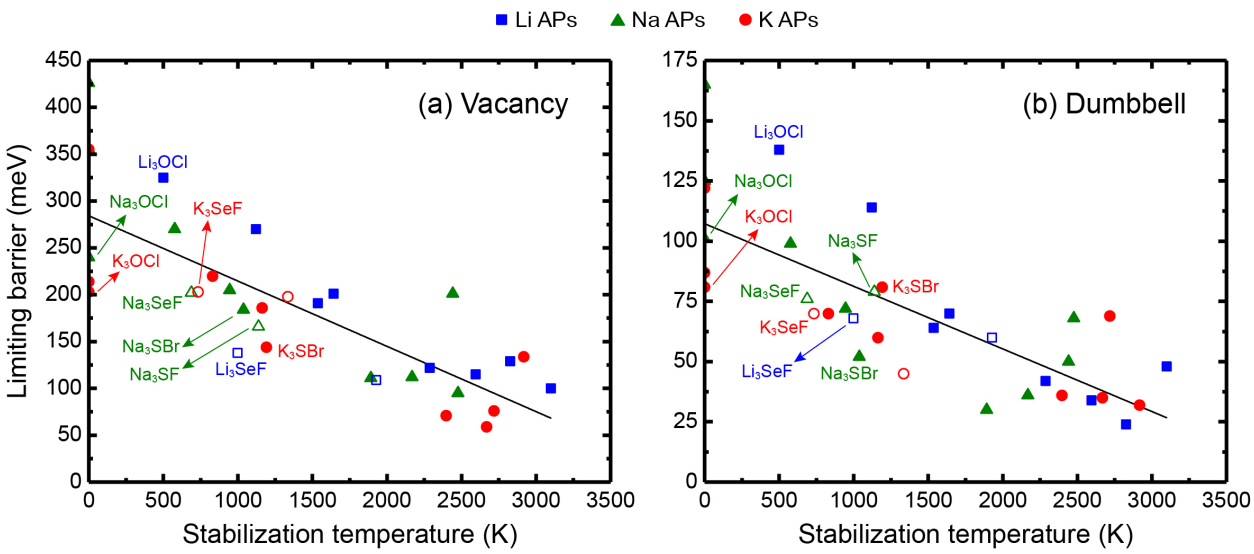

Figure 4.9 Comparison between the stabilization temperature and the limiting barrier of APs for (a) vacancy and (b) dumbbell mechanisms. APs suggested as promising SEs are labelled. Unfilled shapes denote 'F-centered' compounds.

percolating barriers have high stabilization temperatures (i.e., mobility/stability tradeoff). Li_3SeF, Na_3SeF, and K_3SeF have vacancy and dumbbell limiting barriers (138 and 68 meV of Li_3SeF, 202 and 76 meV of Na_3SeF, and 203 and 70 meV of K_3SeF) lower than LOC, NOC, and KOC, respectively, and they also have moderate stabilization temperatures (997, 688, and 733 K of Li_3SeF, Na_3SeF, and K_3SeF, respectively). Na_3SBr, Na_3SF, and K_3SBr have even lower vacancy and dumbbell limiting barriers (184 and 52 meV of Na_3SBr, 166 and 79 meV of Na_3SF, and 144 and 81 meV of K_3SBr) which come at a cost to relatively higher stabilization temperatures (1037, 1139, and 1191 K, respectively) than Na_3SeF and K_3SeF. Having stabilization temperatures near or lower than the assumed realizable stabilization temperature of 1000 K, aforementioned APs Li_3SeF, Na_3SeF, Na_3SBr, Na_3SF, K_3SeF, and K_3SBr might be synthesized at elevated temperatures. Therefore, we suggest Li_3SeF, Na_3SeF, Na_3SBr, Na_3SF, K_3SeF, and K_3SBr as potential SE materials. They will be stable with a metal anode, and viable voltages will be 1.89 V for Li_3SeF, 1.55 V for Na_3SeF, Na_3SBr, and Na_3SF, and 1.3 – 1.4 V for K_3SeF and K_3SBr. As mentioned, Na_3SI is recommended as a starting point for synthesis efforts because it has the lowest stabilization temperature (576 K) close to that of already synthesized LOC (500 K).

The predicted stabilization temperature of AP is guaranteed as a high limit of its actual value if it is higher than the melting temperature of AP and also lower than the melting temperatures of corresponding chalcogenide and halide end members. (Predicted melting

temperatures of APs are listed in Table 4.5) This is because the free energy of an AP at liquid phase above its melting temperature decreases faster than that at solid phase below the melting temperature, whereas there is no change in the decrease in free energies of end members since they remain as solids. Thus, the decrease in ΔG becomes steeper at temperatures above AP's melting point and the stabilization temperature becomes lower. It implies that actual stabilization temperatures of suggested potential compounds Li_3SeF, Na_3SeF, Na_3SBr, Na_3SF, and K_3SeF (except K_3SBr) can be lower than predicted values. Also, the actual stabilization temperatures can be further lower if quasi-orthorhombic APs undergo a phase transition like KOC (orthorhombic α-KOC undergoes a phase transition to cubic β-KOC at 364 K)[183] because high-temperature phases have lower free energies than low-temperature phases at temperatures above the transition temperature.

4.3.4 Mechanisms for Increasing Mobility

Figure 4.10 illustrates the mechanisms underlying the connections between distortions and the migration barrier. The migration barrier for an ion hop, E_b, is defined as the difference in energy between the transition state (TS) and the equilibrium state (ES): $E_b = E_{TS} - E_{ES}$. Thus, E_b can be impacted by changes to TS, to ES, or to both. The grey dashed curve in Figure 4.10 illustrates these energy levels on a model potential energy surface (PES) from an AP having limited lattice distortions ($t \sim 1$). Previously, it was shown (Figures 4.5 and 4.6) that larger lattice distortions

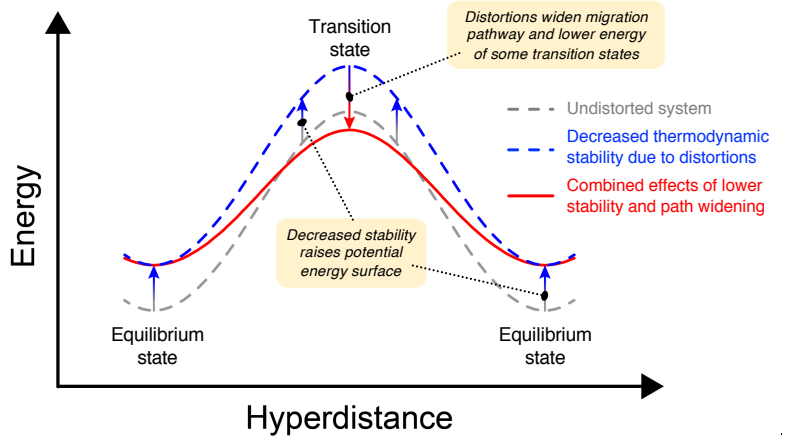

Figure 4.10 Cartoon depicting the effects of lattice distortions on the energy barrier for ion migration in APs. Grey dashed curve: energy profile for migration in an undistorted system. Blue dashed curve: energy profile for a system with reduced thermodynamic stability arising from lattice distortions. Red curve: profile accounting for the combined effects of reduced stability and widening of the migration pathway.

correlate with reduced thermodynamic stability. The impact of reduced stability on the PES is shown by the blue dashed curve in Figure 4.10. In this case the PES is shifted towards higher energies.

Concomitantly, these same lattice distortions can result in path widening at the transition state, offsetting the increase in energy to E_{TS} arising from lowered stability (red curve in Figure 4.10). For example, earlier studies have shown that increasing the width of the cation migration channel can lower E_b by lowering E_{TS}.[46,64] Figure 4.11 shows the correlation between E_b for elementary hops and the width of the ion migration channel for the vacancy mechanism,

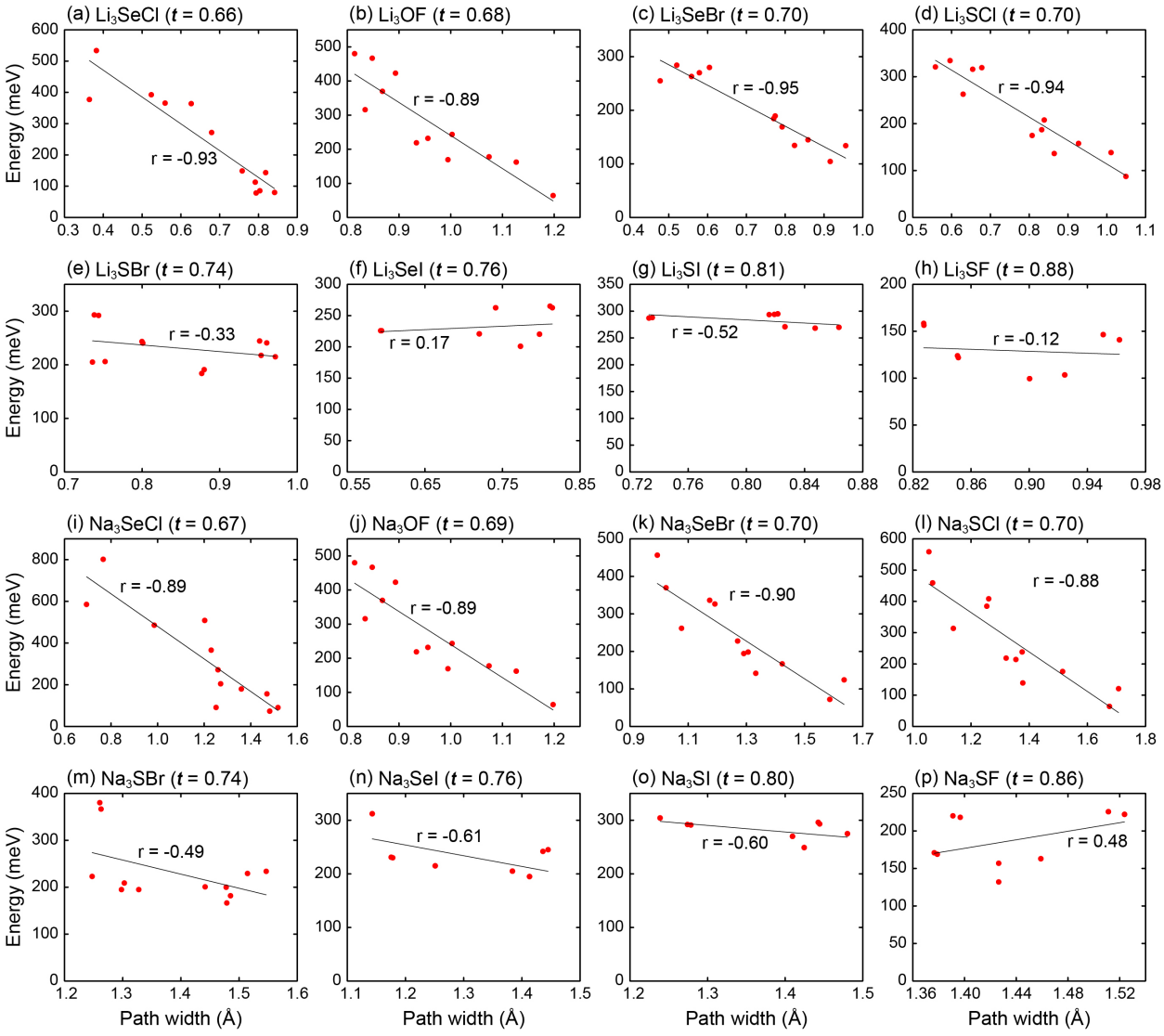

Figure 4.11 Correlation between path width and elementary barrier energies for vacancy migration in the distorted (a-h) lithium and (i-p) sodium APs. r values represent Pearson correlation coefficients.

respectively. These data show that in most compounds a wider channel width results in smaller E_b. Although not presented, K-APs show the same trend. This correlation is much weaker for the interstitial mechanism, most likely because the path-widening effects are subsumed within the formation enthalpy of the interstitial. Thus, lattice distortions can influence E_{TS} (and thus E_b) for the vacancy mechanism by introducing migration pathways with wider channels. In total, the combined effects of lower stability and path widening result in a smaller net migration barrier for a subset of the available migration pathways.

4.3.5 Characterizing Difference in Mobilities between Alkali Ions

Although Na and K chemistry seems to be very similar to Li, sometimes Li battery technologies cannot be directly applicable to Na and K batteries.[196] There is a number of studies that compared different behaviors of Li, Na, and K ions in battery materials. Previous DFT studies regarding alkali ions in graphite predicted that 1) Li and K-ion intercalation is energetically favorable whereas Na ion is not, 2) K-ion migration via vacancy mechanism is even better than Li ion, and 3) preferred stacking sequences of alkali ions are different according to intercalation stages.[197–199] Co-intercalation of both alkali ions and ether molecules in the form of solvated ions into graphite was observed when using an ether-based electrolyte.[200] This is because larger cation ion size leads to wider interlayer distance of graphite and reducing repulsion between negatively charged graphite layers in the discharged states, which results in increasing in stability and higher alkali-ion storage potential.[200] Intercalation experiments of alkali ions into K_xVPO_4F electrode show that a K-cell has distinct voltage plateaus due to the high K^+/vacancy ordering resulting from strong interactions between K ions, whereas voltage plateaus of Li and Na-cells are less obvious.[201]

Contrary to expectations based on ionic radii, K ion have faster diffusion than Li and Na ions in liquid organic electrolytes and a molecular ionic solid $M_6[Rh_4Zn_4O$ (L-cysteinate$)_{12}] \bullet nH_2O$.[202–205] Comparing APs with the same anions (e.g., between Li_3OCl, Na_3OCl, and K_3OCl) leads to the clear investigation of the difference in diffusive behavior between alkali cations in solids: the comparison is confined within the same structural/chemical/mechanical system. Also, it allows to reveal important factors for fast ion mobility vailed behind the effect of lattice distortion, since APs with the same anions have almost the same degree of lattice distortions (i.e., similar t factors). Figure 12(a) indicates that roughly limiting barriers of larger alkali cation are lower than those of smaller one. We found that four lattice/electronic characteristics are

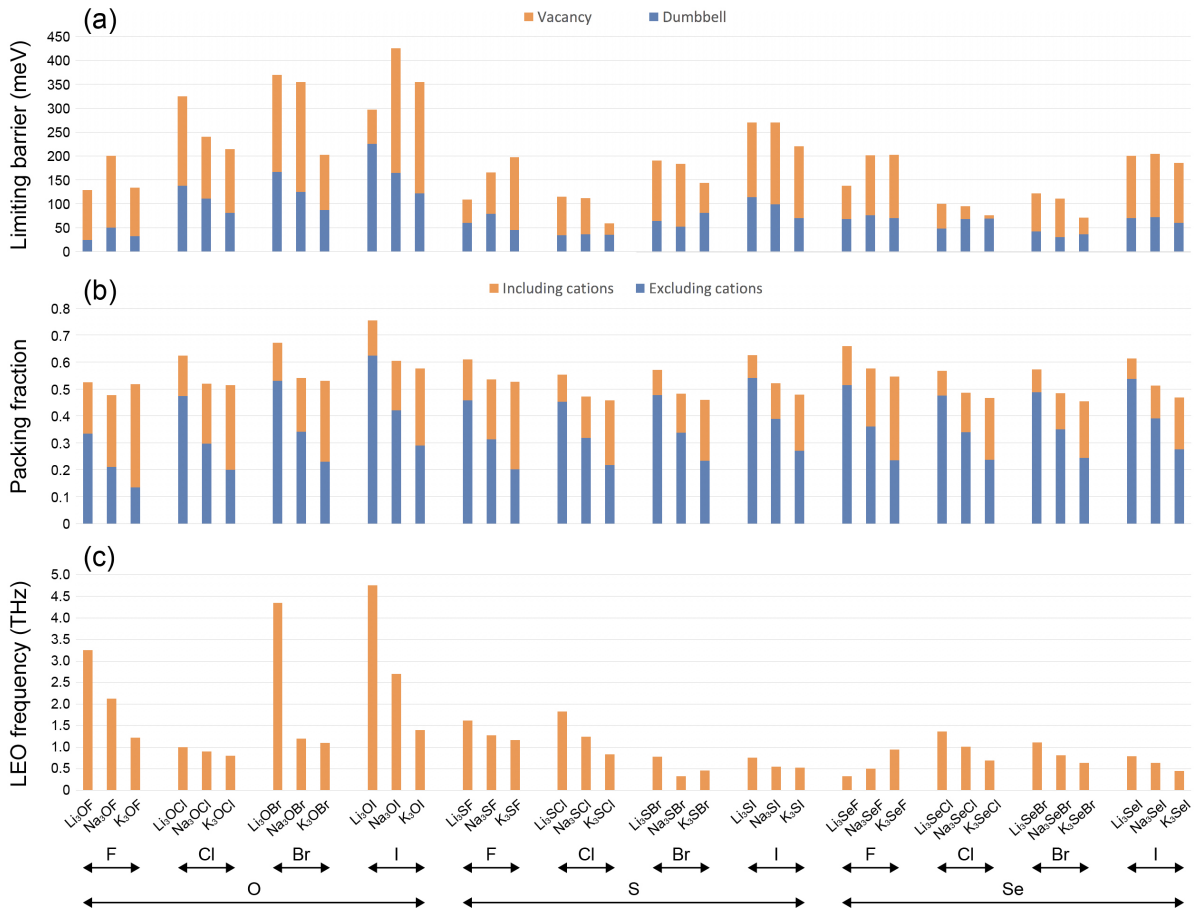

Figure 4.12 Comparison of (a) limiting barriers of vacancy and dumbbell, (b) packing fractions with and without cation, and (c) LEO frequencies between Li, Na, and K APs with the same anions.

responsible for the difference in mobility between alkali cation in AP lattice: *packing fraction*, *lattice dynamics*, *polarizability*, and *Bader charge*.

A wider space will provide better lattice environment for transports of mobile ions.[38,46] Packing fraction is a simple but intuitive indicator showing how much free space is available for diffusive motion of ions. The packing fraction was evaluated using the iterative method with ionic radii of elements.[39] Figure 12(b) shows that packing fractions of K APs are the smallest while those of Li APs are the largest. Thus, K ions are much freer than Li and Na ions to migrate in the lattice. The difference becomes more apparent with the packing fraction excluding cations because of the difference in ionic radii. It implies that larger cation has a significantly wider free space around vacancy sites than smaller cation to migrate in. Therefore, K ions are less hindered by space and may have lower limiting barriers. It is also notable that compounds with smaller halogen anions (except F-centered APs) have lower packing fractions and thus have lower limiting barriers.

Lattice dynamics has been suggested as a factor that can control the ion mobility. The activation energy of self-diffusion behavior in bcc metals is correlated with the longitudinal-acoustic 2/3<111> phonon frequency (the largest diffusivity with the strongest softening).[206] Low-energy optical phonons (LEO, transverse-optical phonon with the lowest frequency) enhance the phonon amplitude and assist the jump of mobile ions; the activation energies of binary and ternary ion conductors are proportional to the square of the LEO frequency.[42] A recent study discussed that low vibration frequencies of Li ion enhance the ion mobility.[43] Figure 12(c) shows that K APs have lower LEO frequencies than Li and Na APs. It implies that K ions have greater amplitudes than other ions, resulting in lower percolating barriers. Therefore, our result also suggests that ion mobility is correlated with lattice dynamics.

Polarizability affects to the softness of lattice and electron clouds. The electronic polarizabilities $\bar{\alpha}$ of AP compounds were calculated by the Clausius-Mossotti relation using predicted electronic dielectric constants ϵ,[207]

$$\bar{\alpha} = \frac{3}{4\pi}\left(\frac{\epsilon - 1}{\epsilon + 2}\right) v_{at}, \tag{4.11}$$

where v_{at} is the volume per atom. It was shown that the increase in polarizability results in decreasing lattice stiffness and in turn yields lower activation energies.[44] Our result shows that AP compounds with larger cation have higher polarizability, Figure 13(a). Thus, the increase in polarizability leads to reduced limiting barriers, a good agreement to the previous report.[44] Our previous report presumed that the lattice distortion effect is greater than the effect arising from the polarizability because APs with larger halogen anion have lower degree of distortion and higher limiting barrier, but also higher polarizability.[208] Here, the comparison between APs with controlled degree of distortions suggests that the polarizability effect indeed exists in the AP system. Therefore, we confirm that the polarizability is one of the descriptors for ion mobility and not negligible, but the distortion effect is greater than the polarizability effect.

High polarizabilities also indicate the readiness of electron-cloud distortion. The polarizability of alkali ion was estimated by averaging reported values in chalcogenide and halide (e.g., averaging α_{K} of K_2O and KCl to estimate α_{K} of K_3OCl), and polarizabilities of anions were adopted from chalcogenides and halides (e.g., α_{O} and α_{Cl} of K_3OCl from those of K_2O and KCl, respectively).[209,210] Figure 13(b) shows that the polarizability of K ion is several times larger than

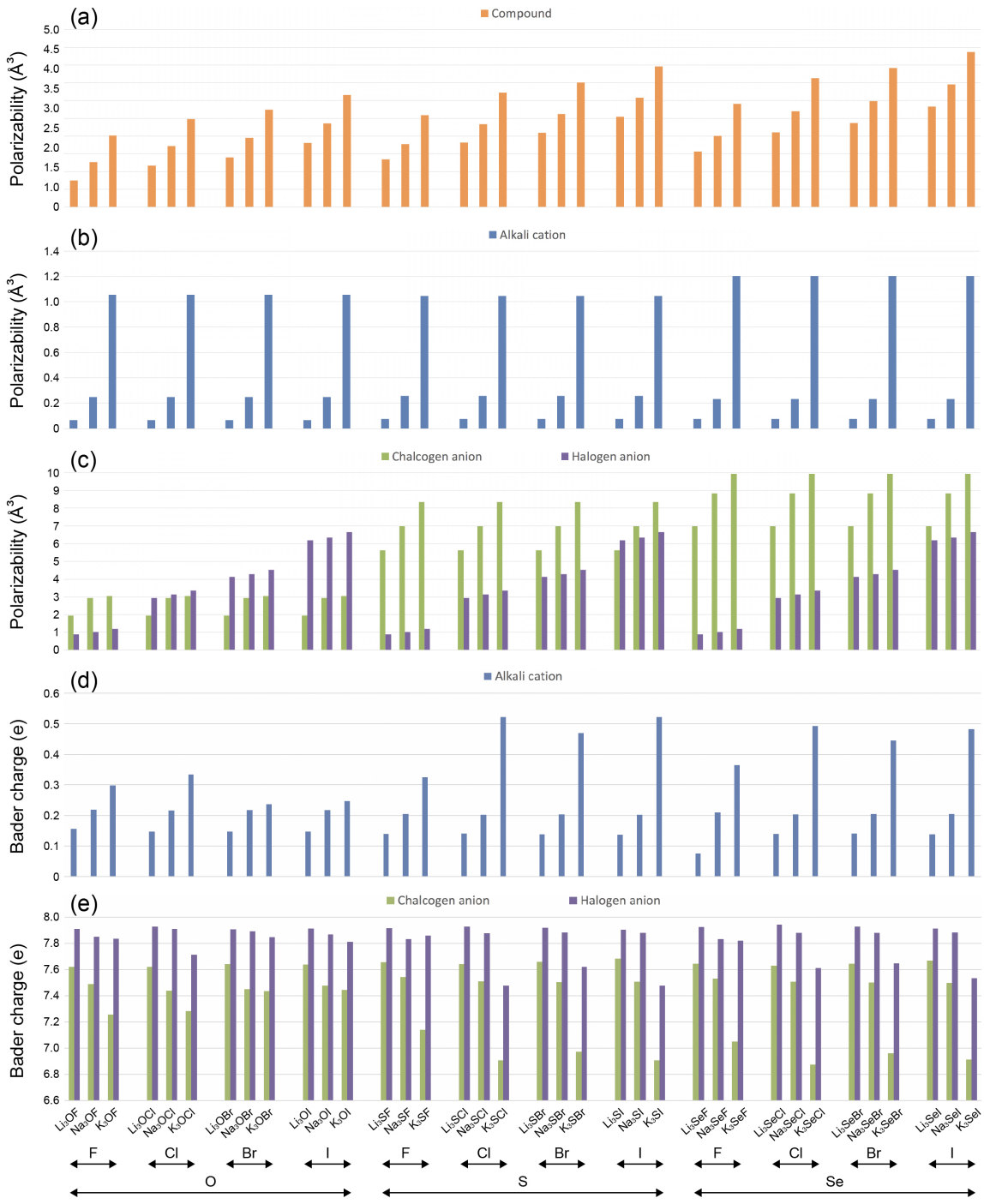

Figure 4.13 Comparison of (a-c) polarizabilities and (d-e) Bader charges between Li, Na, and K AP with the same anions.

those of other cations. Thus, K ions are flexible to move through narrow channels made by adjacent anions and less affected by repulsive forces, whereas Li ions are close to rigid spheres more likely to be interfered by anions and difficult to pass nearby. It is also remarkable that polarizabilities of an anion in different compounds are not the same, i.e., anion polarizability is higher in APs with

larger cation, Figure 13(c). It implies that anions in K APs are also soft enough to allow K ions to pass nearby readily, whereas the same anions in Li and Na APs are less generous in their cations.

The Bader charge defines individual atoms in crystal or molecule, and is useful to approximate the total electronic charge of an atom.[211,212] We used the Bader-charge analysis code along with obtained electron densities to evaluate actual charges of ions.[212–215] The Bader charge was averaged over the same species in the lattice. Figure 13(d) shows that the Bader charge of Li ion is less than 0.15, which means that its net charge is higher than +0.85 (fully ionized when the Bader charge is 0 for cations and 8 for anions). Similarly, net charges of Na and K are about +0.8 and +0.5 ~ +0.75, respectively. It indicates that larger cations are less charged, thus they will be less attracted by anions and can have higher mobilities than smaller cations. The charges of chalcogen and halogen anions in Li APs are about -1.65 and -0.9, whereas those in K APs are also less charged (in a range of -0.9 ~ -1.4 and -0.5 ~ -0.85, respectively) to make a charge balance with less-charged K ions in the lattice, Figure 13(e). Consequently, the electrostatic attraction between cation and anions in K APs are much weaker than those of Li and Na APs, and therefore K ions are less affected by the electrostatic attraction and can have higher mobility than smaller cations. Note that lower net charges increase the ionic radius of cation but also decrease ionic radii of anions, thus the effect of net charge on ionic radii and spatial aspects will be cancelled out.

This conclusion is similar to other studies that K ions feel less drag forces than Li and Na ions: due to weaker Lewis acidity in organic liquid electrolytes, solvated K ions have smaller Stokes radius than solvated Li and Na ions.[202,204] Weaker Lewis acids are less likely to accept an electron pair from a Lewis base and form a Lewis addict (combined product of acid and base).[216] Also, hydrated K ions have smaller hydration radius than hydrated Li and Na in a molecular ionic solid.[205] Thus, K ions have higher mobility resulting from weaker drag forces, whereas Li and Na ions confront with higher barriers. Similarly, K ions in AP system do not encounter severe drag force by the electrostatic attraction and can have higher diffusivity than Li and Na ions.

Previous studies suggested the bonding nature as one of key factors for superionic conductors. A coexistence of ionic and covalent bonds can contribute to the ion diffusion when the bonds prefer different lattice configurations; the bonding fluctuation changes a local lattice configuration (e.g., between octahedral and tetrahedral configurations in AgI) accompanied by diffusive motions of ions,[217–219] helps mobile ions being relatively unconstrained via a mobile

transition zone,[220] and provides temporary metastable sites by perturbing the Coulomb potential.[221] The Bader charge analysis in this work also suggests the importance of the bonding nature. The reduction in net charges of ions indicates that bonds in K APs are less ionic than those in Li and Na APs (covalency effect),[222] and the weaker ionicity in K APs helps K ions less constrained by the electrostatic attraction and suppresses corrugations of the potential energy surface. It agrees with a previous machine learning study that lower ionicity is preferred for superionic conductors.[39]

4.4 Conclusions

The design of new SEs will be aided by an understanding of the elementary chemical and structural features that control ionic mobility. The present study demonstrates that lattice distortions are one such feature. The connection between ionic mobility and lattice distortions was assessed across a series of 36 model anti-perovskite solid electrolytes. The degree of these distortions, quantified by the tolerance factor, *t*, was systematically varied through a sequence of isovalent substitution. DFT calculations were used to evaluate the energy barriers for all relevant ion migration pathways of vacancy and interstitial mechanisms, thermodynamic stabilities, and properties of AP compounds.

These calculations reveal a strong correlation between the magnitude of lattice distortion and the limiting barrier for percolating ion migration: compounds with larger distortions exhibit smaller migration barriers. Consistent with earlier studies, the energetic spread between the largest and smallest migration barriers for a given compound was found to increase with the extent distortion. Hence, lattice distortions slow migration along some pathways, while speeding up others. In the case of the APs, these lower-barrier hops can be assembled into a percolating network. In addition, a higher degree of lattice distortion also correlates with diminished thermodynamic stability. The decomposition energies of APs increase with lattice distortions, thus realizing those compounds having the highest ionic mobility in this class of conductors will require balancing a tradeoff with stability.

Although most of APs are prone to decompose at zero Kelvin, they could be stabilized at elevated temperatures by thermal effects. We found a linear correlation that larger lattice distortions induce higher stabilization temperatures due to lower stability. The comparison between the stabilization temperature with long-range percolating barriers suggests that Li_3SeF,

Na_3SeF, Na_3SBr, Na_3SF, K_3SeF, and K_3SBr are 'Goldilocks' materials that balance ion mobility and stability, i.e., low percolating barriers (138 ~ 203 meV and 52 ~ 81 meV for vacancy and interstitial dumbbell mechanisms) with relatively low stabilization temperatures (688 ~ 1191 K). Therefore, we suggest Li_3SeF, Na_3SeF, Na_3SBr, Na_3SF, K_3SeF, and K_3SBr as potential materials for SEs of monovalent-ion batteries. They are predicted to be stable with a metal anode, and viable voltages will be 1.89 V for Li_3SeF, 1.55 V for Na_3SeF, Na_3SBr, and Na_3SF, and 1.3 – 1.4 V for K_3SeF and K_3SBr. Their fast pathways result from a combination of channel widening and destabilization of the equilibrium configuration.

While the APs represent a specific model system, we anticipate that the trends described here can be generalized to other classes of crystalline solid electrolytes. The present results teach us that perturbations to ion-packing, introduced via isovalent substitution, leads to lattice distortions and symmetry-breaking. These effects remove the degeneracy of the migration barriers in the non-distorted materials, and can open up ion-migration channels with potentially lower barriers. In principle, this concept could be applied to any crystalline system. Of course, this strategy has some boundaries of applicability, as very large ionic size mismatches could induce transformations to other crystal structures.

Comparisons between APs with the same anions (having similar lattice distortions) enables to investigate the difference in diffusive behavior between Li, Na, and K ions in solids. Contrary to expectations based on ionic radii, generally larger alkali ion has higher mobility than smaller one in the AP lattice. We found four lattice/electronic characteristics responsible for the trend: an AP compound with larger alkali ion has 1) a lower packing fraction that leads to wider free space for cations to move through, 2) greater vibration amplitudes (smaller low-energy optical phonon frequency) that facilitate migrations of cations, 3) higher polarizabilities that lead to softer lattice stiffness and flexible electron clouds of ions, and 4) much weaker electrostatic attraction between ions due to lower net charges (covalency effect) according to the Bader charge. Our finding implies that 'packing fraction', 'frequency' of low-energy optical phonon, 'polarizability', and 'Bader charge' are descriptors that characterize the difference in mobilities between alkali ions in solids.

In total, by clarifying the connections between lattice distortions, mobility, and stability and the origin of the difference in mobilities between alkali ions in solid, this work will aid in the design of optimal solid electrolytes.

Chapter 5 Evaluating Descriptors for Ion Mobility in Solids via Machine Learning

5.1 Introduction

It is desirable to understand important features that describe a high ion mobility in solids for the systematic design of SEs. ML can provide new insights to the design principles for SEs since it can find complicated relations between features and a target property.[223] ML has been used in a wide range of research fields, including the field of materials science for property predictions and the discovery of materials.[195,223,232,224–231] ML was also used to perform a material screening to discover new superionic conductors.[39,233–236] Especially, Jalem et al. showed that large cell volume, strong polyanion covalency, and minimized local lattice distortion around Li pathways can decrease migration barriers in the taborite system.[235] Also, Sendek et al. suggested following features as effective properties to classify superionic conductors: long distance between Li and anions, short distance between Li ions, weak ionicity of pathways, low coordination between anions, and high coordination number between Li ions.[39]

Using ML approaches with a large number of ion-migration data, this study aims to systematically understand chemical, physical, and/or structural features that describe the ion transport through a lattice, their relative importance, and how they promote a high ion mobility. As shown in Chapter 4, DFT simulations predicted energy barriers of over 300 elementary paths of ion migration via vacancy and interstitial dumbbell mechanisms, using 36 model AP compounds (X_3AB, where X = Li, Na, or K, A = O, S, or Se, and B = F, Cl, Br, or I). We will perform a ML analysis on the elementary paths (target value = energy barrier) with descriptors that contain the information about migration environments of elementary paths as well as properties of compounds, which leads to detail investigations on defect migrations in the lattice structure.

Descriptors are collected based on low-energy structures and their properties predicted in previous DFT calculations, and ML analysis is performed on vacancy and interstitial dumbbell mechanisms separately. Before ML model training is implemented, redundant features are reduced

by the Pearson correlation analysis. This step makes ML models simpler and decreases the risk of overfitting. The best ML model is selected by optimizing 18 different ML algorithms (9 linear, 3 support vector, and 6 tree-based regression algorithms) using the stratified 10-fold cross-validation on the training set (80% of entire data set) and comparing their prediction performance on the test set (the rest 20% of entire data set). Using the best model, feature subsets are evaluated to determine the most predictive features to describe ion migrations. Finally, relative importance of features in the best subset and their influence on ion transport are also analyzed.

The result reveals that lattice properties have the greatest influence in defect migrations regardless of mechanisms. The path distance (29%) and bottleneck-related features (path width by the first closest ion 23%; total path width 17%; packing fraction without cation 9%) appear as the most important features for vacancy, accounting for 78% of the total importance. A simplified ML model with an aggressive feature filtering also show that the path distance (42%) and total path width (28%) appear as top 2 features, which further supports our analysis. The elementary migration barrier decreases with a shorter path distance and wider bottleneck for migration, thus decreasing the distance between mobile cations and keeping framework ions away from paths will be helpful for the lattice design with a high vacancy mobility.

Similar to vacancy, bottleneck-related features also appear for interstitial dumbbell, occupying a 73% importance (total path width 40%; cation – framework anion distance 19%; packing fraction without cation 14%). However, the path distance is not shown as an important factor for dumbbell because of the concerted motion of three cations that shortens the effective migration distance than the linear distance between cation sites. Rather than modulating electronic or chemical properties, therefore, tuning lattice structure will be the most effective scheme to improve ion mobility. In total, this stochastic study gives a thorough analysis of ion migration with comprehensive features including detail environments of elementary paths as well as compound properties, and will aid in the systematic design of SEs for SSBs.

5.2 Methodology

The entire process performed to select the ML model and find the best descriptive features is shown in Figure 5.1. We performed the ‘feature filtering’ to reduce redundant descriptors and the ‘model selection’ to choose an algorithm that derives the best model for our data. Then, the

most predictive feature subset was found by the 'wrapper' method that iteratively evaluates the performance of descriptor subsets.[237] The *scikit-learn* ML package with the *Python* programming language was adopted to implement ML modeling.[238]

5.2.1 Feature Filtering

The filtering is a feature selection method to reduce the dimension of feature space by eliminating redundant descriptors. It helps to reduce a computational burden and the risk of overfitting. The relations between descriptors were assessed by the Pearson correlation[239]

$$\rho_{X,Y} = \frac{cov(X,Y)}{\sigma_X \sigma_Y}, \tag{5.1}$$

where $cov(X,Y)$ is the covariance of features X and Y and $\sigma_{X \text{ or } Y}$ is the standard deviation of the feature X or Y. The coefficient measures the degree of a linear correlation between X and Y in a range of $-1 \leq \rho \leq 1$, where 0 means no correlation and ± 1 means a perfect positive/negative correlation. Descriptors that show a nearly perfect correlation to the other feature ($|\rho| \geq 0.94$) were filtered to minimize the risk that important descriptors might be ruled out unintentionally. Although having a high correlation, descriptors were not eliminated when their physical meanings are not directly related; for example, one of descriptors 'volume per atom' and 'polarizability' was not filtered despite of a high correlation between them ($\rho = 0.97$).

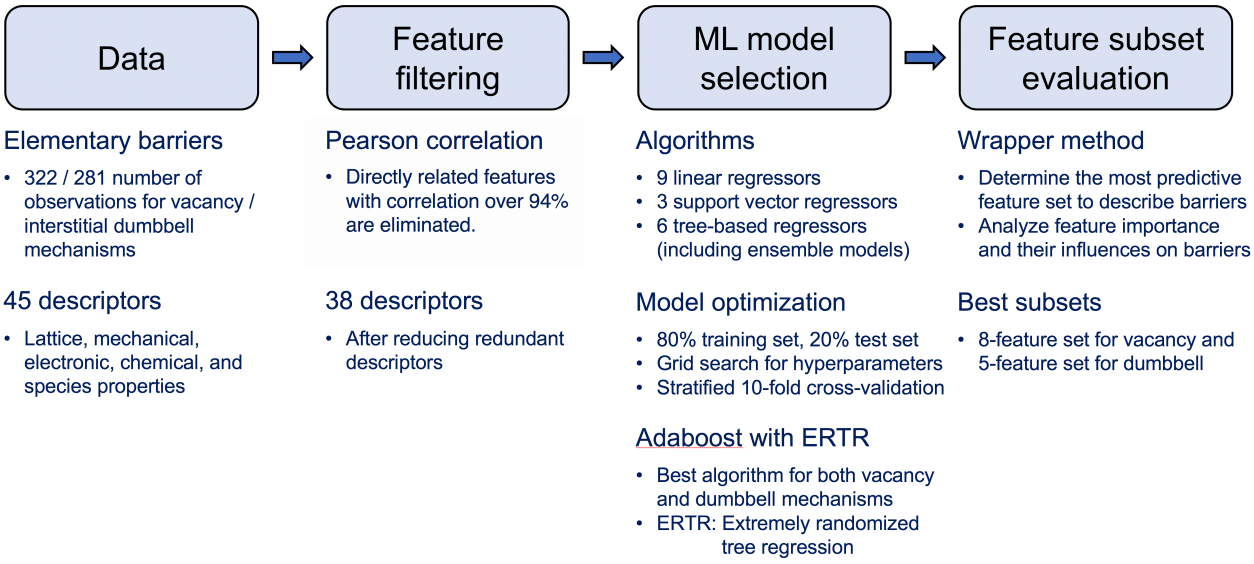

Figure 5.1 Entire process to find useful features to describe ion migration barriers. 7 redundant features were reduced by the filtering, and the rest 38 features were used to optimize ML algorithms and select the best model. The most predictable feature subset was found by the wrapper method which iteratively evaluates different feature subsets.

5.2.2 Model Selection

We evaluated 18 algorithms to find the best model, including 9 linear regressors, 3 support vector regressors (SVR), and 6 tree-based regressors. The *ridge*[240] and *LASSO*[241] linear regressions regularize the error function (sum of squared errors) by adding a penalty (L2 or L1 norm), so that they can shrink coefficients and prevent overfitting (single hyperparameter that controls the magnitude of the regularization). The *elastic net* uses both L1 and L2 norms with an additional hyperparameter that controls the ratio between contributions of two penalties.[242] This algorithm performs better than LASSO when some features are correlated.[242] The *Bayesian ridge regression* is a sequential learning process by updating a probability of model coefficients (in terms of prior and posterior), which inherently includes the regularization term (L2 norm) like the ridge regression.[243] The *Bayesian automatic relevance determination (ARD) regression* is a modified version of the Bayesian ridge regression to assign separated regularization hyperparameters to model coefficients, which is effective when data contains irrelevant features.[244] The regularization hyperparameter(s) in the Bayesian models are optimized automatically during the fitting. The *Huber* regression is basically the same to the ridge regression, but it uses an absolute error for outliers so that a model is less sensitive to them (an additional hyperparameter controlling a threshold to decide outliers).[245] The *passive-aggressive regression* (*PAR*) is a margin-based online (iteratively updating) regression algorithm using the hinge loss (allowing errors when they are within a margin, otherwise the linear L1 error is used), which is suitable for large-scale data (two hyperparameters for regularization and the magnitude of margin).[246] The random sample consensus (RANSAC) is an iterative algorithm to find inlier samples that will be used to train the final model (a hyperparameter controls the ratio of random subsamples to total samples). The RANSAC was implemented with the ridge and LASSO regressors (namely *RANSAC + Ridge* and *RANSAC + LASSO*, respectively).

SVR is a regression version of the support vector machine (SVM) classifier that uses a separating hyperplane with a soft margin allowing some extent of misclassification.[243] The e*psilon-SVR* determines support vectors (i.e., misclassified samples) using the margin area and minimizes the regularized hinge loss with the support vectors (hyperparameters C and ϵ for regularization and the magnitude of margin, respectively).[243,247,248] The *linear-SVR* is the same to the epsilon-SVR but uses a different solver suitable for large-scale data.[249] The *nu-SVR* replaces the

hyperparameter ϵ by ν that controls the number of support vectors (ratio of data outside the margin to entire data).[243,248,250]

The *decision tree regression* (*DTR*) constructs decision criteria (e.g., $x_1 \geq \theta_1$, $x_2 < \theta_2$, $x_2 \geq \theta_3$, etc., where x are features and θ are feature values for thresholds) so that samples are divided into leaves of a tree-like structure.[243,251] A fully-grown (over-complex) decision tree is likely to suffer from overfitting, so adjusting a decision tree (i.e., 'pruning') can improve the predictive accuracy.[252] The adjustable hyperparameters are (1) the minimum number of samples to split, (2) the minimum number of samples at a leaf, (3) the maximum depth of the tree, and (4) the maximum number of features considered at each split. The *random forest regression* (*RFR*) averages tree models trained with random samples, a technique called 'bootstrap aggregating (bagging)' that improves the prediction (an additional hyperparameter controlling the number of tree models).[253–255] The *extremely randomized tree regression* (*ERTR*) is similar to RFR, but further randomizes each tree model by arbitrarily selecting cut-point choices.[256] The *boosting* is a technique that multiple weak learners (models slightly better than random) built by a sequence learning can perform better than any single model.[243] The 'adaptive boosting (adaboost)' algorithm gives greater weights to training samples with higher errors shown in a previous weak model.[257,258] We implemented adaboost algorithm with RFR and ERTR as weak models (namely *adaboost + RFR* and *adaboost + ERTR*, respectively). The *gradient boosting regression tree* (*GBRT*) successively fits a new model to residual errors (difference between data and prediction) shown in a previous step, and adds the predicted residuals to the previous prediction.[259]

The dataset was randomly divided into training and test sets. The training set comprised 80% of the dataset and the remaining 20% was used as test data. It was confirmed that these two sets have a similar distribution of elementary barriers: the mean and standard deviation of the training set was 262 meV and 136 meV, respectively, while for the test set the mean and standard deviation are 268 meV and 145 meV, respectively. (For comparison, the mean and deviation of the entire data are 262 meV and 138 meV). The hyperparameter optimization of a regression algorithm was done by a grid search with the stratified 10-fold cross-validation (CV). We divided the training samples into 10 validation sets evenly so that the maximum difference between the mean target values of validation sets is less than 10% of the mean target value of the entire training set. A literature showed that 10-fold is a reasonable choice, a stratification is generally a better scheme than a regular CV for both bias and variance, and the stratified 10-fold CV may be better

than the more expensive leave-one-out CV for the model optimization.[260] The test set was not involved in the model optimization process, but was used to estimate the prediction power of the optimized model of each algorithm after training. The algorithm that shows the best performance (i.e., the smallest error) was selected to perform the evaluation of feature subsets.

5.2.3 Feature Subset Evaluation

The wrapper method is to find the best subset of features for ML models.[237] Thus, like filtering, it is also one of the feature selection methods. However, unlike filtering, it involves an iterative search with a ML algorithm by selecting a subset and learning the model repeatedly. Thus, it requires a significant computation time, especially when there is a substantially large number of descriptors. Here, 38 descriptors (number of features after filtering) can make a computationally burdensome number of subsets, $\sum_{n=1}^{38}\binom{38}{n}$ = about 275 billion cases. Thus, we made subsets with the number of descriptors up to 8 and larger than 32 (over 65 million subsets) and evaluated them using the selected model to find the most predictive features for ion migration. We found that this approach is sufficient to investigate important features (see results and discussions).

5.2.4 Feature Importance and Influence on Barriers

The most important part in ML studies is to analyze results from the optimized model to study the importance of features and how they affect to the target property. This is rather straightforward for linear regression models, whereas black box models like neural networks, SVM, tree models, etc. are not directly interpretable.[259]

The relative importance of features was analyzed by the *mean decrease impurity* (MDI) for tree-based algorithms, which is defined as the total decrease in impurity (classification) or variance (regression) contributed by a certain feature as[251]

$$MDI(x) = \sum_i \left[n_i var_i(x) - \left(n_{LL} var_{LL}(x) + n_{RL} var_{RL}(x) \right) \right], \tag{5.2}$$

where the sum is over nodes *i* divided by a feature *x*, *n* is the number of samples in a node *i* and its left and right leaves (denoted as subscriptions *LL* and *RL*, respectively), and *var* is the variance of target values of samples in the node and leaves. It measures how much a feature contributes to

minimize the variance of samples at nodes throughout the tree model (greater contribution with larger MDI).

The influence of features was analyzed using the *individual conditional expectation* (ICE) plot, which is inspired by Friedman's *partial dependence plot* (PDP).[259,261] PDP shows the average partial relationship and helps understanding marginal effects of features in black box models, but it may obfuscate the complexity of the modeled relationship.[259,261] In contrast, the ICE plot can suggest the variation in the fitted values by plotting estimated conditional expectation curves of all training samples.[261] The conditional expectation curve of each training sample is derived by predicting target values using the trained ML model as a function of a chosen feature while fixing values of all other features (the number of curves is the same to that of samples). Also, the predicted value at the minimum value of the chosen feature is anchored at zero for all conditional expectation curves (i.e., the centered ICE plot), so that the variation in the target becomes apparent with the increase in the chosen feature. The center curve can be derived by averaging expectation curves. The *PDPbox* package was adopted to implement the ICE analysis.[262]

5.3 Results and Discussion

5.3.1 Data for Analysis

Migration data. The energy barriers of elementary paths in 36 model APs (X_3AB, where X = Li, Na, or K, A = O, S, or Se, and B = F, Cl, Br, or I) were adopted from DFT calculations in Chapter 4. The AP lattice has a cation sublattice by vertex-sharing octahedra, thus cation defects can migrate via octahedron edges. APs with a high-symmetry cubic system have one distinct elementary path, whereas those with a lower-symmetry orthorhombic system have 12 paths (i.e., the number of edges). The number of samples is 322 and 281 for vacancy and interstitial dumbbell, respectively. The data is large enough to satisfy the rule of thumb that the number of samples needs to exceed five times of the number of descriptors to avoid the 'curse of dimensionality' (i.e., overfitting) and achieve reliable models.[263,264] Also, this large data contains not only energetically preferred (low barrier) but also undesirable (high barrier) paths, which can improve the reliability of our ML model.

Table 5.1 List of descriptors (abbreviations in parentheses) and its category. 'Filter' reduces the redundant descriptors denoted in the table (e.g., V_{octa} was reduced into V_a).

Descriptor	Category	Filter	Descriptor	Category	Filter
Volume per atom (V_a)	Lattice		Ionic radius (r_C)	Cation	EN_C
Octahedron volume (V_{octa})	Lattice	V_a	Atomic mass (m_C)	Cation	EN_C
Mass density (ρ_m)	Lattice		Electronegativity (EN_C)	Cation	
Packing fraction (PF)	Lattice		Ion polarizability (α_C)	Cation	EN_C
Packing fraction without cation (PF_C)	Lattice		Bader charge (BC_C)	Cation	
Tolerance factor (t)	Lattice		Born effective charge (BEC_C)	Cation	
Channel size (D_f)	Lattice		Ionic radius (r_O)	Octahedral anion	
Coordination number of cation (CN_C)	Lattice		Atomic mass (m_O)	Octahedral anion	
Path distance (CCD)	Lattice		Electronegativity (EN_O)	Octahedral anion	r_O
Cation – octahedral anion distance (COD)	Lattice		Ion polarizability (α_O)	Octahedral anion	r_O
Cation – framework anion distance (CFD)	Lattice		Bader charge (BC_O)	Octahedral anion	
Distance between anion (AAD)	Lattice		Born effective charge (BEC_O)	Octahedral anion	
Path width by the first closest ion (PW_c)	Lattice		Ionic radius (r_F)	Framework anion	
Path width by the second closest ion (PW_{2c})	Lattice		Atomic mass (m_F)	Framework anion	
Total path width (PW)	Lattice		Electronegativity (EN_F)	Framework anion	
Phonon frequency (ω_{LEO})	Lattice		Ion polarizability (α_F)	Framework anion	
Bulk modulus (B)	Mechanical		Bader charge (BC_F)	Framework anion	
Band gap (E_g)	Electronic		Born effective charge (BEC_F)	Framework anion	
Electronic dielectric constant (ε_e)	Electronic		Ionicity between cation and chalcogen anion ($I_{C\text{-}Ch}$)	Chemical	
Ionic dielectric constant (ε_i)	Electronic		Ionicity between cation and halogen anion ($I_{C\text{-}H}$)	Chemical	
Total dielectric constant (ε)	Electronic	ε_i	Ionicity between anions ($I_{Ch\text{-}H}$)	Chemical	
Polarizability ($\bar{\alpha}$)	Electronic		Decomposition energy (E_d)	Chemical	
			Defect formation energy (E_f)	Chemical	

Descriptors. We collected 45 descriptors that may describe the ion mobility as listed in Table 5.1. Descriptors can be categorized by 'lattice', 'mechanical', 'electronic', 'chemical', or 'compound species' properties. The descriptors were collected based on DFT calculations in Chapter 4; available properties were adopted directly from the previous study, otherwise predicted low-energy structures of APs were used to obtain descriptors with methods discussed in the following paragraphs.

The properties of species (i.e., cation, octahedral anion, or framework anion) include ionic radius,[187] atomic mass,[265] Pauling electronegativity,[266,267] polarizability, Bader charge, and Born effective charge. The Bader charge, which identifies individual atoms and estimates its actual net charge, was predicted using the *Bader Charge Analysis* code with previous DFT electron density

calculations.[211–214] Since two cation sites involve in a path (i.e., end points of a path), the Bader charge and the Born effective charge of a sample (i.e., each elementary path) were estimated by averaging the values of two cations involved. The Bader and Born effective charges of octahedral and framework anions were evaluated by averaging the values of the same anions in a unit cell.

The packing fraction (PF), which represents the ratio of an occupied volume to the total volume, was obtained by the iterative method.[39] The packing fraction without cation (PF_C) measures the occupied volume only by anions. The tolerance factor, which measures the degree of lattice distortions of (anti)perovskite structure,[160] is calculated by $t = (R_X + R_B)/\left[\sqrt{2}(R_X + R_A)\right]$, where R_X, R_B, and R_A are the atomic radii of cation (X site), anion at the octahedron center (A site), and anion at the cubic framework (B site). The lattice structure tends to be cubic when $t \sim 1$, but it becomes orthorhombic as the degree of lattice distortion increases with smaller t (usually when $t < 0.83$). The channel size (i.e., the largest diameter of sphere that can pass freely through the anion sublattice) was claimed to be an important factor for ion mobility within a series of LGPS family.[46] It was calculated by the *Zeo++* code.[268] The coordination number of cation was calculated by counting the number of neighbor ions which have the distance to the cation shorter than 1.2 times of the sum of their ionic radii. The coordination numbers of two cations were averaged since two cation sites involve in a path (the same as for the Bader charge).

Distance-based descriptors were discussed in a previous ML study, but their importance may vary.[39] We included the distances between cations (CCD, i.e., linear path distance), between cation and octahedral/framework anions (COD/CFD, respectively), and between anions (AAD). COD and CFD were evaluated by finding the closest anion for each cation and the distance between them, and then averaging the distances of two cations involved in the path (the same as for the Bader charge). AAD was obtained by finding the closest neighbor anion for each anion and the distance between them, and then averaging the distances over all anions. The path width was evaluated by identifying ions close to the path and measuring the perpendicular distance from the path to the surface of ion (see Ref.[39] for the detailed explanation). We listed three path widths, including the path width by the closest ion (PW_c), the path width by the second-closest ion (PW_{2c}), and the total path width (PW) by the sum of PW_c and PW_{2c}. The lattice dynamics (i.e., phonon frequencies) are also shown to be of importance for ion mobility in literature.[42,43,206] We employed

the frequency of lowest-energy optical phonon (ω_{LEO}) to account for the effect of lattice dynamics.[42]

The total dielectric constant (ε) was obtained by the sum of electronic (ε_e) and ionic (ε_i) contributions. A compound with a high polarizability would have a high ion mobility due to the lattice softening effect.[44] The polarizability of compound was calculated by the Clausius-Mossotti relation as[207]

$$\bar{\alpha} = \frac{3}{4\pi}\left(\frac{\varepsilon_e - 1}{\varepsilon_e + 2}\right) v_{\mathrm{atom}}, \tag{5.3}$$

where v_{atom} is the lattice volume per atom. The bond ionicities between cation and chalcogen anion ($I_{\mathrm{C\text{-}Ch}}$), between cation and halogen anion ($I_{\mathrm{C\text{-}H}}$), and between chalcogen and halogen anions ($I_{\mathrm{Ch\text{-}H}}$) were calculated by the difference in electronegativities between species.[39] The energy above the convex hull (i.e., decomposition energy) was added in the list to include an aspect that most of superionic conductors are not stable at zero Kelvin.[48] The formation energies of neutral vacancy and interstitial dumbbell are calculated by[269]

$$E_{\mathrm{f}} = E_{\mathrm{AP\_defect}} - \left(E_{\mathrm{AP\_pristine}} + \sum_i n_i \mu_i\right), \tag{5.4}$$

where $E_{\mathrm{AP\_defect}}$ and $E_{\mathrm{AP\_pristine}}$ are the total energies of the AP supercell with and without a cation defect, i is the defect species (Li, Na, or K), and n_i and μ_i are the number of the defect cation (-1 for vacancy and +1 for interstitial dumbbell) and its chemical potential. The defect formation energy for a certain elementary path is assigned by averaging the formation energies of two defects involved in the path (i.e., defects at end points of the path).

5.3.2 Implementation of Machine Learning

Feature filtering. Figure 5.2 shows the Pearson correlation analysis for the vacancy mechanism. There is no individual feature that shows a high linear correlation with the elementary barrier (at most 0.34 of the path distance, CCD). It confirms that a single feature cannot represent ion migration in solids. ML analysis can help to find complicated correlations between many features and elementary barriers. This conclusion is the same for the interstitial dumbbell mechanism (at most 0.14 of the phonon frequency, ω_{LEO}).

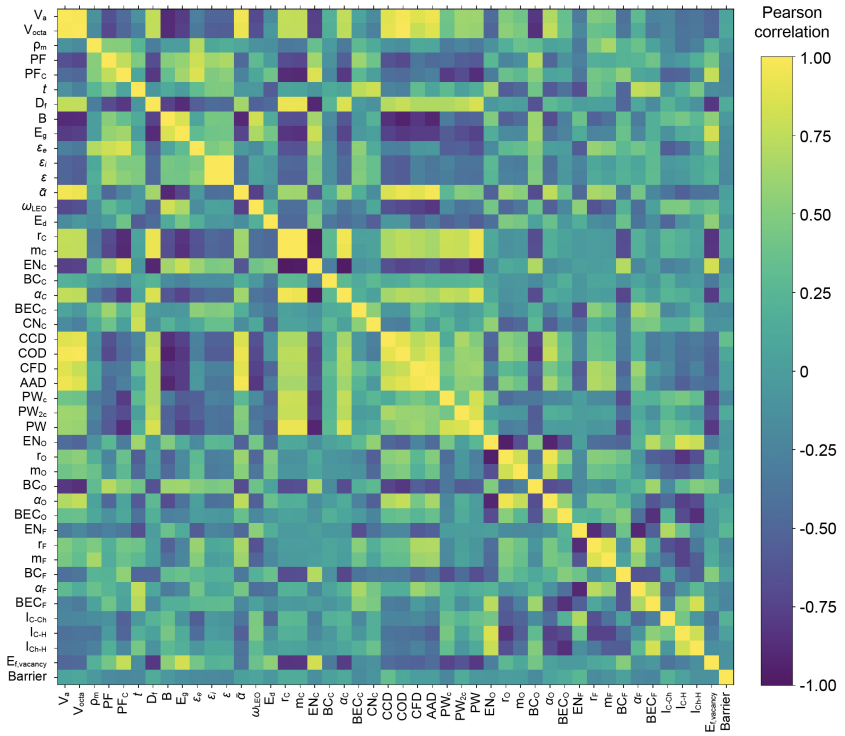

Figure 5.2 Pearson correlation analysis among descriptors and vacancy elementary barriers. +1/-1 value indicates perfect positive/negative linear correlation, whereas no correlation is expected when the coefficient is close to 0.

Seven features were reduced based on the analysis (Table 5.1). The octahedron volume (V_{octa}) is highly correlated to the cell volume (V_a) with ρ = 0.98, indicating that one of these volumetric features is redundant. Thus, V_{octa} was reduced since V_a is more general than V_{octa}. The total dielectric constant (ε) is strongly correlated to the ionic dielectric constant (ε_i) with ρ = 0.99, since the ionic contribution to the total dielectric constant is usually much larger than the electronic contribution (ε_e). So, ε was reduced to ε_i because ε contains ε_e, whereas ε_i has an independent meaning from ε_e. The electronegativity of cation (EN_C) has high correlations to ionic radius (r_C), atomic mass (m_C), and polarizability (α_C) of cation with $\rho \leq$ -0.98 because they can be classified by the type of species. Thus, r_C, m_C, and α_C were reduced to EN_C. Also, the ionic radius of octahedral anion (r_O) has high correlations to electronegativity (EN_O), and polarizability (α_O) of octahedral anion with $|\rho| \geq 0.94$, so EN_O and α_O were reduced to r_O. The filtering implies that reduced features are also important if a reducing feature is proved to be influential in the target property. The correlation analysis result for the interstitial dumbbell is similar to the vacancy result, thus we used the same features for the dumbbell mechanism.

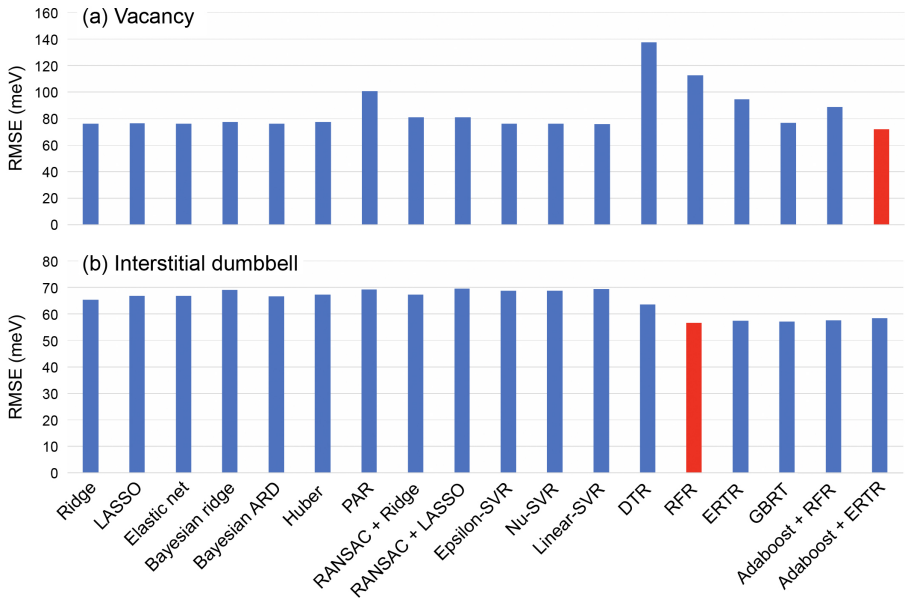

Figure 5.3 Comparison between ML models optimized with 38 features after filtering: (a) vacancy and (b) interstitial dumbbell mechanisms. The test set is used to obtain RMSEs. A red bar indicates the best model.

Model selection. Figure 5.3 compares the performance between ML models with different algorithms, optimized with 38 features after filtering. The 'adaboost + ERTR' algorithm shows the best predictability for vacancy barriers with 72 meV root mean squared error (RMSE). RFR performs the best for dumbbell barriers (58 meV RMSE), but it shows a bad prediction for vacancy barriers (113 meV RMSE, more than 1.5 times larger than 'adaboost + ERTR'). Also, all the tree-based algorithms except DTR show similar prediction powers for dumbbell barriers; the largest difference between RMSEs of these five models is less than 1.6 meV. Therefore, we selected the 'adaboost + ERTR' algorithm to evaluate feature subsets for both vacancy and dumbbell mechanisms.

Figure 5.4 presents the training and test results for vacancy and dumbbell barriers with the 'adaboost + ERTR' algorithm. Figures 5.4(a) and 5.4(b) show that the ML models perfectly predict DFT calculations of the training set for vacancy and dumbbell, indicating that the learning process was performed appropriately. Most of data points in Figures 5.4(c) are well aligned on the guide line, implying a good predictability of the ML model for vacancy (72 meV RMSE). A large portion of the error comes from 5 data points with barriers larger than 550 meV; 64% of the sum of squared error (SSE) is originated from these 5 samples (among 64 test samples). This is because of a relatively small number of training data with very large barriers over 550 meV [4.4% of the

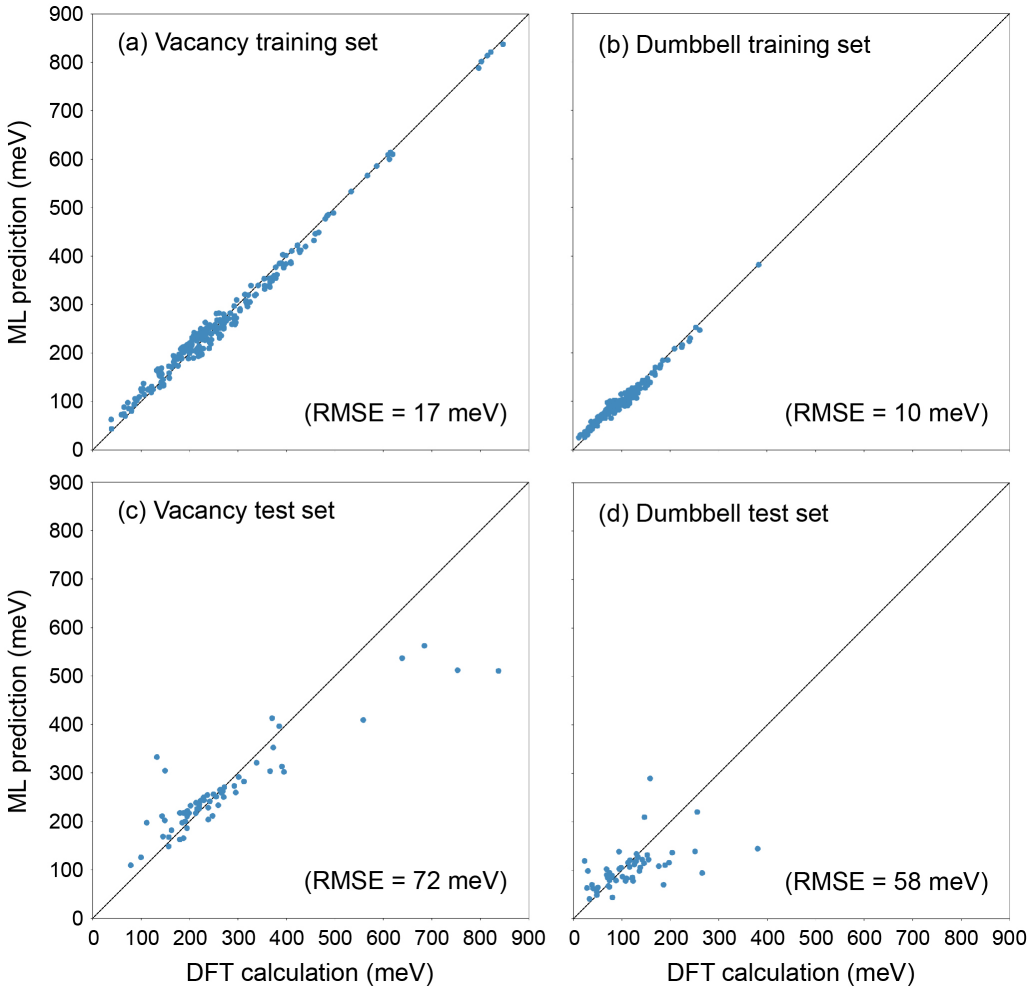

Figure 5.4 Training results of the 'adaboost + ERTR' model with 38 features after filtering using the training data set of (a) vacancy and (b) dumbbell mechanisms. The performance of the model is presented by predicting the test data set of (c) vacancy and (d) dumbbell mechanisms. The black line is a guideline for the perfect prediction.

training set, Figure 5.4(a)]. The ML model for dumbbell also shows a reasonable predictability, Figure 5.4(d). As the same to vacancy, a large portion of RMSE (58 meV) comes from 12 data points with barriers larger than 150 meV; 79% of SSE is originated from these 12 samples (among 56 test samples). Only 10.0% of the training data have barriers over 150 meV, Figure 5.4(b).

Feature subset evaluation. Figure 5.5 presents the effect of the number of features on the predictability of the ML model. The result with the vacancy barriers shows that RMSE reduces and converges as increasing the number of features from 1 to 8 features. However, RMSE with 33 features is higher than that with 8 features and the error increases with a greater number of features over 33 (like a U-shape). We believe that RMSE will not show a meaningful decrease as increasing

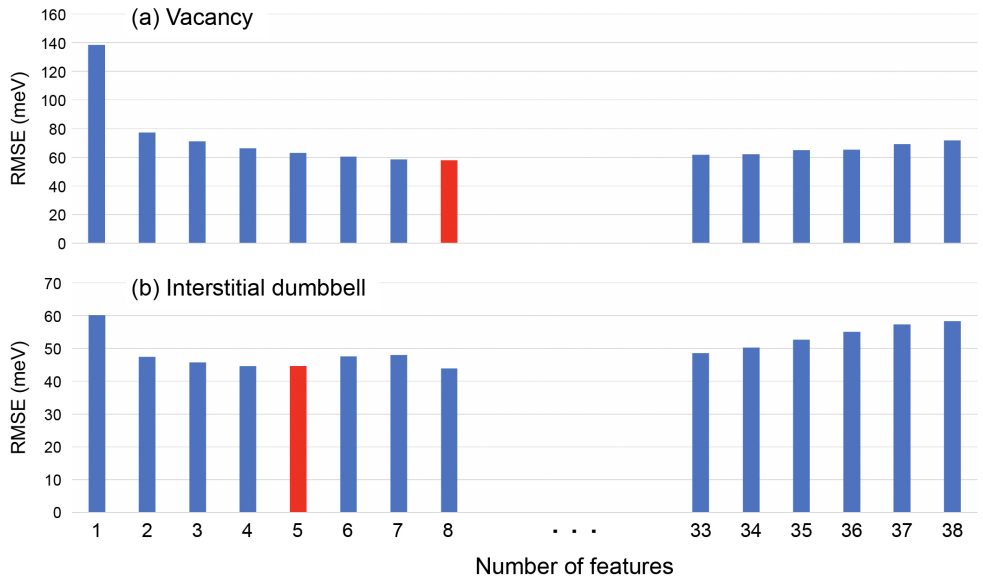

Figure 5.5 Comparison between the 'adaboost + ERTR' models with different numbers of features: (a) vacancy and (b) interstitial dumbbell mechanisms. Each bar represents the lowest RMSE with a certain number of features. The red bar indicates the optimal number of features.

the number of features more than 8. The same trend is also observed in dumbbell barriers, and RMSE fluctuates when the number of features exceeds 5. Although not severe in our results, this U-shape is a well-known overfitting trend.[243] It implies that the predictability of a model becomes maximized with an optimal number of features. Therefore, the 8-feature subset for vacancy and the 5-feature subset for dumbbell are the optimal choices for the predictability as well as a computational efficiency. (Features in these subsets will be discussed in the next section.)

Comparing to Figure 5.4(c) with the full number of features (72 meV RMSE), Figure 5.6(a) with the optimal features subset of vacancy shows that the test samples distribute more closely to the guideline with lower RMSE of 58 meV. This is the same for dumbbell with the optimal feature subset that RMSE reduces from 58 [Figure 5.4(d)] to 45 meV [Figure 5.6(b)]. This result verifies that the optimal feature subset predicts and describes ion migrations through elementary paths better than subsets with larger or smaller number of features.

5.3.3 Interpretation of Results

Features for vacancy migration. Figure 5.7 presents the most predictive features (i.e., selected feature subset) and relative importance of features (in percentage) for ion migration. Figure 5.7(a) suggests that lattice properties have the strongest impact to the vacancy migration,

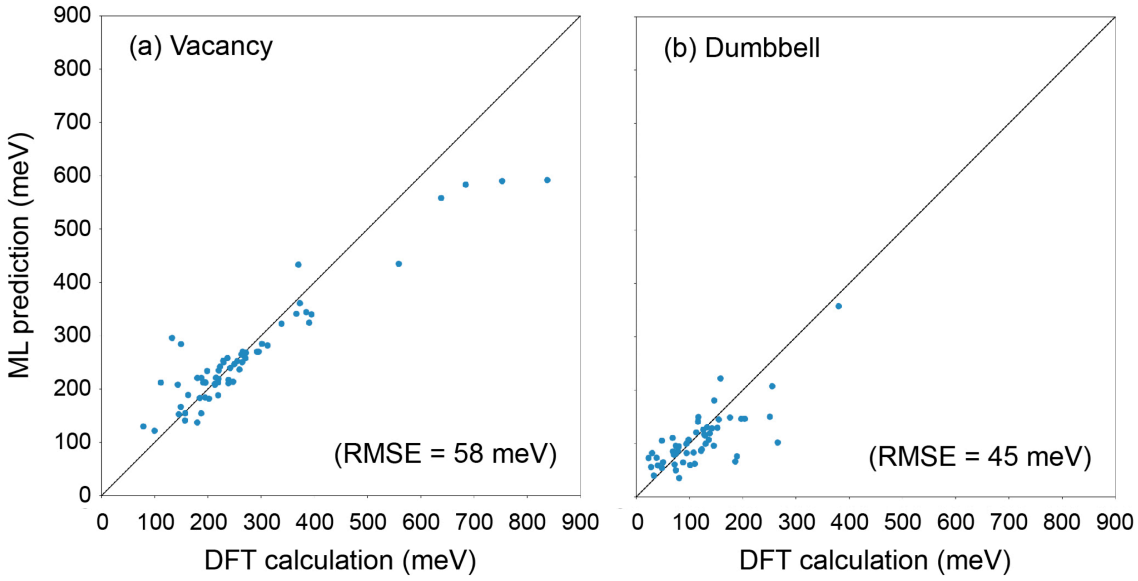

Figure 5.6 Performance of the 'adaboost + ERTR' model by predicting the test data set with the best feature set: (a) vacancy (8-feature subset) and (b) dumbbell (5-feature subset) mechanisms. The black line is a guideline for the perfect prediction.

occupying 78% of the total importance. Especially, the path distance and path widths are the most important features describing the vacancy migration. Figure 5.8 shows the ICE plots for the top three features for vacancy (other features do not show clear ICE trends).

The path distance (CCD) has the largest importance of 29%, and its ICE plot shows that the elementary barrier of vacancy increases with a greater CCD [Figure 5.8(a)]. A longer CCD means that the transition state on a migration path is farther from a local minimum on the potential energy surface (PES; i.e., an equilibrium site of mobile ion), which increases the energy barrier. Therefore, a short migration path is favorable to increase ion mobility. The increase in the energy barrier along the center line of the ICE plot (from left to the right end) is over 300 meV, which is twice the increase in the barrier owing to the path widths [Figures 5.8(b) and 5.8(c)]. It shows the largest impact of the CCD on the barrier comparing to other features, agreeing with the largest importance among features. Therefore, the most effective scheme in the lattice design is to decrease the distance between cation sites. This result is analogous to a previous ML study that the average of distances between mobile ions is an effective feature to classify superionic conductors.[39]

The path width by the first closest ion (PW_c; 23%) and the total path width (PW; 17%) appear to be the second and the third important features, respectively. The ICE plots show that the

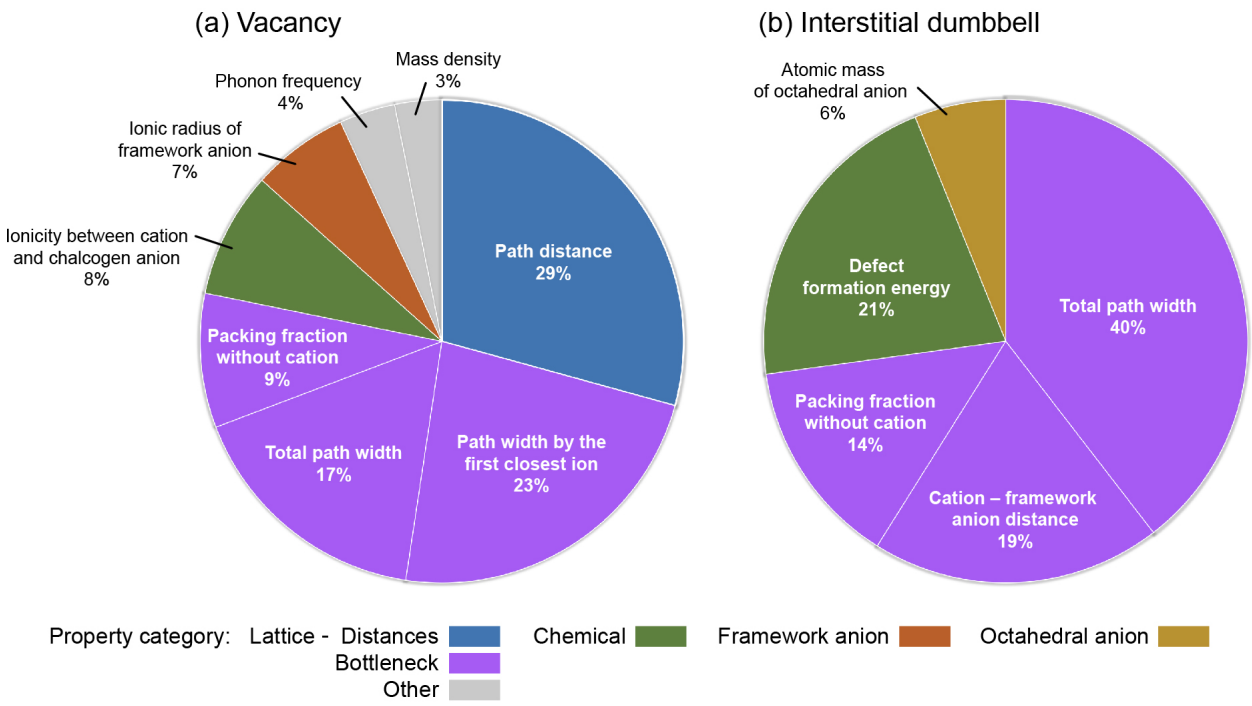

Figure 5.7 Most predictive features and their relative importance (in percentage): (a) vacancy and (b) interstitial dumbbell mechanisms. The importance was evaluated by the mean decrease impurity method.

energy barrier of elementary path decreases with wider path widths [Figures 5.8(b) and 5.8(c)]. It suggests that a lattice needs to have a wide migration window for a high ion mobility, thus framework species should be far from migration paths. This result supports our previous analysis that wide migration channels suppress the corrugation of PES and decrease barriers.[208] The barrier does not change with PW_c when PW_c is too small, in the left area of Figure 5.8(b). The PW_c value in this area is negative, indicating that the linear migration path is interfered by the closest ion. It may imply the channel-widening will be effective when the interference becomes less than 0.2 Å. Also, the decrease in the barrier is negligible when PW_c becomes too wide [in the right area of Figure 5.8(b)], thus the optimized PW_c will be about 0.6 Å. It is also possible that PW might have the optimized value when it becomes wider than the upper bound in Figure 5.8(c).

The Pearson linear correlation between PW_c and PW is high, $\rho = 0.83$; this is reasonable because PW includes PW_c. The packing fraction without cation (PF_C) is ranked at the fourth place with a 9% importance, and has a high correlation to PW with $\rho = -0.87$. Therefore, the elementary barrier will decrease with smaller PF_C (i.e., barrier $\propto 1/PW \propto PF_C$). Although not shown in the best feature subset of vacancy, PW_{2c} and D_i could also be considered as meaningful factors for

vacancy since they indicate the free space for mobile cations to move in a lattice structure. They have high linear correlations to PW with ρ = 0.86 and 0.85, respectively, implying that the elementary barrier will decrease with larger PW_{2c} and D_i. These features (PW, PW_c, PW_{2c}, PF_C, and D_i) can be combined into one descriptor (e.g., PW) by the feature filtering with a moderate

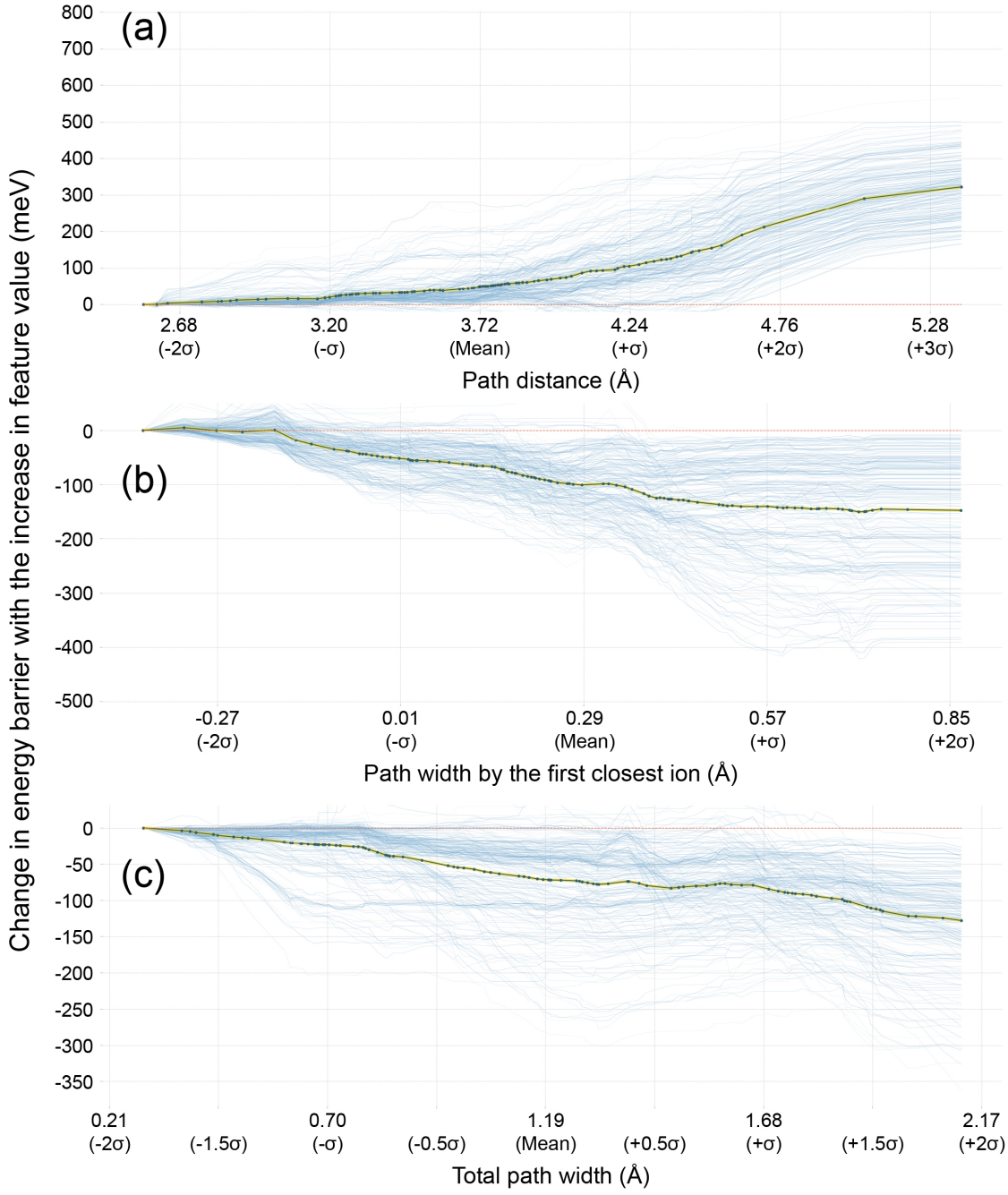

Figure 5.8 ICE plots of top three features for vacancy: (a) path distance, (b) path width by the first closest ion, and (c) total path width. The center curve (yellow) shows the trend of migration barrier with the increase in the feature (i.e., from left to the right). Mean and standard deviation (σ) of features are denoted in parentheses in x-axis.

threshold (e.g., $|\rho| \geq 0.80$), which will be a sole feature that represents the bottleneck area for the vacancy migration.

There are additional four features that have minor effects on vacancy. The ionicity between cation and chalcogen anion ($I_{C\text{-}Ch}$) has an 8% importance. A weak ionicity reduces net charges of ions due to the covalency effect and mitigates the electrostatic attraction between cations and chalcogen anions.[222,270] Thus, cations will migrate through paths more easily. This interpretation agrees with a previous ML study that a weak ionicity of pathway can help breaking and reforming of cation bonds with low energies.[39] The ionic radius of framework (r_F) shows a 7% importance. We presume that this feature indicates the effect of halogen anion based on literature that larger halogen anion can reduce energy barriers and increase ionic conductivities, especially due to the polarizability.[44,271–275] (r_F correlates to the polarizability α_F with a non-negligible coefficient, ρ = 0.72.) Phonon frequency (ω_{LEO}) and mass density (ρ_m) have very weak influence on elementary barriers (4 and 3% importance, respectively).

From these lessons learnt, we tested a simplified ML model by using 20 features filtered with $|\rho| \geq 0.80$ and the 'adaboost + ERTR' algorithm. The best feature subset of the simplified model presents CCD (42%), PW (28%), and r_F (11%) as top 3 features occupying 80% of the total importance. (This best subset has 7 features, and other 4 features have contributions equal to or less than 6% each.) By the feature filtering, CCD includes distance-based features (COD, AAD, and CFD) and PW including PW_c, PW_{2c}, PF_C, PF, and D_i represents the bottleneck area as discussed. Therefore, this result further supports our analysis that lattice properties, especially distances between species and bottleneck area, are the most influential in the vacancy mobility.

Features for interstitial dumbbell migration. Figure 5.7(b) suggests that lattice properties also have the strongest impact to the interstitial dumbbell migration: PW, cation – framework anion distance (CFD), and PF_C occupy 73% of the total importance. The defect formation energy (E_f) accounts for a 21% importance and ranks at the second place. Note that features of dumbbell do not show clear ICE trends.

PW and PF_C, shown in the best feature set of vacancy, also appear as important features for interstitial dumbbell. PW is the most important feature with a 40% importance, which is the same degree of importance as for the path widths (PW_c and PW) of vacancy, and PF_C is ranked at the fourth place with a 14% importance. As shown in the vacancy case, wider PW and lower PF_C

will reduce the elementary barriers of dumbbell. CFD occupies 19% of the total importance (third rank) and has linear correlations to PW and D_i with Pearson coefficients ρ = 0.64 and 0.73, respectively. It implies that CFD is related to the bottleneck area for the dumbbell migration. Thus, we believe that longer distance between cation and framework anion will make wider space and reduce the elementary barrier of interstitial dumbbell.

The path distance (CCD), shown as the most important feature for vacancy, does not appear as an important feature to describe the dumbbell migration. This may be because the concerted motion of three cations associated with the dumbbell migration makes an effective migration distance much shorter than the linear distance between cation sites.[66] Thus, the migration distance is not significant to describe the energy barrier of interstitial dumbbell.

The energetic stability of equilibrium and transition states (ES and TS, respectively) affect to the energy barrier ($E_b = E_{TS} - E_{ES}$), see Chapter 4. Higher E_f indicates that the ES of dumbbell is less stable (i.e., higher E_{ES}). Also, a previous study showed with vacancies in Li_3OCl AP that TSs do not change much with a large change in the stability of defect.[71] Thus, we presume that E_{TS} of dumbbell is not affected by the change in E_{ES}. Therefore, the elementary barrier of dumbbell might decrease with the increase in E_f. The atomic mass of octahedral anion (m_O) has a very weak influence on elementary barriers (6% importance).

In total, ML analysis revealed that lattice properties have the greatest influence in defect migrations. The path distance and bottleneck-related features appear as the most important features for vacancy, accounting for 78% of the total importance. For interstitial dumbbell, bottleneck-related features occupy a 73% importance, and the defect formation energy is also shown with a 21% importance. Regardless of migration mechanisms, therefore, tuning lattice structure will be the most effective scheme to improve ion mobility.

5.4 Conclusions

It is desirable to understand important features that describe a high ion mobility in solids for the systematic design of SEs. This study implemented a comprehensive ML analysis on elementary migration paths to systematically understand chemical, physical, and/or structural features that describe the ion transport through a lattice, their relative importance, and how they promote a high ion mobility. Previous DFT calculations were adopted to collect descriptors as well

as a large number of ion-migration data over 300 elementary barriers via vacancy and interstitial dumbbell mechanisms, based on 36 model APs X_3AB. The descriptors contain the information about migration environments of elementary paths as well as properties of compounds.

The ML process was performed in the order of the 'feature filtering', 'model selection', and 'feature subset evaluation'. The filtering reduced initially 45 descriptors to 38 features by eliminating reductant descriptors using a very high Pearson linear correlation of $|\rho| \geq 0.94$. The optimized ML model with the 'adaboost + ERTR' algorithm presents the best predictability for our data. The feature subsets with different numbers of features were evaluated using the best ML model. We found that the 8-feature subset for vacancy and the 5-feature subset for dumbbell are the optimal choices for the predictability, which reduce prediction errors than the full-feature models. Finally, the relative importance of these features and their influence in ion migration were analyzed by combining MDI, ICE plot, and Pearson linear correlation.

Our ML analysis revealed that lattice properties have the greatest influence in defect migrations regardless of mechanisms. The path distance and bottleneck-related features appeared as the most important features for vacancy, accounting for 78% of the total importance. The path distance (CCD) has the largest importance of 29%, and three bottleneck-related features occupy a 49% importance (path width by the first closest ion, PW_c 23%; total path width, PW 17%; packing fraction without cation, PF_C 9%). Since bottleneck-related features are closely related, we also built a simplified ML model using a moderate filtering threshold ($|\rho| \geq 0.80$) that leads to 20 features for the optimization of the ML algorithm. This model again showed that CCD (42%) and PW (28%) appear as top 2 features, which further supports our analysis that lattice properties are the most influential in the vacancy migration. The elementary migration barrier decreases with a shorter path distance and wider bottleneck for migration, thus decreasing the distance between mobile cations and keeping framework ions away from paths will be helpful for the lattice design with a high vacancy mobility. For interstitial dumbbell, bottleneck-related features occupy a 73% importance (PW 40%; cation – framework anion distance, CFD 19%; PF_C 14%). PW and PF_C, shown as important features for vacancy, also appeared in the feature subset of dumbbell.

In total, this stochastic study gives a thorough analysis of ion migration with comprehensive features including detail environments of elementary paths as well as compound properties, and will aid in the systematic design of solid electrolytes for solid-state batteries.

Chapter 6 Potential Solid Electrolytes for Multivalent Ions Based on the Anti-perovskite Structure

6.1 Introduction

Thus far, many inorganic solids with high Li-ion conductivities at room temperature (R.T.) have been suggested as SEs, including $Li_{2.9}PO_{3.3}N_{0.46}$,[23] $75Li_2S•25P_2S_5$ (LPS glass),[24] $Li_7La_3Zr_2O_{12}$,[19] Li_6PS_5Br,[20] $Li_{10}GeP_2S_{12}$,[21] and $Li_{9.54}Si_{1.74}P_{1.44}S_{11.7}Cl_{0.3}$..[22] These findings open the possibility to realize SSBs using a Li-metal anode. Also, there are various Na and K-ion conductors like Na_3PS_4 (glass-ceramic),[28] $Na_{10}SnP_2S_{12}$,[29] $Na_{11}Sn_2PS_{12}$,[30] $NaCB_{11}H_{12}$,[32] K-β"-Al_2O_3 (beta-alumina; also conducting Na, Ag, Li, and Rb ions),[276,277] and $K_2Fe_4O_7$.[278] In contrast, a limited number of fast MV-ion conductors at R.T. has been reported. Metal-organic frameworks (MOFs) were shown as host materials for solid Mg conductors.[279] Authors inserted $Mg(OPhCF_3)_2$ and $Mg(TFSI)_2$ salts into Mg_2(dobdc) and Mg_2(dobpdc) MOFs and presented Mg-ion conductivities up to 10^{-4} S/cm at R.T. (activation energy E_a = 110 ~ 190 meV). A chalcogenide spinel $MgSc_2Se_4$ presents a high Mg-ion conductivity of ~10^{-5} S/cm at R.T. (E_a = 370 meV), which was the first demonstration of fast Mg-ion conduction in a close-packed framework.[40] In addition, solid polymer electrolytes were suggested as Ca-ion conductors, e.g., a solid network by cross-linking between PTHF and Epoxy and containing $Ca(NO_3)_2$ with ionic conductivities up to 10^{-4} S/cm at R.T. (E_a = 310 meV; transference number = 0.359).[280,281] Therefore, the discovery of MV SEs remains an important pursuit to advance the prospects for MV SSBs.

Previous literature showed that most alkaline earth metals, 3d transition metals, and lanthanides can reside in the AP lattice cage.[282,283,292–296,284–291] These AP materials have small anions B, C, N, or O at the center of octahedra (A site) to maintain high tolerance factors, and a number of anions can occupy the B site. They exhibit a wide range of electronic, magnetic, and thermal properties, and have been exploited in applications ranging from thermoelectrics, memory devices, sensors, and optical devices.[283,284] Here, we focus on Mg and Ca-containing AP to

investigate the possibility to use them as SEs of MV SSEs. Mg^{2+} and Ca^{2+} cations can occupy the X site of the AP structure (i.e., at vertices of X_6A octahedra), then A^{3-} and B^{3-} pnictogen anions (elements in Group 15) form the bcc framework and make the charge balance in the X_3AB formula. Among many possible combinations, we selected ten Mg/Ca APs not presenting a metallic behavior: Mg_3NB, Ca_3NB, Ca_3PSb, and Ca_3AsSb (where B = P, As, Sb, or Bi).[293–296]

First-principles calculations were used to evaluate suitability for SE applications by predicting equilibrium structures, band gaps, elastic moduli, percolating migration barriers, defect formation energies, thermodynamic stability, and chemical stability window under applied potential. All compounds are predicted to be thermodynamically stable, which agrees to the fact that six of them have been synthesized. Thus, it is expected that not-yet-synthesized compounds Mg_3NP, Mg_3NBi, Ca_3PSb, and Ca_3AsSb are also synthesizable. Ca and Mg APs follow a similar trend to that observed in monovalent APs, where lattice distortions decrease the energy barriers for percolating ion migration. These MV APs are predicted to have high defect formation energies, implying that defect concentrations need to be frozen in during synthesis.

We found that Mg_3NAs, Ca_3NAs, and Ca_3PSb are potential candidates of SEs for MV SSBs. Mg_3NAs and Ca_3NAs have low percolating barriers of about 500 meV for vacancy and less than 200 meV for interstitial dumbbell migration mechanisms. Ca_3NAs was shown as an electronic insulator,[293] and Mg_3NAs having much larger band gap than Ca_3NAs would also have an insulating behavior. Ca_3PSb has even lower vacancy limiting barrier 433 meV with the same band gap as Ca_3NAs, which come at a cost to diminished chemical stability window. These compounds are stable against the respective metal anode and predicted to have moderate oxidative stability up to 1.2, 1.7, and 1.4 V, respectively, implying that coating materials may be needed to prevent oxidation by the cathode and increase the operating voltage. In total, this work will aid in the advance of Mg and Ca MV SSBs with metal anodes.

6.2 Methodology

6.2.1 First-principles Calculations

DFT calculations were implemented with the Vienna *ab initio* Simulation Package (VASP).[134] The Perdew-Burke-Ernzerhof (PBE)[110] exchange-correlation functional was used in

combination with the projector augmented wave (PAW) method.[135,136] The valence electron configurations were: $2s^2 2p^6 3s^2$ for Mg, $3s^2 3p^6 4s^2$ for Ca, $2s^2 2p^3$ for N, $3s^2 3p^3$ for P, $4s^2 4p^3$ for As, $4d^{10} 5s^2 5p^3$ for Sb, and $5d^{10} 6s^2 6p^3$ for Bi. The plane-wave basis included functions with kinetic energies equal or higher than 550 eV for Mg compounds and 450 eV for Ca compounds. This cutoff energy is set to 520 eV for all compounds during calculations for phase diagram and chemical stability, the same to the Materials Project database. The Brillouin zone was sampled on an 8 × 8 × 8 grid for Mg APs with a cubic lattice (5 atoms), a 6 × 6 × 6 grid for Ca APs with a cubic lattice (5 atoms), and a 3 × 3 × 3 grid for all APs with an orthorhombic lattice (20 atoms), a 21 × 21 × 13 grid for Mg metal (2 atoms), a 2 × 2 × 2 grid for Mg_3Z_2 (Z = N, P, or As; 80 atoms), a 8 × 8 × 6 grid for Mg_3M_2 (M = Sb or Bi; 5 atoms), a 8 × 8 × 8 grid for Ca metal (4 atoms), a 8 × 8 × 2 grid for Ca_2N (9 atoms), a 6 × 6 × 6 grid for CaZ (Z = P or As; 12 atoms), and a 6 × 6 × 2 grid for Ca_2M (M = Sb or Bi; 12 atoms). A Γ-centered k-point mesh was used. These cutoff energies and k-point sampling densities yielded energy convergence to within 2 meV/atom. The energy criterion for convergence of the self-consistency loop was set to 10^{-5} eV, and the force criterion for the relaxation of geometric degrees of freedom (ion positions and cell geometry) was 0.01 eV/Å. The equilibrium volume was found by fitting energy data as a function of volume to the Murnaghan EOS.[132] The non-self-consistent GW (G_0W_0) method with the HSE06[112,113] hybrid functional was used to calculate band gaps, which works well in a practical manner.[116,117,121]

The energy barrier of ion migration was evaluated by the nudged elastic band (NEB) method.[168,169] NEB calculations were performed on enlarged supercells based on a 3 × 3 × 3 replication (135 atoms) of the unit cell for cubic (Pm-3m) compounds and a 2 × 2 × 2 replication (160 atoms) for orthorhombic (Pnma) compounds. The Brillouin zone was sampled on a 2 × 2 × 2 grid for a cubic supercell and a 2 × 2 × 1 grid for an orthorhombic supercell, with a Γ-centered k-point mesh. These k-point sampling densities yielded energy convergence for supercells to within 1 meV/atom. The force convergence criterion for NEB calculations was set to 0.04 eV/Å with three intermediate images.

Bulk and shear moduli were calculated by the Voigt equations using the stiffness tensor C_{ij}.[178] We found that the predicted bulk moduli by the Voigt formula are almost the same to the values obtained by the Murnaghan EOS fitting (see Table 6.2). The finite differences were used for the stiffness tensor calculation to include the ionic contribution as well as cell distortions, as implemented in VASP. Finer DFT settings were used to predict accurate elastic properties: (1) The

cutoff energies are increased to 800 eV for Mg_3NB (B = P, As, Sb, or Bi), 700 eV for Ca_3NB (B = P, As, Sb, or Bi), and 600 eV for Ca_3PSb and Ca_3AsSb, (2) the Brillouin zone was sampled on an 11 × 11 × 11 grid for Mg APs with a cubic lattice (5 atoms), a 8 × 8 × 8 grid for Ca APs with a cubic lattice, and a 4 × 4 × 4 grid for all compounds with an orthorhombic lattice, with a Γ-centered k-point mesh, (3) the energy criterion for convergence of the self-consistency loop was set to 10^{-7} eV, and (4) an additional support grid for the evaluation of the augmentation charges was used (*ADDGRID* tag in VASP).

6.2.2 Defect Formation Energy

The formation energy of defect *X* is calculated by[69,71]

$$E_f(X) = E_S(X) - [E_S(\text{Defect-free}) \pm E_X], \tag{6.1}$$

where $E_S(X)$ and $E_S(\text{Defect-free})$ are the energies of the defective and pristine supercells and E_X is the energy of a formula unit (f.u.) *X* added $(+)$ to or extracted $(-)$ from the supercell. The formation energy is per defect pair. The size of supercell is the same as for NEB calculations.

6.2.3 Thermodynamic Stability

The phase diagram and chemical stability window of APs (i.e., stable potential range with respect to a metal anode) were analyzed by the Materials Project database and *pymatgen* code.[37,133,172,173] The phase diagram was constructed by comparing zero Kelvin DFT energies of compounds.[172] The chemical stability window is the potential range where reductive nor oxidative reaction does not occur in a contact with a metal.[36] A compound is stable with a metal anode if no reaction occurs at 0 V, and the oxidation limit is the highest viable voltage without additional treatments. The chemical stability window was analyzed by following the method using the grand potential phase diagram.[133] The decomposition energy of a given phase into the phase equilibria in a contact with a Mg or Ca metal reservoir at an applied voltage ϕ (at zero Kelvin without vibrational contributions and the pV term)[133] can be expressed as[36]

$$E_{D,\text{open}}(\phi) = \{E_{\text{Equilibrium}}(\phi) - [E_{AP} + \Delta n_M \mu_M(\phi)]\}/N, \tag{6.2}$$

where *N* is the total number of atoms involved in the balanced equation, $E_{\text{Equilibrium}}(\phi)$ is the sum of total energies of all phases at the equilibrium, E_{AP} is the total energy of AP, Δn_M is the change

in the number of atom M = Mg or Ca metal (reduction/oxidation when Δn_{M} is positive/negative), and $\mu_{\mathrm{M}}(\phi)$ is the chemical potential of M under an external potential described as[36]

$$\mu_{\mathrm{M}}(\phi) = \mu_{\mathrm{M}}^{0} - ze\phi, \tag{6.3}$$

where μ_{M}^{0} is the chemical potential of M without an external potential, z is the charge number of M (+2 for alkaline earth metals), and e is the elementary charge.

6.3 Results and Discussion

6.3.1 Structure

Four Mg and six Ca APs will be considered: Mg_3NB, Ca_3NB, Ca_3PSb, and Ca_3AsSb (where B = P, As, Sb, or Bi).[293–296] First, we predicted ground-state structures of compounds whose experimental data are available; i.e., Mg_3NB (B = As or Sb)[294] and Ca_3NB (B = P, As, Sb, or Bi).[293,297] The atomic configuration of Ca_3NAs was used an initial guess of the orthorhombic structure of Ca_3NP since only the lattice parameter of Ca_3NP is known. Other four compounds have the cubic symmetry. The tolerance factor and predicted lattice parameters are listed in Table 6.1. (Ionic radii of elements were cited from ref.[298], and the ionic radius of Bi^{3-} anion was assumed as 2.48 Å based on the bond lengths of Mg pnictogenides.) The predicted structures are very close to experiments. Especially, the octahedron tilting angle of Ca_3NAs is nearly the same to the experiment (8.7°).[297] The predicted tilting angle of Ca_3NP is 12.7°, larger than that of Ca_3NAs due to its smaller tolerance factor (i.e., greater lattice distortion).

Table 6.1 Tolerance factor (*t*), structure symmetry, and lattice parameters of Mg and Ca APs. Values in parentheses are experiment data.[293,294]

Compound	*t*	Symmetry	*a* (Å)	*b* (Å)	*c* (Å)
Mg_3NP	0.823	Orthorhombic	5.936	5.929	8.382
Mg_3NAs	0.851	Cubic	4.242 (4.217)		
Mg_3NSb	0.916	Cubic	4.378 (4.352)		
Mg_3NBi	0.925	Cubic	4.437		
Ca_3NP	0.812	Orthorhombic	6.742 (6.709)	6.627 (6.658)	9.433 (9.452)
Ca_3NAs	0.837	Orthorhombic	6.733 (6.725)	6.728 (6.720)	9.550 (9.534)
Ca_3NSb	0.896	Cubic	4.863 (4.854)		
Ca_3NBi	0.904	Cubic	4.908 (4.888)		
Ca_3PSb	0.780	Orthorhombic	7.434	7.813	10.599
Ca_3AsSb	0.757	Orthorhombic	7.526	7.983	10.711

Previous DFT studies simulated the rest of compounds Mg_3NB (B = P or Bi)[295] and Ca_3ASb (A = P or As)[296] using the cubic symmetry. However, the orthorhombic symmetry is a preferred structure for APs with lattice distortions (see Chapter 4), and the other DFT study showed that Mg_3NP can have an orthorhombic unit cell.[299] Therefore, we tested cubic and orthorhombic symmetries to determine the equilibrium structures by comparing ground-state energies between symmetries. The structure of Ca_3NAs was used as an initial guess of their orthorhombic structures. The result shows that Mg_3NBi has the cubic structure, which agrees with its highest tolerance factor among Mg APs in this study. Mg_3NP has an orthorhombic structure with a mild octahedra tilting (10.3°), which is 15.4 meV/atom more stable than the cubic phase (at zero Kelvin without zero-point energy). Ca_3ASb (A = P or As) also have orthorhombic structures with tilting angles (18.3° and 21.4°, respectively) larger than those of Mg_3NP and Ca_3NP due to smaller tolerance factors. The orthorhombic structures of Ca_3ASb (A = P or As) are more stable than cubic phases by 106.0 and 161.8 meV/atom, respectively.

Similar to cubic monovalent APs ($t > 0.83$), Mg and Ca APs with $t > 0.84$ have the non-distorted cubic AP symmetry. Otherwise, APs have orthorhombic structures with octahedra tilting, but no variation in the bond lengths/angles of octahedra was found (i.e., intact octahedron shape = moderate distortions). This also agrees with the criterion of moderate distortions for monovalent APs ($0.72 < t < 0.83$) that all Mg and Ca APs in this study have tolerance factors larger than 0.75.

6.3.2 Properties

Thermodynamic stability. The phase diagrams (Figure 6.1) show that all Mg and Ca APs are stable at zero Kelvin. It agrees with the fact that Mg_3NB (B = As or Sb) and Ca_3NB (B = P, As, Sb, or Bi) were already synthesized (Table 6.2).[293,294] Therefore, it is expected that other four not-yet-synthesized MV APs compounds are also synthesizable. Mg_3NB (B = P or Bi) may be synthesized by the synthesis method used for Mg_3NB (B = As or Sb), e.g., the reaction of pnictogen and Mg_3N_2 at 800 °C releasing 0.5 mol N_2 gas per mol.[294] Although Ca_3NB (B = P, As, Sb, or Bi) were also synthesized using pnictogen and Ca_3N_2 at 1000 °C,[293] Ca_3ASb (A = P or As) would need to be prepared using a different reaction path because As nor P will not be released in a form of gas. We presume that Ca_2Sb and CaZ (Z = P or As) may undergo a stoichiometric reaction without extra products based on the exothermic reaction energies at zero Kelvin: -126.1 and -109.9

meV/atom for Ca_3PSb and Ca_3AsSb, respectively. Note that all Mg and Ca APs will be sensitive to air.[293,294]

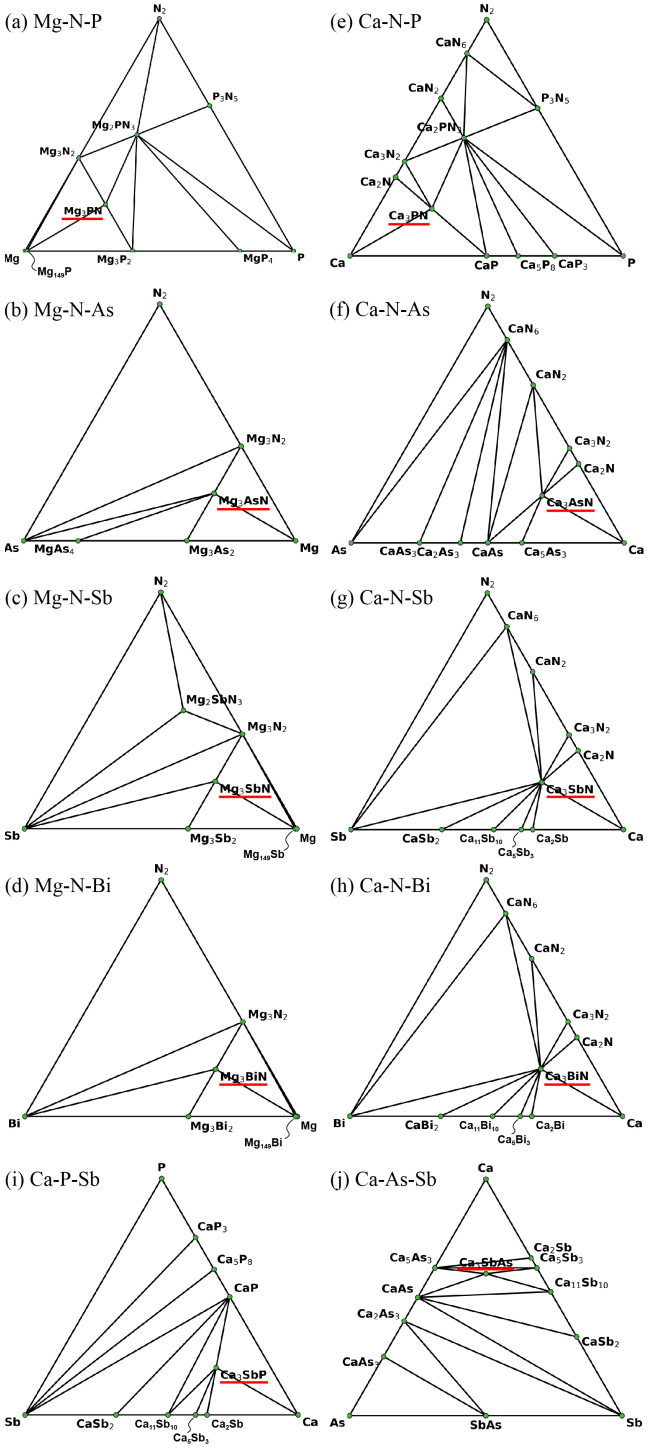

Figure 6.1 Ternary phase diagrams including (a-d) Mg and (e-j) Ca APs.

Table 6.2 Summary of predicted properties of Mg and Ca AP compounds. Bulk modulus in parentheses is a value predicted by the Murnaghan EOS fitting.

Compounds	*t*	Thermodynamic stability	Limiting barrier (meV)		Chemical stability window (V)	Band gap (eV)	Modulus (GPa)	
			Vacancy	Dumbbell			Bulk	Shear
Mg_3NP	0.823	Stable	517	162	0.01 ~ 0.52	2.79	90.5 (89.1)	69.6
Mg_3NAs	0.851	Stable (Synthesized)[294]	519	195	-0.41 ~ 1.18	2.68	87.9 (84.9)	71.7
Mg_3NSb	0.916	Stable (Synthesized)[294]	759	246	0.02 ~ 0.78	1.78	80.3 (78.2)	62.1
Mg_3NBi	0.925	Stable	723	706	0.02 ~ 0.39	1.59	74.3 (72.1)	55.5
Ca_3NP	0.812	Stable (Synthesized)[293]	446	132	-2.22 ~ 0.92	2.68	62.0 (62.5)	42.6
Ca_3NAs	0.837	Stable (Synthesized)[293]	508	171	-0.38 ~ 1.68	2.14	60.0 (60.9)	45.7
Ca_3NSb	0.896	Stable (Synthesized)[293]	865	233	-0.57 ~ 1.85	1.70	57.8 (57.9)	49.5
Ca_3NBi	0.904	Stable (Synthesized)[293]	900	247	-0.56 ~ 1.71	1.65	54.1 (54.1)	47.0
Ca_3PSb	0.780	Stable	433	206	-1.99 ~ 1.41	2.14	39.8 (40.1)	21.1
Ca_3AsSb	0.757	Stable	373	321	0.64 ~ 1.33	2.00	36.9 (36.8)	18.0

Percolating barrier. Figure 6.2 presents the distribution of energy barriers and limiting barriers (listed in Table 6.2). An elementary barrier of a cubic AP is equivalent to the limiting barrier. An AP compound with lattice distortions shows the spectrum of barriers; the low limit of the spectrum decreases linearly and the high limit increases exponentially with smaller tolerance factor, similar to monovalent APs, and limiting barriers can be made by connecting low-barrier

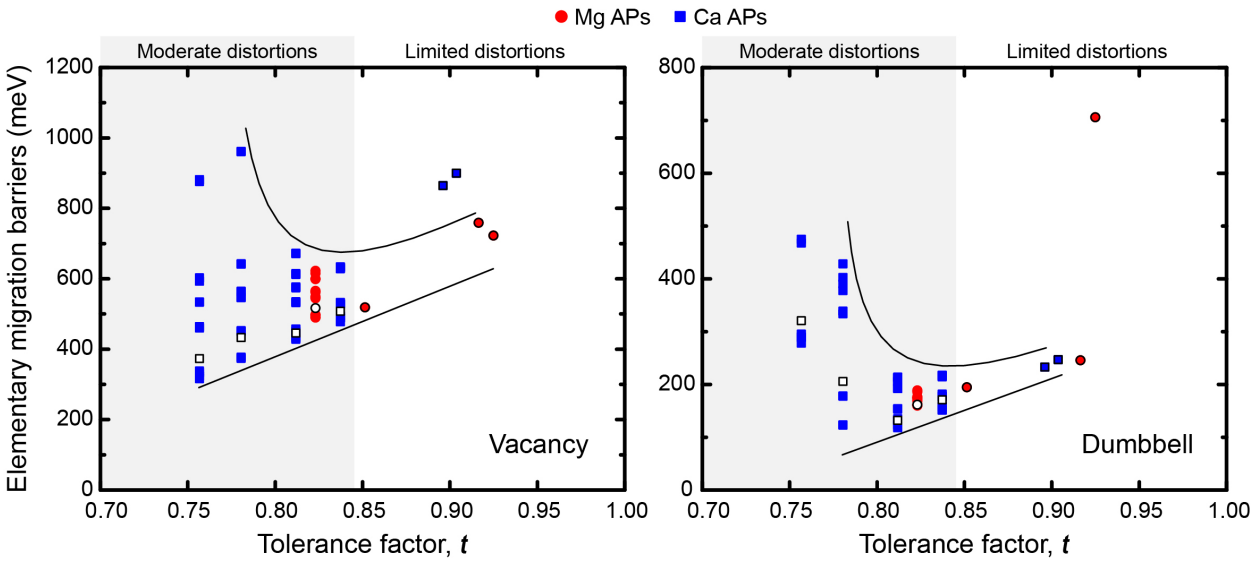

Figure 6.2 Dispersion of elementary migration barriers as a function of the tolerance factor (t) for vacancy and interstitial dumbbell migration mechanisms. APs in the area of limited distortions have a distinct energy barrier, equivalent to the limiting barrier. The spectrum of barriers appears with lattice distortions, and an unfilled shape denotes the position of limiting barrier in the spectrum. Black solid line and curve are guides for linear decrease and exponential increase in barriers with smaller tolerance factor.

paths. Therefore, the limiting barrier decreases linearly with greater lattice distortions. Note that the dumbbell limiting barriers of Ca_3PSb and Ca_3AsSb increase even with low tolerance factors because no low-energy barrier is available owing to unstable defect sites (not all 12 paths are available).

Many Mg and Ca APs have vacancy limiting barriers lower than 525 meV, which is required to satisfy C/2 rate.[45] The limiting barrier can even lower than 200 meV with the dumbbell mechanism, surpassing activation energies of state-of-the-art MV SEs $MgSc_2Se_4$ (370 meV) and PEGDA-Ca polymer (250 meV).[40,280] Also, the limiting barrier can be further reduced in compositions having greater lattice distortions or that employ complex anions (paddle-wheel effect).[194]

Defect formation energy. Previous studies suggested that the formation energies of defects in Li_3OCl are very high (at least 0.93 eV, Table 6.3), so no enough defect concentration can be secured at a thermodynamic equilibrium.[66,69,71,72] Therefore, defects need to be frozen into the lattice during synthesis, e.g., LiCl deficient samples ($Li_{3-x}OCl_x$) and Sr^{2+} doping in Na APs.[64,65] Here, we study the formation energies of various defects in Mg and Ca APs; the following paragraph will describe the types of defects.

Table 6.3 Formation energies of six different defects in Mg and Ca APs (also Li_3OCl for comparison). Values marked by an asterisk indicate the defect with the smallest formation energy for an AP.

Compounds	*t*	Defect formation energy (eV per defect pair)					
		Vacancy	Interstitial	Frenkel	AP Schottky	X_xA_y Schottky	X_xB_y Schottky
Li_3OCl	0.823	3.98	3.17	1.59 [69]	1.44 [69]	1.56 [69]	0.93 * [69]
Mg_3NP	0.823	3.46 *	4.53	4.33	8.53	9.09	8.26
Mg_3NAs	0.851	2.84 *	4.57	4.22	7.34	7.91	7.04
Mg_3NSb	0.916	2.57 *	4.45	5.05	7.08	6.63	7.77
Mg_3NBi	0.925	2.14 *	4.44	4.87	6.17	5.16	7.07
Ca_3NP	0.812	3.89	3.36 *	4.35	8.97	6.61	3.93
Ca_3NAs	0.837	3.30	3.20 *	4.14	8.46	6.02	3.93
Ca_3NSb	0.896	3.31 *	3.65	5.44	8.70	5.88	9.70
Ca_3NBi	0.904	5.53	8.45	5.54	6.70	3.13 *	3.87
Ca_3PSb	0.780	4.20	1.53 *	3.23	8.98	7.73	6.57
Ca_3AsSb	0.757	3.91	1.20 *	2.73	8.28	3.56	6.09

The cation vacancy or interstitial dumbbell is a simple point defect by removing or adding a Mg/Ca atom in a supercell. The *Frenkel* defect is a pair of point defects that an atom dislocates from its normal site to an interstitial site, thus making both a vacancy and an interstitial defects.[122] A Mg/Ca atom at a site is removed and an interstitial dumbbell is made at the other site in a AP supercell. The *Schottky* defect is a pair of vacancies by completely removing a pair of cation and anion in a stoichiometry, e.g., removing a f.u. of X_3AB, X_xA_y, or X_xB_y from a supercell.[122] Mg_3A_2 (A = N) and Mg_3B_2 (B = P, As, Sb, or Bi) were used for Mg APs, which are two end members of convex hull along the tie line in the phase diagram. Since only Ca_3N_2 appears in the ICSD database, Ca_2N, CaP, CaAs, Ca_2Sb, and Ca_2Bi were used for X_xA_y and X_xB_y depending on the composition of Ca APs.

The formation energies of various defects in MV APs are listed in Table 6.3. The vacancy or interstitial defect has the smallest formation energy in most of Mg and Ca APs. All Mg and Ca APs have significantly large formation energies of defects; the smallest formation energies are in a range of 1.2 ~ 3.5 eV. Therefore, the concentration of defects in Mg and Ca APs would be significantly low at an equilibrium, and thus defects should be introduced during the synthesis.

Chemical stability window. Figure 6.3 shows the stable range of Mg and Ca APs with respect to a metal anode as a function of the applied external potential (ranges also listed in Table

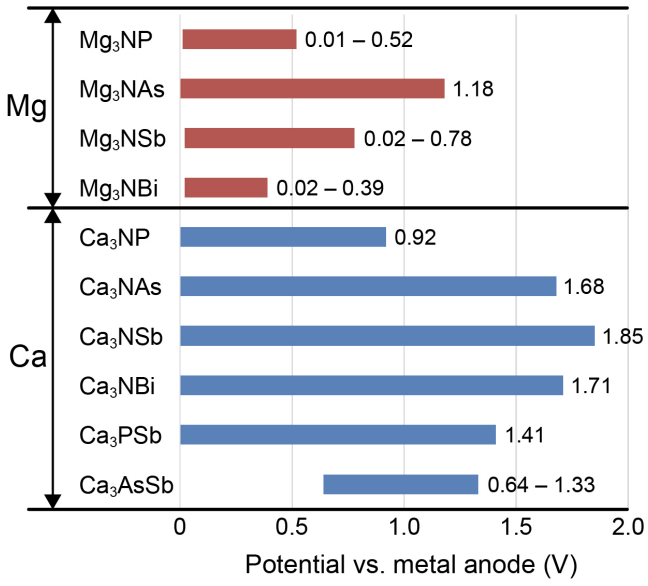

Figure 6.3 Chemical stability window of Mg and Ca APs. All compounds except Ca_3AsSb are stable against metal anode without applied potential. The oxidation limit in the right-end of window is the highest viable voltage without interface treatments.

2). The reduction limits (left-end of window) of Mg APs are at most 0.02 V; thus, they are virtually stable with Mg metal. All Ca APs except Ca_3AsSb are also stable with Ca metal. Therefore, Mg and Ca APs are advantageous to use a metal anode. The oxidation limits of Mg APs are in a range of 0.39 ~ 1.18 V and those of Ca APs are between 0.92 ~ 1.85 V, so Ca APs usually have wider viable voltage ranges than Mg APs. However, the highest voltage limit is not high, i.e., 1.18 V of Mg_3NAs and 1.85 V of Ca_3NSb, thus coating at cathode interfaces between these APs and a metal anode would be needed for cells working at voltages over APs' oxidation limits.

Other properties. The predicted band gaps of Mg and Ca APs are in a range of 1.65 ~ 2.79 eV (Table 6.2). A previous study showed that Ca_3NBi and Ca_3NSb have a semi-conducting behavior whereas Ca_3NAs and Ca_3NP are insulators.[293] It agrees with our predictions that the band gap decreases with larger anion. So, Ca_3NBi and Ca_3NSb are not good candidates for SEs, and we presume that Mg_3NBi and Mg_3NSb having similar band gaps are also semi-conductors. Mg_3NAs and Mg_3NP are expected to have an insulating behavior since they have larger band gaps than Ca_3NP.

The predicted bulk and shear moduli of Mg and Ca APs are listed in Table 2. Mg APs have very large moduli at least 74 GPa of bulk and 55 GPa of shear moduli. Ca_3NB (B = P, As, Sb, or Bi) also have large moduli over 54 GPa of bulk and 47 GPa of shear moduli, and Ca_3ASb (A = P or As) have 18 and 21 GPa of shear moduli, respectively. A previous study suggested that the dendrite initiation may be suppressed if a SE has at least 1.8 times larger shear modulus than a metal anode (assuming that the Poisson's ratio is 0.33).[14] All Mg and Ca APs have at least 2.5 times larger shear moduli than Mg or Ca metal (shear moduli of Mg and Ca metals are 17 and 7.4 GPa, respectively),[300,301] thus may prevent the dendrite formation. However, the dendrite might still penetrate by several mechanisms, e.g., grain boundary softening.[302]

6.3.3 Potential Multivalent Anti-perovskites for Solid Electrolytes

The predicted properties of Mg and Ca APs were compared to find candidates for MV-ion conducting SEs. Among Mg APs, Mg_3NAs has lower limiting barriers than Mg_3NSb and Mg_3NBi. Mg_3NAs has similar limiting barriers, band gap, and moduli to Mg_3NP, but also have more than twice wider stable voltage range than Mg_3NP. Therefore, Mg_3NAs is anticipated to be a potential candidate for a SE. Also, Ca_3NAs would be a SE candidate because of its lower limiting barriers

than Ca_3NSb and Ca_3NBi and much wider stable voltage limit than Ca_3NP. Both Mg_3NAs and Ca_3NAs are believed to have electron-insulating behaviors as discussed. Although having a lower voltage limit than Ca_3NAs, Ca_3PSb has a lower vacancy limiting barrier, which will be advantageous for high cation mobilities if vacancies are dominant over interstitial dumbbells. Also, Ca_3PSb has the same band gap as Ca_3NAs, implying that it might be an electronic insulator. Therefore, we suggest Mg_3NAs, Ca_3NAs, and Ca_3PSb as potential candidates for SEs of MV SSBs.

Inspired by Ca_3PSb, we also simulated the structures and stabilities of Mg_3ASb (A = P or As). Similar to Ca versions, they are also predicted to have orthorhombic structures (lattice parameters a, b, and c are 6.950, 6.862, and 9.906 Å for Mg_3PSb and 7.059, 6.966, and 10.239 Å for Mg_3AsSb). However, they are not stable at zero Kelvin and prone to decompose into Mg_3P_2 + Mg_3Sb_2 and Mg_3As_2 + Mg_3Sb_2 with -34.6 and -49.6 meV/atom exothermic reaction energies, respectively. Also, they have a narrow chemical stability window with the oxidation potential limit up to 0.61 V. Therefore, they will not be good SE candidates.

6.4 Conclusions

Although in the early stage of development, MV SSBs are expected as future technologies for high volumetric capacities without safety concerns. The present study has investigated ten Mg and Ca AP compounds Mg_3NB, Ca_3NB, Ca_3PSb, and Ca_3AsSb (where B = P, As, Sb, or Bi) to discover potential MV SEs. In particular, ground-state structures, thermodynamic stability, long-range percolating barrier, defect formation energy, chemical stability window, band gap, and elastic moduli were predicted by first-principles calculations at the atomic scale.

All compounds were predicted to be stable at zero Kelvin (without zero-point energy). It shows a good agreement to the previous experiments that Mg_3NB (where B = As or Sb) and Ca_3NB (where B = P, As, Sb, or Bi) have been synthesized. Therefore, other four compounds are also expected to be synthesizable. Mg and Ca APs have similar tolerance factor regimes for the degree of lattice distortions as monovalent APs, and follow the trend that the limiting barrier decreases with larger distortions (smaller tolerance factor, t). The formation energies of defects are very high, so defects need to be introduced in the lattice during synthesis. The predicted moduli indicate that these compounds have at least 2.5 times stiffer shear moduli than Mg or Ca metal, satisfying Monroe and Newman's dendrite-suppression criterion.

We suggest Mg_3NAs, Ca_3NAs, and Ca_3PSb as potential candidates for SEs of MV SSBs. These compounds have limiting barriers close or lower than 500 meV for vacancy and 200 meV for interstitial dumbbell migration mechanisms. Ca_3NAs is shown as an electronic insulator and Mg_3NAs and Ca_3PSb are predicted to have the same or larger band gaps than Ca_3NAs, thus they would also have insulating behaviors. They are stable in a contact with a metal anode and the oxidation limits are 1.2, 1.7, and 1.4 V, respectively, thus treatments like coating at a cathode interface would be needed for cells with these APs to operate at voltages over the limits. In total, we screened Mg and Ca APs to discover potential MV-ion conducting SEs, which will aid in the advance of Mg and Ca SSBs with metal anodes.

Chapter 7 Conclusions and Next Steps

Improvements in battery technologies are driven by emerging applications such as electric vehicles. For these applications it is desirable to increase energy density and minimize safety concerns. SSBs using a SE with a metal anode have the potential to achieve both of these goals. Key properties of SEs that promote the viability of SSB are fast ion conduction and good stability and wettability at interfaces between a SE and the electrodes. As a step towards understanding these properties, this dissertation has focused on the following topics: (1) phenomena at anode/SE interfaces, (2) mechanisms associated with fast ion transport in inorganic solids, and (3) the discovery of potential monovalent and MV-ion conducting SEs. The AP compound Li_3OCl (LOC) was adopted as a model SE by virtue of its high ionic conductivity and its reported compatibility with Li metal. The simple crystal structure LOC (and for all anti-perovskites) enables a comprehensive characterization of its properties using computationally-expensive electronic-structure calculations (DFT). Monovalent and MV analogues of LOC, as well as those based on isovalent-anion substitutions, were also explored to screen for potential new SEs and to inform a machine learning study of the features that most strongly impact ion mobility in these compounds.

Chapter 3 examined the thermodynamic properties and electronic structure of interfaces between Li metal and LOC in detail. The wetting of LOC by Li was found to change dramatically as a function of interfacial composition. The oxygen-terminated Li/LOC interface is the most thermodynamically stable and the most strongly adherent with Li. This strong interaction results in a low contact angle and good wettability for Li. However, this strong interfacial interaction significantly narrows the electrochemical window of LOC in the interfacial region by shifting both the CBM and VBM. This suggests a tradeoff between strong interfacial bonding/wettability and electrochemical stability. Nevertheless, the CBM in LOC remains ~1 V more negative than the Li/Li^+ redox potential, suggesting that LOC remains stable against reduction by the anode. In future studies this approach could be used to investigate oxidative stability at interfaces with cathode materials.

Chapter 4 described the atomic-scale connections between ionic mobility, thermodynamic stability, and symmetry-lowering lattice distortions across a series of 36 model APs. The degree of lattice distortion, quantified by the tolerance factor, t, was varied via isovalent composition variations, i.e., X_3AB (X = Li, Na, or K, A = O, S, or Se, and B = F, Cl, Br, or I). Our calculations show a strong correlation, wherein compounds with larger distortions exhibit migration barriers that are smaller for some pathways. The energetic spread between migration barriers due to symmetry-lowering lattice distortions slows migration along some pathways, while speeding up others. In the case of the APs, these lower-barrier hops can be assembled into a percolating network. At the same time, a higher degree of lattice distortion also correlates with diminished thermodynamic stability. Thus, realizing those compounds having the highest ionic mobility in this class of conductors will require balancing a tradeoff with stability. An analysis of the thermal stabilization of AP compounds suggests that Li_3SeF, Na_3SeF, Na_3SBr, Na_3SF, K_3SeF, and K_3SBr are promising materials that balance high ion mobility with stability at moderate temperatures. These materials are also predicted to be stable against alkali metal anodes, and thus can potentially be considered as candidates for SSBs that use a metal anode.

The present results teach us that perturbations (or intentional frustrations) to ion-packing, introduced via isovalent substitution, leads to lattice distortions and symmetry-breaking. These effects remove the degeneracy of the migration barriers in the non-distorted materials, and can open up ion-migration channels with potentially lower barriers. In principle, this concept could be applied to additional crystalline materials beyond the anti-perovskites examined here. The investigation of this approach to other classes of fast ion conductors is a potential next step.

A comparison between the mobility of three alkali metal ions (Li, Na, and K) in the anti-perovskite structure was performed. Contrary to expectations based on ionic radii, larger alkali ion generally has higher mobility than smaller one in the AP lattice. The observed differences in mobility can be explained by 4 factors: an AP compound with larger alkali ion has 1) a lower packing fraction that leads to wider free space for cations to move through, 2) greater vibration amplitudes (smaller low-energy optical phonon frequency) that facilitate migrations of cations, 3) higher polarizabilities that lead to softer lattice stiffness and flexible electron clouds of ions, and 4) much weaker electrostatic attraction between ions due to lower net charges (covalency effect) according to the Bader charge.

Using data from DFT simulations, Chapter 5 used ML to uncover the relative importance of features that promote ion migration in anti-perovskites. The ML analysis revealed that lattice properties have the greatest influence on ion mobility regardless of mechanism. The path distance and bottleneck-geometry are the most important features for vacancy migration, together accounting for 78% of the total importance. The path distance, CCD, has the largest importance (29%) of any single feature, while three bottleneck-related features occupy a total of 49% importance (distance to the nearest anion from migration path, PW_c 23%; total path width, PW 17%; packing fraction without cation, PF_C 9%). Since bottleneck-related features are closely related, a simplified ML model was built using a moderate filtering threshold ($|\rho| \geq 0.80$) that leads to 20 features for the optimization of the ML algorithm. This model again showed that CCD (42%) and PW (28%) appear as top 2 features, which further supports our analysis that lattice properties are the most influential in the vacancy migration. The elementary migration barrier decreases with a shorter path distance and wider bottleneck for migration, thus decreasing the distance between mobile cations and keeping framework ions away from paths will be helpful for achieving high vacancy mobility. For migration of interstitials, bottleneck-related features occupy 73% importance (PW 40%; cation – framework anion distance, CFD 19%; PF_C 14%). PW and PF_C, important features for vacancies, also appear in the feature subset of dumbbell. This ML analysis could be generalized by including migration data from other types of solid materials and to systems involving transport of MV ions.

Finally, the study was extended to MV-ion containing APs as potential SEs (Chapter 6). Ten non-metallic Mg and Ca AP compounds were examined: Mg_3NB, Ca_3NB, Ca_3PSb, and Ca_3AsSb (where B = P, As, Sb, or Bi). All compounds were predicted to be stable at zero Kelvin and stiff enough to satisfy Monroe and Newman's dendrite-suppression criterion. The results suggest Mg_3NAs, Ca_3NAs, and Ca_3PSb are the most promising potential MV SE candidates. These compounds have limiting barriers close or lower than 500 meV for vacancy migration which would allow operation at C/2. The limiting barrier can even lower than 200 meV assuming an interstitial dumbbell mechanism, surpassing activation energies of state-of-the-art MV SEs $MgSc_2Se_4$ (370 meV) and PEGDA-Ca polymer (250 meV). These materials are stable in a contact with their respective Mg or Ca anode, and are stable against oxidation for voltages ranging from 1.2 to 1.7 V. Thus, interfacial coatings may be needed for these APs to operate with high voltage cathodes. A preliminary analysis suggests that the formation energies for defects is high, so high carrier

concentrations may need to be introduced in the lattice during synthesis or via doping. Experimental studies of these materials are called for to validate the present ion mobility predictions.

In total, this study investigated solid electrolyte interfacial phenomena, revealed factors that describe ion migrations in solids, and identified new materials for monovalent- and MV-ion conducting SEs. This work will aid in the systematic design of optimal SEs and accelerate the commercialization of safe, energy dense, and longer-lasting SSBs.

Bibliography

(1) Cazenave, A.; Palanisamy, H. Sea Level Rise and Future Earth. In *Global Change and Future Earth*; Beer, T., Li, J., Alverson, K., Eds.; Cambridge University Press: Cambridge, UK, 2018; pp 144–158.

(2) Larcher, D.; Tarascon, J.-M. Towards Greener and More Sustainable Batteries for Electrical Energy Storage. *Nat. Chem.* **2015**, *7* (1), 19–29.

(3) Goodenough, J. B.; Kim, Y. Challenges for Rechargeable Li Batteries. *Chem. Mater.* **2010**, *22* (3), 587–603.

(4) Kim, S. W.; Seo, D. H.; Ma, X.; Ceder, G.; Kang, K. Electrode Materials for Rechargeable Sodium-Ion Batteries: Potential Alternatives to Current Lithium-Ion Batteries. *Adv. Energy Mater.* **2012**, *2* (7), 710–721.

(5) Eftekhari, A.; Jian, Z.; Ji, X. Potassium Secondary Batteries. *ACS Appl. Mater. Interfaces* **2017**, *9* (5), 4404–4419.

(6) Kim, H.; Kim, J. C.; Bianchini, M.; Seo, D. H.; Rodriguez-Garcia, J.; Ceder, G. Recent Progress and Perspective in Electrode Materials for K-Ion Batteries. *Adv. Energy Mater.* **2018**, *8* (9), 1–19.

(7) Muldoon, J.; Bucur, C. B.; Gregory, T. Quest for Nonaqueous Multivalent Secondary Batteries: Magnesium and Beyond. *Chem. Rev.* **2014**, *114* (23), 11683–11720.

(8) Tesla Model S https://www.tesla.com/models (accessed Mar 2, 2020).

(9) 2019 Jaguar XF 20d Premium Sedan RWD Features and Specs https://www.caranddriver.com/jaguar/xf/specs/2019/jaguar_xf_2019-jaguar-xf_2019/400713 (accessed Mar 2, 2020).

(10) Ford Focus https://www.ford.com/cars/focus/ (accessed Apr 24, 2019).

(11) Shepardson, D. U.S. Opens Probe into Fatal Tesla Crash, Fire in California. *Reuters*. March 27, 2018.

(12) Roth, E. P.; Orendorff, C. J. How Electrolytes Influence Battery Safety. *Electrochem. Soc. Interface* **2012**, *21* (2), 45–49.

(13) Goodenough, J. B.; Singh, P. Review—Solid Electrolytes in Rechargeable Electrochemical Cells. *J. Electrochem. Soc.* **2015**, *162* (14), A2387–A2392.

(14) Monroe, C.; Newman, J. The Impact of Elastic Deformation on Deposition Kinetics at Lithium/Polymer Interfaces. *J. Electrochem. Soc.* **2005**, *152* (2), A396–A404.

(15) Yu, S.; Schmidt, R. D.; Garcia-Mendez, R.; Herbert, E.; Dudney, N. J.; Wolfenstine, J. B.; Sakamoto, J.; Siegel, D. J. Elastic Properties of the Solid Electrolyte $Li_7La_3Zr_2O_{12}$ (LLZO). *Chem. Mater.* **2016**, *28* (1), 197–206.

(16) Hu, Y.-S. Batteries: Getting Solid. *Nat. Energy* **2016**, *1* (4), 16042.

(17) Jung, Y. C.; Kim, S. K.; Kim, M. S.; Lee, J. H.; Han, M. S.; Kim, D. H.; Shin, W. C.; Ue, M.; Kim, D. W. Ceramic Separators Based on Li^+-Conducting Inorganic Electrolyte for High-Performance Lithium-Ion Batteries with Enhanced Safety. *J. Power Sources* **2015**, *293*, 675–683.

(18) Albertus, P.; Babinec, S.; Litzelman, S.; Newman, A. Status and Challenges in Enabling the Lithium Metal Electrode for High-Energy and Low-Cost Rechargeable Batteries. *Nat. Energy* **2018**, *3* (1), 16–21.

(19) Murugan, R.; Thangadurai, V.; Weppner, W. Fast Lithium Ion Conduction in Garnet-Type $Li_7La_3Zr_2O_{12}$. *Angew. Chemie - Int. Ed.* **2007**, *46* (41), 7778–7781.

(20) Deiseroth, H.-J.; Kong, S. T.; Eckert, H.; Vannahme, J.; Reiner, C.; Zaiß, T.; Schlosser, M. Li_6PS_5X: A Class of Crystalline Li-Rich Solids with an Unusually High Li^+ Mobility. *Angew. Chemie - Int. Ed.* **2008**, *47* (4), 755–758.

(21) Kamaya, N.; Homma, K.; Yamakawa, Y.; Hirayama, M.; Kanno, R.; Yonemura, M.; Kamiyama, T.; Kato, Y.; Hama, S.; Kawamoto, K.; et al. A Lithium Superionic Conductor. *Nat. Mater.* **2011**, *10* (9), 682–686.

(22) Kato, Y.; Hori, S.; Saito, T.; Suzuki, K.; Hirayama, M.; Mitsui, A.; Yonemura, M.; Iba, H.; Kanno, R. High-

Power All-Solid-State Batteries Using Sulfide Superionic Conductors. *Nat. Energy* **2016**, *1* (4), 16030.

(23) Bates, J. B.; Dudney, N. J.; Gruzalski, G. R.; Zuhr, R. A.; Choudhury, A.; Luck, C. F.; Robertson, J. D. Fabrication and Characterization of Amorphous Lithium Electrolyte Thin Films and Rechargeable Thin-Film Batteries. *J. Power Sources* **1993**, *43* (1–3), 103–110.

(24) Hayashi, A.; Hama, S.; Minami, T.; Tatsumisago, M. Formation of Superionic Crystals from Mechanically Milled Li_2S-P_2S_5 Glasses. *Electrochem. commun.* **2003**, *5* (2), 111–114.

(25) Aono, H.; Sugimoto, E.; Sadaoka, Y.; Imanaka, N.; Adachi, G. Ionic Conductivity of Solid Electrolytes Based on Lithium Titanium Phosphate. *J. Electrochem. Soc.* **1990**, *137* (4), 1023–1027.

(26) Inaguma, Y.; Liquan, C.; Itoh, M.; Nakamura, T.; Uchida, T.; Ikuta, H.; Wakihara, M. HIGH IONIC CONDUCTIVITY IN LITHIUM LANTHANUM TITANATE. *Solid State Commun.* **1993**, *86* (10), 689–693.

(27) Goodenough, J. B.; Hong, H. Y.-P.; Kafalas, J. A. FAST Na^+ - ION TRANSPORT IN SKELETON STRUCTURES. *Mater. Res. Bull.* **1976**, *11* (2), 203–220.

(28) Hayashi, A.; Noi, K.; Sakuda, A.; Tatsumisago, M. Superionic Glass-Ceramic Electrolytes for Room-Temperature Rechargeable Sodium Batteries. *Nat. Commun.* **2012**, *3* (May), 855–856.

(29) Richards, W. D.; Tsujimura, T.; Miara, L. J.; Wang, Y.; Kim, J. C.; Ong, S. P.; Uechi, I.; Suzuki, N.; Ceder, G. Design and Synthesis of the Superionic Conductor $Na_{10}SnP_2S_{12}$. *Nat. Commun.* **2016**, *7*, 11009.

(30) Zhang, Z.; Ramos, E.; Lalère, F.; Assoud, A.; Kaup, K.; Hartman, P.; Nazar, L. F. $Na_{11}Sn_2PS_{12}$: A New Solid State Sodium Superionic Conductor. *Energy Environ. Sci.* **2018**, *11* (1), 87–93.

(31) Matsuo, M.; Oguchi, H.; Sato, T.; Takamura, H.; Tsuchida, E.; Ikeshoji, T.; Orimo, S. I. Sodium and Magnesium Ionic Conduction in Complex Hydrides. *J. Alloys Compd.* **2013**, *580* (Supplement 1), S98–S101.

(32) Tang, W. S.; Unemoto, A.; Zhou, W.; Stavila, V.; Matsuo, M.; Wu, H.; Orimo, S. I.; Udovic, T. J. Unparalleled Lithium and Sodium Superionic Conduction in Solid Electrolytes with Large Monovalent Cage-like Anions. *Energy Environ. Sci.* **2015**, *8* (12), 3637–3645.

(33) Bachman, J. C.; Muy, S.; Grimaud, A.; Chang, H. H.; Pour, N.; Lux, S. F.; Paschos, O.; Maglia, F.; Lupart, S.; Lamp, P.; et al. Inorganic Solid-State Electrolytes for Lithium Batteries: Mechanisms and Properties Governing Ion Conduction. *Chem. Rev.* **2016**, *116* (1), 140–162.

(34) Richards, W. D.; Miara, L. J.; Wang, Y.; Kim, J. C.; Ceder, G. Interface Stability in Solid-State Batteries. *Chem. Mater.* **2016**, *28* (1), 266–273.

(35) Cheng, E. J.; Sharafi, A.; Sakamoto, J. Intergranular Li Metal Propagation through Polycrystalline $Li_{6.25}Al_{0.25}La_3Zr_2O_{12}$ Ceramic Electrolyte. *Electrochim. Acta* **2017**, *223*, 85–91.

(36) Zhu, Y.; He, X.; Mo, Y. Origin of Outstanding Stability in the Lithium Solid Electrolyte Materials: Insights from Thermodynamic Analyses Based on First-Principles Calculations. *ACS Appl. Mater. Interfaces* **2015**, *7* (42), 23685–23693.

(37) Jain, A.; Ong, S. P.; Hautier, G.; Chen, W.; Richards, W. D.; Dacek, S.; Cholia, S.; Gunter, D.; Skinner, D.; Ceder, G.; et al. Commentary: The Materials Project: A Materials Genome Approach to Accelerating Materials Innovation. *APL Mater.* **2013**, *1* (1), 011002.

(38) Wang, Y.; Richards, W. D.; Ong, S. P.; Miara, L. J.; Kim, J. C.; Mo, Y.; Ceder, G. Design Principles for Solid-State Lithium Superionic Conductors. *Nat. Mater.* **2015**, *14* (10), 1026–1031.

(39) Sendek, A. D.; Yang, Q.; Cubuk, E. D.; Duerloo, K.-A. N.; Cui, Y.; Reed, E. J. Holistic Computational Structure Screening of More than 12 000 Candidates for Solid Lithium-Ion Conductor Materials. *Energy Environ. Sci.* **2017**, *10* (1), 306–320.

(40) Canepa, P.; Bo, S. H.; Sai Gautam, G.; Key, B.; Richards, W. D.; Shi, T.; Tian, Y.; Wang, Y.; Li, J.; Ceder, G. High Magnesium Mobility in Ternary Spinel Chalcogenides. *Nat. Commun.* **2017**, *8*, 1759.

(41) Liu, W.; Lee, S. W.; Lin, D.; Shi, F.; Wang, S.; Sendek, A. D.; Cui, Y. Enhancing Ionic Conductivity in Composite Polymer Electrolytes with Well-Aligned Ceramic Nanowires. *Nat. Energy* **2017**, *2* (5), 1–7.

(42) Wakamura, K. Roles of Phonon Amplitude and Low-Energy Optical Phonons on Superionic Conduction. *Phys. Rev. B - Condens. Matter Mater. Phys.* **1997**, *56* (18), 11593–11599.

(43) Muy, S.; Bachman, J. C.; Giordano, L.; Chang, H.; Abernathy, D. L.; Bansal, D.; Delaire, O.; Hori, S.; Kanno, R.; Maglia, F.; et al. Tuning Mobility and Stability of Lithium Ion Conductors Based on Lattice Dynamics. *Energy Environ. Sci.* **2018**, *11* (4), 850–859.

(44) Kraft, M. A.; Culver, S. P.; Calderon, M.; Böcher, F.; Krauskopf, T.; Senyshyn, A.; Dietrich, C.; Zevalkink, A.; Janek, J.; Zeier, W. G. Influence of Lattice Polarizability on the Ionic Conductivity in the Lithium Superionic Argyrodites Li_6PS_5X (X = Cl, Br, I). *J. Am. Chem. Soc.* **2017**, *139* (31), 10909–10918.

(45) Rong, Z.; Malik, R.; Canepa, P.; Sai Gautam, G.; Liu, M.; Jain, A.; Persson, K.; Ceder, G. Materials Design Rules for Multivalent Ion Mobility in Intercalation Structures. *Chem. Mater.* **2015**, *27* (17), 6016–6021.

(46) Ong, S. P.; Mo, Y.; Richards, W. D.; Miara, L.; Lee, H. S.; Ceder, G. Phase Stability, Electrochemical Stability and Ionic Conductivity of the $Li_{10\pm1}MP_2X_{12}$ (M = Ge, Si, Sn, Al or P, and X = O, S or Se) Family of Superionic Conductors. *Energy Environ. Sci.* **2013**, *6* (1), 148–156.

(47) Zhang, Z.; Shao, Y.; Lotsch, B.; Hu, Y.-S.; Li, H.; Janek, J.; Nazar, L. F.; Nan, C.; Maier, J.; Armand, M.; et al. New Horizons for Inorganic Solid State Ion Conductors. *Energy Environ. Sci.* **2018**, *11* (8), 1945–1976.

(48) Zhu, Y.; He, X.; Mo, Y. First Principles Study on Electrochemical and Chemical Stability of Solid Electrolyte–Electrode Interfaces in All-Solid-State Li-Ion Batteries. *J. Mater. Chem. A* **2016**, *4* (9), 3253–3266.

(49) Han, F.; Zhu, Y.; He, X.; Mo, Y.; Wang, C. Electrochemical Stability of $Li_{10}GeP_2S_{12}$ and $Li_7La_3Zr_2O_{12}$ Solid Electrolytes. *Adv. Energy Mater.* **2016**, *6* (8), 1501590.

(50) Rettenwander, D.; Wagner, R.; Reyer, A.; Bonta, M.; Cheng, L.; Doeff, M. M.; Limbeck, A.; Wilkening, M.; Amthauer, G. Interface Instability of Fe-Stabilized $Li_7La_3Zr_2O_{12}$ versus Li Metal. *J. Phys. Chem. C* **2018**, *122* (7), 3780–3785.

(51) Han, X.; Gong, Y.; Fu, K. (Kelvin); He, X.; Hitz, G. T.; Dai, J.; Pearse, A.; Liu, B.; Wang, H.; Rubloff, G.; et al. Negating Interfacial Impedance in Garnet-Based Solid-State Li Metal Batteries. *Nat. Mater.* **2016**, *16* (5), 572–579.

(52) Li, Y.; Zhou, W.; Chen, X.; Lü, X.; Cui, Z.; Xin, S.; Xue, L.; Jia, Q.; Goodenough, J. B. Mastering the Interface for Advanced All-Solid-State Lithium Rechargeable Batteries. *Proc. Natl. Acad. Sci.* **2016**, *113* (47), 13313–13317.

(53) Sharafi, A.; Kazyak, E.; Davis, A. L.; Yu, S.; Thompson, T.; Siegel, D. J.; Dasgupta, N. P.; Sakamoto, J. Surface Chemistry Mechanism of Ultra-Low Interfacial Resistance in the Solid-State Electrolyte $Li_7La_3Zr_2O_{12}$. *Chem. Mater.* **2017**, *29* (18), 7961–7968.

(54) Kumar, N.; Siegel, D. J. Interface-Induced Renormalization of Electrolyte Energy Levels in Magnesium Batteries. *J. Phys. Chem. Lett.* **2016**, *7* (5), 874–881.

(55) Thompson, T.; Yu, S.; Williams, L.; Schmidt, R. D.; Garcia-Mendez, R.; Wolfenstine, J.; Allen, J. L.; Kioupakis, E.; Siegel, D. J.; Sakamoto, J. Electrochemical Window of the Li-Ion Solid Electrolyte $Li_7La_3Zr_2O_{12}$. *ACS Energy Lett.* **2017**, *2* (2), 462–468.

(56) Zhang, Y.; Zhao, Y.; Chen, C. Ab Initio Study of the Stabilities of and Mechanism of Superionic Transport in Lithium-Rich Antiperovskites. *Phys. Rev. B - Condens. Matter Mater. Phys.* **2013**, *87* (13), 134303.

(57) Luntz, A. C.; Voss, J.; Reuter, K. Interfacial Challenges in Solid-State Li Ion Batteries. *J. Phys. Chem. Lett.* **2015**, *6* (22), 4599–4604.

(58) Manthiram, A.; Yu, X.; Wang, S. Lithium Battery Chemistries Enabled by Solid-State Electrolytes. *Nat. Rev. Mater.* **2017**, *2* (4), 16103.

(59) Luo, W.; Gong, Y.; Zhu, Y.; Li, Y.; Yao, Y.; Zhang, Y.; Fu, K. K.; Pastel, G.; Lin, C. F.; Mo, Y.; et al. Reducing Interfacial Resistance between Garnet-Structured Solid-State Electrolyte and Li-Metal Anode by a Germanium Layer. *Adv. Mater.* **2017**, *29* (22), 1606042.

(60) Tsai, C.-L.; Roddatis, V.; Chandran, C. V.; Ma, Q.; Uhlenbruck, S.; Bram, M.; Heitjans, P.; Guillon, O. $Li_7La_3Zr_2O_{12}$ Interface Modification for Li Dendrite Prevention. *ACS Appl. Mater. Interfaces* **2016**, *8* (16), 10617–10626.

(61) Braga, M. H.; Grundish, N. S.; Murchison, A. J.; Goodenough, J. B. Alternative Strategy for a Safe Rechargeable Battery. *Energy Environ. Sci.* **2017**, *10* (1), 331–336.

(62) Wang, C.; Gong, Y.; Liu, B.; Fu, K.; Yao, Y.; Hitz, E.; Li, Y.; Dai, J.; Xu, S.; Luo, W.; et al. Conformal, Nanoscale ZnO Surface Modification of Garnet-Based Solid-State Electrolyte for Lithium Metal Anodes. *Nano Lett.* **2017**, *17* (1), 565–571.

(63) Fu, K. (Kelvin); Gong, Y.; Liu, B.; Zhu, Y.; Xu, S.; Yao, Y.; Luo, W.; Wang, C.; Lacey, S. D.; Dai, J.; et al. Toward Garnet Electrolyte–Based Li Metal Batteries: An Ultrathin, Highly Effective, Artificial Solid-State Electrolyte/Metallic Li Interface. *Sci. Adv.* **2017**, *3* (4), e1601659.

(64) Zhao, Y.; Daemen, L. L. Superionic Conductivity in Lithium-Rich Anti-Perovskites. *J. Am. Chem. Soc.* **2012**, *134* (36), 15042–15047.

(65) Wang, Y.; Wang, Q.; Liu, Z.; Zhou, Z.; Li, S.; Zhu, J.; Zou, R.; Wang, Y.; Lin, J.; Zhao, Y. Structural Manipulation Approaches towards Enhanced Sodium Ionic Conductivity in Na-Rich Antiperovskites. *J. Power Sources* **2015**, *293*, 735–740.

(66) Emly, A.; Kioupakis, E.; Van der Ven, A. Phase Stability and Transport Mechanisms in Antiperovskite Li_3OCl and Li_3OBr Superionic Conductors. *Chem. Mater.* **2013**, *25* (23), 4663–4670.

(67) Lü, X.; Howard, J. W.; Chen, A.; Zhu, J.; Li, S.; Wu, G.; Dowden, P.; Xu, H.; Zhao, Y.; Jia, Q. Antiperovskite Li_3OCl Superionic Conductor Films for Solid-State Li-Ion Batteries. *Adv. Sci.* **2016**, *3* (3), 1500359.

(68) Lü, X.; Wu, G.; Howard, J. W.; Chen, A.; Zhao, Y.; Daemen, L. L.; Jia, Q. Li-Rich Anti-Perovskite Li_3OCl Films with Enhanced Ionic Conductivity. *Chem. Commun.* **2014**, *50* (78), 11520–11522.

(69) Mouta, R.; Melo, M. Á. B.; Diniz, E. M.; Paschoal, C. W. A. Concentration of Charge Carriers, Migration, and Stability in Li_3OCl Solid Electrolytes. *Chem. Mater.* **2014**, *26* (24), 7137–7144.

(70) Mouta, R.; Diniz, E. M.; Paschoal, C. W. A. Li^+ Interstitials as the Charge Carriers in Superionic Lithium-Rich Anti-Perovskites. *J. Mater. Chem. A* **2015**, *4* (5), 1–3.

(71) Lu, Z.; Chen, C.; Baiyee, Z. M.; Chen, X.; Niu, C.; Ciucci, F. Defect Chemistry and Lithium Transport in Li_3OCl Anti-Perovskite Superionic Conductors. *Phys. Chem. Chem. Phys.* **2015**, *17* (48), 32547–32555.

(72) Stegmaier, S.; Voss, J.; Reuter, K.; Luntz, A. C. Li^+ Defects in a Solid-State Li Ion Battery: Theoretical Insights with a Li_3OCl Electrolyte. *Chem. Mater.* **2017**, *29* (10), 4330–4340.

(73) Deng, Z.; Radhakrishnan, B.; Ong, S. P. Rational Composition Optimization of the Lithium-Rich $Li_3OCl_{1-x}Br_x$ Anti-Perovskite Superionic Conductors. *Chem. Mater.* **2015**, *27* (10), 3749–3755.

(74) Braga, M. H.; Murchison, A. J.; Ferreira, J. A.; Singh, P.; Goodenough, J. B. Glass-Amorphous Alkali-Ion Solid Electrolytes and Their Performance in Symmetrical Cells. *Energy Environ. Sci.* **2016**, *9* (3), 948–954.

(75) Zhu, J.; Li, S.; Zhang, Y.; Howard, J. W.; Lü, X.; Li, Y.; Wang, Y.; Kumar, R. S.; Wang, L.; Zhao, Y. Enhanced Ionic Conductivity with Li7O2Br3 Phase in Li3OBr Anti-Perovskite Solid Electrolyte. *Appl. Phys. Lett.* **2016**, *109* (10), 101904.

(76) Li, Y.; Zhou, W.; Xin, S.; Li, S.; Zhu, J.; Lü, X.; Cui, Z.; Jia, Q.; Zhou, J.; Zhao, Y.; et al. Fluorine-Doped Antiperovskite Electrolyte for All-Solid-State Lithium-Ion Batteries. *Angew. Chemie - Int. Ed.* **2016**, *55* (34), 9965–9968.

(77) Zhu, J.; Wang, Y.; Li, S.; Howard, J. W.; Neuefeind, J.; Ren, Y.; Wang, H.; Liang, C.; Yang, W.; Zou, R.; et al. Sodium Ion Transport Mechanisms in Antiperovskite Electrolytes Na_3OBr and Na_4OI_2: An *in Situ* Neutron Diffraction Study. *Inorg. Chem.* **2016**, *55* (12), 5993–5998.

(78) Hood, Z. D.; Wang, H.; Pandian, A. S.; Keum, J. K.; Liang, C. Li_2OHCl Crystalline Electrolyte for Stable Metallic Lithium Anodes. *J. Am. Chem. Soc.* **2016**, *138* (6), 1768–1771.

(79) Fang, H.; Wang, S.; Liu, J.; Sun, Q.; Jena, P. Superhalogen-Based Lithium Superionic Conductors. *J. Mater. Chem. A* **2017**, *5* (26), 13373–13381.

(80) Fang, H.; Jena, P. Li-Rich Antiperovskite Superionic Conductors Based on Cluster Ions. *Proc. Natl. Acad. Sci.* **2017**, *114* (42), 11046–11051.

(81) Wang, Z.; Xu, H.; Xuan, M.; Shao, G. From Anti-Perovskite to Double Anti-Perovskite: Tuning Lattice Chemistry to Achieve Super-Fast Li^+ Transport in Cubic Solid Lithium Halogen-Chalcogenides. *J. Mater. Chem. A* **2017**, *6* (1), 73–83.

(82) Dawson, J. A.; Canepa, P.; Famprikis, T.; Masquelier, C.; Islam, M. S. Atomic-Scale Influence of Grain Boundaries on Li-Ion Conduction in Solid Electrolytes for All-Solid-State Batteries. *J. Am. Chem. Soc.* **2018**, *140* (1), 362–368.

(83) Wan, T. H.; Lu, Z.; Ciucci, F. A First Principle Study of the Phase Stability, Ion Transport and Substitution Strategy for Highly Ionic Conductive Sodium Antipervoskite as Solid Electrolyte for Sodium Ion Batteries. *J. Power Sources* **2018**, *390*, 61–70.

(84) Dawson, J. A.; Attari, T.; Chen, H.; Emge, S.; Johnston, K. E.; Islam, S. Elucidating Lithium-Ion and Proton Dynamics in Anti-Perovskite Solid Electrolytes. *Energy Environ. Sci.* **2018**, 10.1039/c8ee00779a.

(85) Yu, Y.; Wang, Z.; Shao, G. Theoretical Design of Double Anti-Perovskite Na_6SOI_2 as Super-Fast Ionic

Conductor for Solid Na^+ Ion Batteries. *J. Mater. Chem. A* **2018**, 10.1039/C8TA08412B.

(86) Chen, M.-H.; Emly, A.; Van der Ven, A. Anharmonicity and Phase Stability of Antiperovskite Li_3OCl. *Phys. Rev. B - Condens. Matter Mater. Phys.* **2015**, *91* (21), 214306.

(87) Van de Walle, A.; Ceder, G. The Effect of Lattice Vibrations on Substitutional Alloy Thermodynamics. *Rev. Mod. Phys.* **2002**, *74* (1), 11–45.

(88) Sun, W.; Dacek, S. T.; Ong, S. P.; Hautier, G.; Jain, A.; Richards, W. D.; Gamst, A. C.; Persson, K. A.; Ceder, G. The Thermodynamic Scale of Inorganic Crystalline Metastability. *Sci. Adv.* **2016**, *2* (11), e1600225.

(89) Schrödinger, E. Quantisierung Als Eigenwertproblem. *Ann. Phys.* **1926**, *384* (4), 361–376.

(90) Born, M.; Oppenheimer, R. Zur Quantentheorie Der Molekeln. *Ann. Phys.* **1927**, *389* (20), 457–484.

(91) Sholl, D. S.; Steckel, J. A. *Density Functional Theory: A Practical Introduction*; John Wiley & Sons: Hoboken, New Jersey, 2009.

(92) Griffiths, D. J. *Introduction to Quantum Mechanics*, 2nd ed.; Pearson Prentice Hall: Upper Saddle River, NJ, 2005.

(93) Lee, J. G. *Computational Materials Science: An Introduction*, 2nd ed.; CRC Press: Boca Raton, 2016.

(94) Hartree, D. R. The Wave Mechanics of an Atom with a Non-Coulomb Central Field. Part I. Theory and Methods. *Math. Proc. Cambridge Philos. Soc.* **1928**, *24* (1), 89–110.

(95) Hartree, D. R. The Wave Mechanics of an Atom with a Non-Coulomb Central Field. Part II. Some Results and Discussion. *Math. Proc. Cambridge Philos. Soc.* **1928**, *24* (1), 111–132.

(96) Hartree, D. R. The Wave Mechanics of an Atom with a Non-Coulomb Central Field. Part III. Term Values and Intensities in Series in Optical Spectra. *Math. Proc. Cambridge Philos. Soc.* **1928**, *24* (3), 426–437.

(97) Slater, J. C. The Self Consistent Field and the Structure of Atoms. *Phys. Rev.* **1928**, *32* (3), 339–348.

(98) Fock, V. Näherungsmethode Zur Lösung Des Quantenmechanischen Mehrkörperproblems. *Zeitschrift für Phys.* **1930**, *61* (1–2), 126–148.

(99) Hartree, D. R.; Hartree, F. R. S. Self-Consistent Field, with Exchange, for Beryllium. *Proc. R. Soc. London. Ser. A - Math. Phys. Sci.* **1935**, *150* (869), 9–33.

(100) Hohenberg, P.; Kohn, W. Inhomogeneous Electron Gas. *Phys. Rev.* **1964**, *136* (3B), B864–B871.

(101) Kohn, W.; Sham, L. J. Self-Consistent Equations Including Exchange and Correlation Effects. *Phys. Rev.* **1965**, *140* (4A), A1133–A1138.

(102) Martin, R. M. *Electronic Structure: Basic Theory and Practical Methods*; Cambridge University Press: Cambridge, UK, 2004.

(103) Thomas, L. H. The Calculation of Atomic Fields. *Math. Proc. Cambridge Philos. Soc.* **1927**, *23* (5), 542–548.

(104) Fermi, E. Un Metodo Statistico per La Deter- Minazione Di Alcune Priorieta Dell'atome. *Rend. Accad. Naz. Lincei* **1927**, *6*, 602–607.

(105) Dirac, P. A. M. Note on Exchange Phenomena in the Thomas Atom. *Math. Proc. Cambridge Philos. Soc.* **1930**, *26* (3), 376–385.

(106) Vosko, S. H.; Wilk, L.; Nusair, M. Accurate Spin-Dependent Electron Liquid Correlation Energies for Local Spin Density Calculations: A Critical Analysis. *Can. J. Phys.* **1980**, *58* (8), 1200–1211.

(107) Perdew, J. P.; Wang, Y. Accurate and Simple Analytic Representation of the Electron-Gas Correlation Energy. *Phys. Rev. B* **1992**, *45* (23), 13244–13249.

(108) Ceperley, D. M.; Alder, B. J. Ground State of the Electron Gas by a Stochastic Method. *Phys. Rev. Lett.* **1980**, *45* (7), 566–569.

(109) Kohn, W. Nobel Lecture: Electronic Structure of Matter—Wave Functions and Density Functionals. *Rev. Mod. Phys.* **1999**, *71* (5), 1253–1266.

(110) Perdew, J. P.; Burke, K.; Ernzerhof, M. Generalized Gradient Approximation Made Simple. *Phys. Rev. Lett.* **1996**, *77* (18), 3865–3868.

(111) Aryasetiawan, F.; Gunnarsson, O. The ***GW*** Method. *Reports Prog. Phys.* **1998**, *61* (3), 237–312.

(112) Heyd, J.; Scuseria, G. E.; Ernzerhof, M. Hybrid Functionals Based on a Screened Coulomb Potential. *J. Chem. Phys.* **2003**, *118* (18), 8207–8215.

(113) Krukau, A. V.; Vydrov, O. A.; Izmaylov, A. F.; Scuseria, G. E. Influence of the Exchange Screening Parameter

on the Performance of Screened Hybrid Functionals. *J. Chem. Phys.* **2006**, *125* (22), 224106.

(114) Singh, R.; Deb, B. M. Developments in Excited-State Density Functional Theory. *Phys. Rep.* **1999**, *311* (2), 47–94.

(115) Hedin, L. New Method for Calculating the One-Particle Green's Function with Application to the Electron-Gas Problem. *Phys. Rev.* **1965**, *139* (3A), A796–A823.

(116) Shishkin, M.; Kresse, G. Self-Consistent GW Calculations for Semiconductors and Insulators. *Phys. Rev. B - Condens. Matter Mater. Phys.* **2007**, *75* (23), 235102.

(117) Fuchs, F.; Furthmüller, J.; Bechstedt, F.; Shishkin, M.; Kresse, G. Quasiparticle Band Structure Based on a Generalized Kohn-Sham Scheme. *Phys. Rev. B - Condens. Matter Mater. Phys.* **2007**, *76* (11), 115109.

(118) Toroker, M. C.; Kanan, D. K.; Alidoust, N.; Isseroff, L. Y.; Liao, P.; Carter, E. A. First Principles Scheme to Evaluate Band Edge Positions in Potential Transition Metal Oxide Photocatalysts and Photoelectrodes. *Phys. Chem. Chem. Phys.* **2011**, *13* (37), 16644.

(119) Grüneis, A.; Kresse, G.; Hinuma, Y.; Oba, F. Ionization Potentials of Solids: The Importance of Vertex Corrections. *Phys. Rev. Lett.* **2014**, *112* (9), 096401.

(120) Hinuma, Y.; Grüneis, A.; Kresse, G.; Oba, F. Band Alignment of Semiconductors from Density-Functional Theory and Many-Body Perturbation Theory. *Phys. Rev. B* **2014**, *90* (15), 155405.

(121) Shishkin, M.; Kresse, G. Implementation and Performance of the Frequency-Dependent GW Method within the PAW Framework. *Phys. Rev. B - Condens. Matter Mater. Phys.* **2006**, *74*, 035101.

(122) Charles, K. *Introduction to Solid State Physics*, 8th ed.; John Wiley & Sons: New York, 2005.

(123) Kaviany, M. *Heat Transfer Physics*, 2nd ed.; Cambridge University Press: New York, NY, 2014.

(124) Gonze, X.; Lee, C. Dynamical Matrices, Born Effective Charges, Dielectric Permittivity Tensors, and Interatomic Force Constants from Density-Functional Perturbation Theory. *Phys. Rev. B - Condens. Matter Mater. Phys.* **1997**, *55* (16), 10355–10368.

(125) Pick, R. M.; Cohen, M. H.; Martin, R. M. Microscopic Theory of Force Constants in the Adiabatic Approximation. *Phys. Rev. B - Condens. Matter Mater. Phys.* **1970**, *1* (2), 910–920.

(126) Detraux, F.; Ghosez, P.; Gonze, X. Long-Range Coulomb Interaction in ZrO_2. *Phys. Rev. Lett.* **1998**, *81* (15), 3297.

(127) Parlinski, K.; Li, Z. Q.; Kawazoe, Y. Parlinski, Li, and Kawazoe Reply: *Phys. Rev. Lett.* **1998**, *81* (15), 3298.

(128) Maradudin, A. A.; Montroll, E. W.; Weiss, G. H. *Theory of Lattice Dynamics in the Harmonic Approximation*, 2nd ed.; Academic Press: New York, 1971.

(129) Zinenko, V. I.; Zamkova, N. G. Lattice Dynamics of Antiperovskite Structure Compounds A_3OX (A = Na, K; X = Cl, Br). *Ferroelectrics* **2002**, *265* (1), 23–29.

(130) Parlinski, K. PHONON Software. Kraków 2013.

(131) Skelton, J. M.; Tiana, D.; Parker, S. C.; Togo, A.; Tanaka, I.; Walsh, A. Influence of the Exchange-Correlation Functional on the Quasi-Harmonic Lattice Dynamics of II-VI Semiconductors. *J. Chem. Phys.* **2015**, *143* (6), 064710.

(132) Murnaghan, F. D. The Compressibility of Media under Extreme Pressures. *Proc. Natl. Acad. Sci.* **1944**, *30* (9), 244–247.

(133) Ong, S. P.; Wang, L.; Kang, B.; Ceder, G. Li−Fe−P−O_2 Phase Diagram from First Principles Calculations. *Chem. Mater.* **2008**, *20* (5), 1798–1807.

(134) Kresse, G.; Furthmüller, J. Efficient Iterative Schemes for Ab Initio Total-Energy Calculations Using a Plane-Wave Basis Set. *Phys. Rev. B - Condens. Matter Mater. Phys.* **1996**, *54* (16), 11169–11186.

(135) Blöchl, P. E. Projector Augmented-Wave Method. *Phys. Rev. B - Condens. Matter Mater. Phys.* **1994**, *50* (24), 17953–17979.

(136) Kresse, G.; Joubert, D. From Ultrasoft Pseudopotentials to the Projector Augmented-Wave Method. *Phys. Rev. B - Condens. Matter Mater. Phys.* **1999**, *59* (3), 1758–1775.

(137) Wei, S.; Chou, M. Y. Ab Initio Calculation of Force Constants and Full Phonon Dispersions. *Phys. Rev. Lett.* **1992**, *69* (19), 2799–2802.

(138) Hinuma, Y.; Oba, F.; Kumagai, Y.; Tanaka, I. Ionization Potentials of (112) and (112-) Facet Surfaces of

$CuInSe_2$ and $CuGaSe_2$. *Phys. Rev. B - Condens. Matter Mater. Phys.* **2012**, *86* (24), 245433.

(139) Wallance, D. C. *Thermodynamics of Crystals*; John Wiley & Sons: New York, 1972.

(140) Siegel, D. J.; Wolverton, C.; Ozoliņš, V. Reaction Energetics and Crystal Structure of $Li_4BN_3H_{10}$ from First Principles. *Phys. Rev. B - Condens. Matter Mater. Phys.* **2007**, *75* (1), 014101.

(141) Rogal, J. Stability, Composition and Function of Palladium Surfaces in Oxidizing Environments: A First-Principles Statistical Mechanics Approach, Freie Universität Berlin, 2006.

(142) Chase, M. W. *NIST-JANAF Thermochemical Tables*, 4th ed.; American Institute of Physics: Melville, NY, 1998.

(143) Kirklin, S.; Saal, J. E.; Meredig, B.; Thompson, A.; Doak, J. W.; Aykol, M.; Rühl, S.; Wolverton, C. The Open Quantum Materials Database (OQMD): Assessing the Accuracy of DFT Formation Energies. *npj Comput. Mater.* **2015**, *1* (1), 15010.

(144) Radin, M. D.; Rodriguez, J. F.; Tian, F.; Siegel, D. J. Lithium Peroxide Surfaces Are Metallic, While Lithium Oxide Surfaces Are Not. *J. Am. Chem. Soc.* **2012**, *134* (2), 1093–1103.

(145) Shishkin, M.; Marsman, M.; Kresse, G. Accurate Quasiparticle Spectra from Self-Consistent GW Calculations with Vertex Corrections. *Phys. Rev. Lett.* **2007**, *99* (24), 246403.

(146) Chen, H. M.; Maohua, C.; Adams, S. Stability and Ionic Mobility in Argyrodite-Related Lithium-Ion Solid Electrolytes. *Phys. Chem. Chem. Phys.* **2015**, *17* (25), 16494–16506.

(147) Zhu, H.; Aindow, M.; Ramprasad, R. Stability and Work Function of TiC_xN_{1-x} Alloy Surfaces: Density Functional Theory Calculations. *Phys. Rev. B - Condens. Matter Mater. Phys.* **2009**, *80* (20), 201406(R).

(148) Zucker, R. V.; Chatain, D.; Dahmen, U.; Hagege, S.; Carter, W. C. New Software Tools for the Calculation and Display of Isolated and Attached Interfacial-Energy Minimizing Particle Shapes. *J. Mater. Sci.* **2012**, *47* (24), 8290–8302.

(149) Smith, J. R.; Hong, T.; Srolovitz, D. J. Metal-Ceramic Adhesion and the Harris Functional. *Phys. Rev. Lett.* **1994**, *72* (25), 4021–4024.

(150) Seriani, N. Ab Initio Thermodynamics of Lithium Oxides : From Bulk Phases to Nanoparticles. *Nanotechnology* **2009**, *20* (44), 445703.

(151) Jäckle, M.; Groß, A. Microscopic Properties of Lithium, Sodium, and Magnesium Battery Anode Materials Related to Possible Dendrite Growth. *J. Chem. Phys.* **2014**, *141* (17), 174710.

(152) Liu, Z.; Qi, Y.; Lin, Y. X.; Chen, L.; Lu, P.; Chen, L. Q. Interfacial Study on Solid Electrolyte Interphase at Li Metal Anode: Implication for Li Dendrite Growth. *J. Electrochem. Soc.* **2016**, *163* (3), A592–A598.

(153) Wang, Y.; Liu, Z. K.; Chen, L. Q.; Wolverton, C. First-Principles Calculations of B″-Mg_5Si_6/α-Al Interfaces. *Acta Mater.* **2007**, *55* (17), 5934–5947.

(154) Yuan, Y.; Lee, T. R. Surface Science Techniques. In *Surface Science Techniques*; Bracco, G., Holst, B., Eds.; Springer Series in Surface Sciences; Springer: Berlin, Heidelberg, 2013; Vol. 51, pp 3–34.

(155) Young, T. An Essay on the Cohesion of Fluids. *Philos. Trans. R. Soc. London* **1805**, *95*, 65–87.

(156) Borodin, O.; Behl, W.; Jow, T. R. Oxidative Stability and Initial Decomposition Reactions of Carbonate, Sulfone, and Alkyl Phosphate-Based Electrolytes. *J. Phys. Chem. C* **2013**, *117* (17), 8661–8682.

(157) Yu, S. Atomic Scale Simulations of the Solid Electrolyte $Li_7La_3Zr_2O_{12}$., University of Michigan, Ann Arbor, MI, 2018.

(158) Hoffmann, R. Solids and Surfaces: A Chemist's View of Bonding in Extended Structures. VCH Publishers: New York, NY 1988.

(159) Levy, M. R.; Grimes, R. W.; Sickafus, K. E. Disorder Processes in $A^{3+}B^{3+}O_3$ Compounds: Implications for Radiation Tolerance. *Philos. Mag.* **2004**, *84* (6), 533–545.

(160) Goldschmidt, V. M. Die Gesetze Der Krystallochemie. *Naturwissenschaften* **1926**, *14* (21), 477–485.

(161) Tilley, R. J. D. *Perovskites: Structure-Property Relationships*; John Wiley & Sons: Chichester, West Sussex, 2016.

(162) Lufaso, M. W. Perovskite Synthesis and Analysis Using Structure Prediction Diagnostic Software. Ph.D. Thesis, Ohio State University, Columbus, OH, 2002.

(163) Hines, R. I. Atomistic Simulation and Ab-Initio Studies of Polar Solids. Ph.D. Thesis, University of Bristol,

Bristol, UK, 1997.

(164) Levy, M. R. Crystal Structure and Defect Property Predictions in Ceramic Materials. Ph.D. Thesis, University of London, London, UK, 2005.

(165) Yokokawa, H.; Sakai, N.; Kawada, T.; Dokiya, M. Thermodynamic Stabilities of Perovskite Oxides for Electrodes and Other Electrochemical Materials. *Solid State Ionics* **1992**, *52* (1–3), 43–56.

(166) Kreuer, K. D. On the Development of Proton Conducting Materials for Technological Applications. *Solid State Ionics* **1997**, *97* (1–4), 1–15.

(167) Nagabhushana, G. P.; Shivaramaiah, R.; Navrotsky, A. Direct Calorimetric Verification of Thermodynamic Instability of Lead Halide Hybrid Perovskites. *Proc. Natl. Acad. Sci.* **2016**, *113* (28), 7717–7721.

(168) Jónsson, H.; Mills, G.; Jacobsen, K. W. Nudged Elastic Band Method for Finding Minimum Energy Paths of Transitions. In *Classical and Quantum Dynamics in Condensed Phase Simulations*; Berne, B. J., Ciccotti, G., Coker, D. F., Eds.; World Scientific: Singapore, 1998; pp 385–404.

(169) Henkelman, G.; Jónsson, H. Improved Tangent Estimate in the Nudged Elastic Band Method for Finding Minimum Energy Paths and Saddle Points. *J. Chem. Phys.* **2000**, *113* (22), 9978–9985.

(170) Aidhy, D. S.; Wolverton, C. First-Principles Prediction of Phase Stability and Crystal Structures in Li-Zn and Na-Zn Mixed-Metal Borohydrides. *Phys. Rev. B - Condens. Matter Mater. Phys.* **2011**, *83* (14), 144111.

(171) Schmidt, J.; Shi, J.; Borlido, P.; Chen, L.; Botti, S.; Marques, M. A. L. Predicting the Thermodynamic Stability of Solids Combining Density Functional Theory and Machine Learning. *Chem. Mater.* **2017**, *29* (12), 5090–5103.

(172) Ong, S. P.; Jain, A.; Hautier, G.; Kang, B.; Ceder, G. Thermal Stabilities of Delithiated Olivine MPO_4 (M=Fe, Mn) Cathodes Investigated Using First Principles Calculations. *Electrochem. commun.* **2010**, *12* (3), 427–430.

(173) Ong, S. P.; Richards, W. D.; Jain, A.; Hautier, G.; Kocher, M.; Cholia, S.; Gunter, D.; Chevrier, V. L.; Persson, K. A.; Ceder, G. Python Materials Genomics (Pymatgen): A Robust, Open-Source Python Library for Materials Analysis. *Comput. Mater. Sci.* **2013**, *68*, 314–319.

(174) Lindemann, F. A. The Calculation of Molecular Vibration Frequencies. *Phys. Z.* **1910**, *11*, 609–612.

(175) Pines, D. *Elementary Excitations in Solids*; CRC Press: Boca Raton, 2018.

(176) Anderson, O. L. A Simplified Method for Calculating the Debye Temperature from Elastic Constants. *J. Phys. Chem. Solids* **1963**, *24* (7), 909–917.

(177) Schreiber, E.; Anderson, O. L.; Soga, N. *Elastic Constants and Their Measurements*; McGraw-Hill: New York, 1973.

(178) Voigt, W. *Lehrbuch Der Kristallphysik*; Taubner: Leipzig, 1928.

(179) Reuss, A. Berechnung Der Fließgrenze von Mischkristallen Auf Grund Der Plastizitätsbedingung Für Einkristalle. *ZAMM - J. Appl. Math. Mech. / Zeitschrift für Angew. Math. und Mech.* **1929**, *9* (1), 49–58.

(180) Ravindran, P.; Fast, L.; Korzhavyi, P. A.; Johansson, B.; Wills, J.; Eriksson, O. Density Functional Theory for Calculation of Elastic Properties of Orthorhombic Crystals: Application to $TiSi_2$. *J. Appl. Phys.* **1998**, *84* (9), 4891.

(181) Sitta, S.; Hippler, K.; Vogt, P.; Sabrowsky, H. Kristallstruktur von Gelbem K_3OBr. *Zeitschrift für Anorg. und Allg. Chemie* **1991**, *597* (1), 197–200.

(182) Sitta, S.; Hippler, K.; Vogt, P.; Sabrowsky, H. Crystal Structure of K_3OI. *Zeitschrift für Krist.* **1991**, *196* (1–4), 193–196.

(183) Sabrowsky, H.; Feldbaum-Moller, E.; Fischer, K.; Sitta, S.; Vogt, P.; Winter, V. Die Kristallstrukturen von α- Und β-K_3OCl. *Zeitschrift für Anorg. und Allg. Chemie* **1996**, *622*, 153–156.

(184) Yashima, M.; Ali, R. Structural Phase Transition and Octahedral Tilting in the Calcium Titanate Perovskite $CaTiO_3$. *Solid State Ionics* **2009**, *180* (2–3), 120–126.

(185) Munoz, A.; Alonso, J. A.; Martínez-Lope, M. J.; Casáis, M. T.; Ferna, M. T.; Martínez, J. L.; Fernández-Díaz, M. T. Evolution of the Magnetic Structure of Hexagonal $HoMnO_3$ from Neutron Powder Diffraction Data. *Chem. Mater.* **2001**, *13* (5), 1497–1505.

(186) Bréard, Y.; Fjellvåg, H.; Hauback, B. Investigation of Bixbyite Type Scandium Oxides Involving a Magnetic Cation: $Sc_{2-x}Fe_xO_3$ ($0 \leq x \leq 1$). *Solid State Commun.* **2011**, *151* (3), 223–226.

(187) Shannon, R. D. Revised Effective Ionic Radii and Systematic Studies of Interatomic Distances in Halides and

Chalcogenides. *Acta Crystallogr. Sect. A* **1976**, *32* (5), 751–767.

(188) He, X.; Zhu, Y.; Mo, Y. Origin of Fast Ion Diffusion in Super-Ionic Conductors. *Nat. Commun.* **2017**, *8*, 1–7.

(189) Rayavarapu, P. R.; Sharma, N.; Peterson, V. K.; Adams, S. Variation in Structure and Li^+-Ion Migration in Argyrodite-Type Li_6PS_5X (X = Cl, Br, I) Solid Electrolytes. *J. Solid State Electrochem.* **2012**, *16* (5), 1807–1813.

(190) Dietrich, C.; Weber, D.; Sedlmaier, S. J.; Indris, S.; Culver, S.; Walter, D.; Janek, J.; Zeier, W. Lithium Ion Conductivity in Li_2S-P_2S_5 Glasses – Building Units and Local Structure Evolution during the Crystallization of the Superionic Conductors Li_3PS_4, $Li_7P_3S_{11}$ A. *J. Mater. Chem. A* **2017**, *5* (34), 18111–18119.

(191) Yu, S.; Siegel, D. J. Grain Boundary Contributions to Li-Ion Transport in the Solid Electrolyte Li7La3Zr2O12 (LLZO). *Chem. Mater.* **2017**, *29* (22), 9639–9647.

(192) Hull, S.; Keen, D. A.; Gardner, N. J. G.; Hayes, W. The Crystal Structures of Superionic Ag_3SI. *J. Phys. Condens. Matter* **2001**, *13* (10), 2295–2316.

(193) Kagawa, F.; Oike, H. Quenching of Charge and Spin Degrees of Freedom in Condensed Matter. *Adv. Mater.* **2017**, *29* (25), 1601979.

(194) Jansen, M. Volume Effect or Paddle-Wheel Mechanism - Fast Alkali-Metal Ionic Conduction in Solids with Rotationally Disordered Complex Anions. *Angew. Chemie Int. Ed. English* **1991**, *30* (12), 1547–1558.

(195) Schmidt, J.; Shi, J.; Borlido, P.; Chen, L.; Botti, S.; Marques, M. A. L. Predicting the Thermodynamic Stability of Solids Combining Density Functional Theory and Machine Learning. *Chem. Mater.* **2017**, *29* (12), 5090–5103.

(196) Deng, D. Li-Ion Batteries: Basics, Progress, and Challenges. *Energy Sci. Eng.* **2015**, *3* (5), 385–418.

(197) Wang, Z.; Selbach, S. M.; Grande, T. Van Der Waals Density Functional Study of the Energetics of Alkali Metal Intercalation in Graphite. *RSC Adv.* **2014**, *4* (8), 4069–4079.

(198) Xu, Z.; Lv, X.; Chen, J.; Jiang, L.; Lai, Y.; Li, J. Dispersion-Corrected DFT Investigation on Defect Chemistry and Potassium Migration in Potassium-Graphite Intercalation Compounds for Potassium Ion Batteries Anode Materials. *Carbon N. Y.* **2016**, *107*, 885–894.

(199) Moriwake, H.; Kuwabara, A.; Fisher, C. A. J.; Ikuhara, Y. Why Is Sodium-Intercalated Graphite Unstable? *RSC Adv.* **2017**, *7* (58), 36550–36554.

(200) Kim, H.; Yoon, G.; Lim, K.; Kang, K. A Comparative Study of Graphite Electrodes Using the Co-Intercalation Phenomenon for Rechargeable Li, Na and K Batteries. *Chem. Commun.* **2016**, *52* (85), 12618–12621.

(201) Kim, H. The 2018 Colin Garfield Fink Postdoctoral Summer Fellowship – Summary Report: Investigation of Alkali Ion (Li, Na, and K) Intercalation in K_xVPO_4F Host Material. *Electrochem. Soc. Interface* **2018**, *27* (4), 78–79.

(202) Komaba, S.; Hasegawa, T.; Dahbi, M.; Kubota, K. Potassium Intercalation into Graphite to Realize High-Voltage/High-Power Potassium-Ion Batteries and Potassium-Ion Capacitors. *Electrochem. commun.* **2015**, *60*, 172–175.

(203) Lei, K.; Li, F.; Mu, C.; Wang, J.; Zhao, Q.; Chen, C.; Chen, J. High K-Storage Performance Based on the Synergy of Dipotassium Terephthalate and Ether-Based Electrolytes. *Energy Environ. Sci.* **2017**, *10* (2), 552–557.

(204) Okoshi, M.; Yamada, Y.; Komaba, S.; Yamada, A.; Nakai, H. Theoretical Analysis of Interactions between Potassium Ions and Organic Electrolyte Solvents: A Comparison with Lithium, Sodium, and Magnesium Ions. *J. Electrochem. Soc.* **2017**, *164* (2), A54–A60.

(205) Yoshinari, N.; Yamashita, S.; Fukuda, Y.; Nakazawa, Y.; Konno, T. Mobility of Hydrated Alkali Metal Ions in Metallosupramolecular Ionic Crystals. *Chem. Sci.* **2019**, *10* (2), 587–593.

(206) Köhler, U.; Herzig, C. On the Correlation between Self-Diffusion and the Low-Frequency LA ⅔ ⟨ 111 ⟩ Phonon Mode in b . c . c . Metals. *Philos. Mag. A* **1988**, *58* (5), 769–786.

(207) Pearson, E. W.; Jackson, M. D.; Gordon, R. G. A Theoretical Model for the Index of Refraction of Simple Ionic Crystals. *J. Phys. Chem.* **1984**, *88* (1), 119–128.

(208) Kim, K.; Siegel, D. J. Correlating Lattice Distortions, Ion Migration Barriers, and Stability in Solid Electrolytes. *J. Mater. Chem. A* **2019**, *7* (7), 3216–3227.

(209) Shanker, J.; Agrawal, S. C. Electronic Polarizabilities and Sizes of Ions in Alkaline Earth Halides and Alkali

Chalcogenides. *J. Phys. Chem. Solids* **1980**, *41* (3), 209–213.

(210) Mahan, G. D.; Subbaswamy, K. R. *Local Density Theory of Polarizability*; Springer US: Boston, MA, 1990.

(211) Bader, R. F. W. *Atoms in Molecules: A Quantum Theory*; Oxford University Press: New York, 1990.

(212) Henkelman, G.; Arnaldsson, A.; Jónsson, H. A Fast and Robust Algorithm for Bader Decomposition of Charge Density. *Comput. Mater. Sci.* **2006**, *36* (3), 354–360.

(213) Sanville, E.; Kenny, S. D.; Smith, R.; Henkelman, G. Improved Grid-Based Algorithm for Bader Charge Allocation. *J. Comput. Chem.* **2007**, *28* (5), 899–908.

(214) Tang, W.; Sanville, E.; Henkelman, G. A Grid-Based Bader Analysis Algorithm without Lattice Bias. *J. Phys. Condens. Matter* **2009**, *21* (8), 084204.

(215) Yu, M.; Trinkle, D. R. Accurate and Efficient Algorithm for Bader Charge Integration. *J. Chem. Phys.* **2011**, *134* (6), 064111.

(216) Lewis, G. N. *Valence and the Structure of Atoms and Molecules*; The Chemical Catalog Company, inc.: New York, 1923.

(217) Aniya, M. A Chemical Approach for the Microscopic Mechanism of Fast Ion Transport in Solids. *Solid State Ionics* **1992**, *50* (1–2), 125–129.

(218) Aniya, M. Superionicity as a Local Fluctuation of the Chemical Bond. *Solid State Ionics* **1994**, *70–71* (1), 673–677.

(219) Aniya, M.; Shimojo, F. Coupled Motions of Ions and Electrons in Some Superionic Conductors: An Ab Initio Molecular Dynamics Study. *Solid State Ionics* **2006**, *177* (19–25), 1567–1572.

(220) Wood, B. C.; Marzari, N. Dynamical Structure, Bonding, and Thermodynamics of the Superionic Sublattice in ?-AgI. *Phys. Rev. Lett.* **2006**, *97* (16), 166401.

(221) Adelstein, N.; Wood, B. C. Role of Dynamically Frustrated Bond Disorder in a Li^+ Superionic Solid Electrolyte. *Chem. Mater.* **2016**, *28* (20), 7218–7231.

(222) Hornebecq, V.; Réau, J.-M.; Villesuzanne, A.; Elissalde, C.; Ravez, J. Ionic Conductivity, Ferroelectricity and Chemical Bonding in TKWB Type Ceramics of the $K_6Li_4Ta_{10}O_{30}$-$Pb_5Ta_{10}O_{30}$ System. *J. Mater. Chem.* **1998**, *8* (11), 2423–2428.

(223) Liu, Y.; Zhao, T.; Ju, W.; Shi, S.; Shi, S.; Shi, S. Materials Discovery and Design Using Machine Learning. *J. Mater.* **2017**, *3* (3), 159–177.

(224) Kim, C.; Pilania, G.; Ramprasad, R. From Organized High-Throughput Data to Phenomenological Theory Using Machine Learning: The Example of Dielectric Breakdown. *Chem. Mater.* **2016**, *28* (5), 1304–1311.

(225) Attarian Shandiz, M.; Gauvin, R. Application of Machine Learning Methods for the Prediction of Crystal System of Cathode Materials in Lithium-Ion Batteries. *Comput. Mater. Sci.* **2016**, *117*, 270–278.

(226) Zhuo, Y.; Mansouri Tehrani, A.; Brgoch, J. Predicting the Band Gaps of Inorganic Solids by Machine Learning. *J. Phys. Chem. Lett.* **2018**, *9* (7), 1668–1673.

(227) Cao, L.; Zhu, P.; Zhao, Y.; Zhao, J. Using Machine Learning and Quantum Chemistry Descriptors to Predict the Toxicity of Ionic Liquids. *J. Hazard. Mater.* **2018**, *352*, 17–26.

(228) Petrich, L.; Westhoff, D.; Feinauer, J.; Finegan, D. P.; Daemi, S. R.; Shearing, P. R.; Schmidt, V. Crack Detection in Lithium-Ion Cells Using Machine Learning. *Comput. Mater. Sci.* **2017**, *136*, 297–305.

(229) Balachandran, P. V.; Emery, A. A.; Gubernatis, J. E.; Lookman, T.; Wolverton, C.; Zunger, A. Predictions of New ABO_3 Perovskite Compounds by Combining Machine Learning and Density Functional Theory. *Phys. Rev. Mater.* **2018**, *2* (4), 043802.

(230) Artrith, N.; Urban, A.; Ceder, G. Constructing First-Principles Phase Diagrams of Amorphous Li_xSi Using Machine-Learning-Assisted Sampling with an Evolutionary Algorithm. *J. Chem. Phys.* **2018**, *148* (24).

(231) Zeng, Y.; Li, Q.; Bai, K. Prediction of Interstitial Diffusion Activation Energies of Nitrogen, Oxygen, Boron and Carbon in Bcc, Fcc, and Hcp Metals Using Machine Learning. *Comput. Mater. Sci.* **2018**, *144*, 232–247.

(232) Amsler, M.; Ward, L.; Hegde, V. I.; Goesten, M. G.; Yi, X.; Wolverton, C. Ternary Mixed-Anion Semiconductors with Tunable Band Gaps from Machine-Learning and Crystal Structure Prediction. *Phys. Rev. Mater.* **2019**, *3* (3), 035404.

(233) Fujimura, K.; Seko, A.; Koyama, Y.; Kuwabara, A.; Kishida, I.; Shitara, K.; Fisher, C. A. J.; Moriwake, H.; Tanaka, I. Accelerated Materials Design of Lithium Superionic Conductors Based on First-Principles

Calculations and Machine Learning Algorithms. *Adv. Energy Mater.* **2013**, *3* (8), 980–985.

(234) Jalem, R.; Nakayama, M.; Kasuga, T. An Efficient Rule-Based Screening Approach for Discovering Fast Lithium Ion Conductors Using Density Functional Theory and Artificial Neural Networks. *J. Mater. Chem. A* **2014**, *2* (3), 720–734.

(235) Jalem, R.; Kimura, M.; Nakayama, M.; Kasuga, T. Informatics-Aided Density Functional Theory Study on the Li Ion Transport of Tavorite-Type $LiMTO_4F$ (M^{3+}-T^{5+}, M^{2+}-T^{6+}). *J. Chem. Inf. Model.* **2015**, *55* (6), 1158–1168.

(236) Kireeva, N.; Pervov, V. S. Materials Space of Solid-State Electrolytes: Unraveling Chemical Composition-Structure-Ionic Conductivity Relationships in Garnet-Type Metal Oxides Using Cheminformatics Virtual Screening Approaches. *Phys. Chem. Chem. Phys.* **2017**, *19* (31), 20904–20918.

(237) Kohavi, R.; John, G. H. Wrappers for Feature Subset Selection. *Artif. Intell.* **1997**, *97* (1–2), 273–324.

(238) Pedregosa, F.; Varoquaux, G.; Gramfort, A.; Michel, V.; Thirion, B.; Grisel, O.; Blondel, M.; Prettenhofer, P.; Weiss, R.; Dubourg, V.; et al. Scikit-Learn: Machine Learning in Python. *J. Mach. Learn. Res.* **2011**, *12*, 2825–2830.

(239) Rodgers, J. L.; Nicewander, W. A. Thirteen Ways to Look at the Correlation Coefficient. *Am. Stat.* **1988**, *42* (1), 59–66.

(240) Hoerl, A. E.; Kennard, R. W. Ridge Regression: Biased Estimation for Nonorthogonal Problems. *Technometrics* **1970**, *12* (1), 55–67.

(241) Tibshirani, R. Regression Shrinkage and Selection via the Lasso. *J. R. Stat. Soc. Ser. B (Statistical Methodol.* **1996**, *58* (1), 267–288.

(242) Zou, H.; Hastie, T. Regression and Variable Selection via the Elastic Net. *J. R. Stat. Soc. Ser. B (Statistical Methodol.* **2005**, *67* (2), 301–320.

(243) Bishop, C. M. *Pattern Recognition and Machine Learning*; Springer: New York, NY, 2006.

(244) Mackay, D. J. C. Bayesian Methods for Backpropagation Networks. In *Models of Neural Networks III*; Domany, E., van Hemmen, J. L., Schulten, K., Eds.; Springer, 1994; pp 211–254.

(245) Huber, P. J. Robust Estimation of a Location Parameter. *Ann. Math. Stat.* **1964**, *35* (1), 73–101.

(246) Crammer, K.; Dekel, O.; Keshet, J.; Shalev-Shwartz, S.; Singer, Y. Online Passive-Aggressive Algorithms. *J. Mach. Learn. Res.* **2006**, *7*, 551–585.

(247) Drucker, H.; Burges, C. J. C.; Kaufman, L.; Smola, A.; Vapnik, V. Support Vector Regression Machines. In *Neural Information Processing Systems*; Mozer, M. C., Joradn, J. I., Petsche, T., Eds.; MIT Press: Cambridge, MA, 1997; Vol. 9, pp 155–161.

(248) Chang, C.-C.; Lin, C.-J. LIBSVM: A Library for Support Vector Machines. *ACM Trans. Intell. Syst. Technol.* **2011**, *2* (3), 27.

(249) Fan, R.-E.; Chang, K.-W.; Hsieh, C.-J.; Wang, X.-R.; Lin, C.-J. LIBLINEAR: A Library for Large Linear Classification. *J. Mach. Learn. Res.* **2008**, *9*, 1871–1874.

(250) Schölkopf, B.; Smola, A. J.; Williamson, R. C.; Bartlett, P. L. New Support Vector Algorithms. *Neural Comput.* **2000**, *12*, 1207–1245.

(251) Breiman, L.; Friedman, J. H.; Olshen, R. A.; Stone, C. J. *Classification and Regression Trees*; Chapman and Hall/CRC: Boca Raton, FL, 1984.

(252) Bramer, M. *Principles of Data Mining*, 2nd ed.; Springer-Verlag: London, 2007.

(253) Breiman, L. Bagging Predictors. *Mach. Learn.* **1996**, *24* (2), 123–140.

(254) Tin Kam Ho. Random Decision Forests. In *Proceedings of 3rd International Conference on Document Analysis and Recognition*; IEEE Comput. Soc. Press, 1995; Vol. 1, pp 278–282.

(255) Breiman, L. Random Forests. *Mach. Learn.* **2001**, *45* (1), 5–32.

(256) Geurts, P.; Ernst, D.; Wehenkel, L. Extremely Randomized Trees. *Mach. Learn.* **2006**, *63* (1), 3–42.

(257) Freund, Y.; Schapire, R. E. A Decision-Theoretic Generalization of On-Line Learning and an Application to Boosting. *J. Comput. Syst. Sci.* **1997**, *55* (1), 119–139.

(258) Drucker, H. Improving Regressors Using Boosting Techniques. In *Proceedings of the 14th International Conference on Machine Learning*; 1997; pp 107–115.

(259) Friedman, J. H. . Greedy Function Approximation: A Gradient Boosting Machine. *Ann. Stat.* **2001**, *29* (5), 1189–1232.

(260) Kohavi, R. A Study of Cross-Validation and Bootstrap for Accuracy Estimation and Model Selection. *Proc. 14th Int. Jt. Conf. Artif. Intell.* **1995**, *2*, 1137–1143.

(261) Goldstein, A.; Kapelner, A.; Bleich, J.; Pitkin, E. Peeking Inside the Black Box: Visualizing Statistical Learning With Plots of Individual Conditional Expectation. *J. Comput. Graph. Stat.* **2015**, *24* (1), 44–65.

(262) PDPbox. *GitHub* (https://github.com/SauceCat/PDPbox), Accessed June 13, 2019.

(263) Theodoridis, S.; Koutroumbas, K. *Pattern Recognition*, 4th ed.; Academin Press: Burlington, MA, 2008.

(264) Roy, K.; Kar, S.; Das, R. N. *A Primer on QSAR/QSPR Modeling*; SpringerBriefs in Molecular Science; Springer International Publishing: Cham, 2015.

(265) Coursey, J. S.; Schwab, D. J.; Tsai, J. J.; Dragoset, R. A. *Atomic Weights and Isotopic Compositions with Relative Atomic Masses*; National Institute of Standards and Technology (NIST) Physical Measurement Laboratory, 2015.

(266) Pauling, L. THE NATURE OF THE CHEMICAL BOND. IV. THE ENERGY OF SINGLE BONDS AND THE RELATIVE ELECTRONEGATIVITY OF ATOMS. *J. Am. Chem. Soc.* **1932**, *54* (9), 3570–3582.

(267) Allred, A. L. Electronegativity Values from Thermochemical Data. *J. Inorg. Nucl. Chem.* **1961**, *17* (3–4), 215–221.

(268) Willems, T. F.; Rycroft, C. H.; Kazi, M.; Meza, J. C.; Haranczyk, M. Algorithms and Tools for High-Throughput Geometry-Based Analysis of Crystalline Porous Materials. *Microporous Mesoporous Mater.* **2012**, *149* (1), 134–141.

(269) Van de Walle, C. G.; Neugebauer, J. First-Principles Calculations for Defects and Impurities: Applications to III-Nitrides. *J. Appl. Phys.* **2004**, *95* (8), 3851–3879.

(270) Wadati, H.; Maniwa, A.; Chikamatsu, A.; Kumigashira, H.; Oshima, M.; Mizokawa, T.; Fujimori, A.; Sawatzky, G. A. Madelung Potentials and Covalency Effect in Strained $La_{1-x}Sr_xMnO_3$ Thin Films Studied by Core-Level Photoemission Spectroscopy. *Phys. Rev. B - Condens. Matter Mater. Phys.* **2009**, *80* (12), 125107.

(271) Takahashi, T.; Nomura, E.; Yamamoto, O. Solid State Ionics. High Ionic Conductivity Solid in Silver Halide-Silver Sulphate System. *J. Appl. Electrochem.* **1972**, *2* (1), 51–57.

(272) Aboagye, J. K.; Friauf, R. J. Anomalous High-Temperature Ionic Conductivity in the Silver Halides. *Phys. Rev. B* **1975**, *11* (4), 1654–1664.

(273) Dreyfus, R. W.; Nowick, A. S. Ionic Conductivity of Doped NaCl Crystals. *Phys. Rev.* **1962**, *126* (4), 1367–1377.

(274) Hoshino, H.; Shimoji, M. Ionic Conductivity of Potassium Bromide and Sodium Bromide Crystal Coloured with Bromine. *J. Phys. Chem. Solids* **1971**, *32* (2), 385–393.

(275) Grammatikakis, J. Measurements of the Ionic Conductivity of NaI and Calculation of the Bulk Modulus and Specific Heat of Vacancies. *Phys. Status Solidi* **1982**, *113* (2), 721–726.

(276) Yung-Fang Yu Yao; Kummer, J. T. Ion Exchange Properties of and Rates of Ionic Diffusion in Beta-Alumina. *J. Inorg. Nucl. Chem.* **1967**, *29* (9), 2453–2475.

(277) Lu, X.; Bowden, M. E.; Sprenkle, V. L.; Liu, J. A Low Cost, High Energy Density, and Long Cycle Life Potassium-Sulfur Battery for Grid-Scale Energy Storage. *Adv. Mater.* **2015**, *27* (39), 5915–5922.

(278) Yuan, H.; Li, H.; Zhang, T.; Li, G.; He, T.; Du, F.; Feng, S. A $K_2Fe_4O_7$ Superionic Conductor for All-Solid-State Potassium Metal Batteries. *J. Mater. Chem. A* **2018**, *6* (18), 8413–8418.

(279) Aubrey, M. L.; Ameloot, R.; Wiers, B. M.; Long, J. R. Metal-Organic Frameworks as Solid Magnesium Electrolytes. *Energy Environ. Sci.* **2014**, *7* (2), 667–671.

(280) Genier, F. S.; Burdin, C. V.; Biria, S.; Hosein, I. D. A Novel Calcium-Ion Solid Polymer Electrolyte Based on Crosslinked Poly(Ethylene Glycol) Diacrylate. *J. Power Sources* **2019**, *414* (28), 302–307.

(281) Wang, J.; Genier, F. S.; Li, H.; Biria, S.; Hosein, I. D. A Solid Polymer Electrolyte from Cross-Linked Polytetrahydrofuran for Calcium Ion Conduction. *ACS Appl. Polym. Mater.* **2019**, *1* (7), 1837–1844.

(282) He, T.; Huang, Q.; Ramirez, A. P.; Wang, Y.; Regan, K. A.; Rogado, N.; Hayward, M. A.; Haas, M. K.; Slusky, J. S.; Inumara, K.; et al. Superconductivity in the Non-Oxide Perovskite MgCNi3. *Nature* **2001**, *411*, 54–56.

(283) Cao, W. H.; He, B.; Liao, C. Z.; Yang, L. H.; Zeng, L. M.; Dong, C. Preparation and Properties of Antiperovskite-Type Nitrides: $InNNi_3$ and $InNCo_3$. *J. Solid State Chem.* **2009**, *182* (12), 3353–3357.

(284) Bilal, M.; Jalali-Asadabadi, S.; Ahmad, R.; Ahmad, I. Electronic Properties of Antiperovskite Materials from State-of-the-Art Density Functional Theory. *J. Chem.* **2015**, 495131.

(285) Kirchner, M.; Schnelle, W.; Wagner, F. R.; Niewa, R. Preparation, Crystal Structure and Physical Properties of Ternary Compounds $(R_3N)In$, R = Rare-Earth Metal. *Solid State Sci.* **2003**, *5* (9), 1247–1257.

(286) Velden, A.; Jansen, M. Zur Kenntnis Der Inversen Perowskite M_3TO (M = Ca, Sr, Yb; T = Si, Ge, Sn, Pb). *Zeitschrift fur Anorg. und Allg. Chemie* **2004**, *630* (2), 234–238.

(287) Okamoto, Y.; Sakamaki, A.; Takenaka, K. Thermoelectric Properties of Antiperovskite Calcium Oxides Ca3PbO and Ca3SnO. *J. Appl. Phys.* **2016**, *119* (20), 1–6.

(288) Chen, K.; Li, C.; Hu, M.; Hou, X.; Li, C.; Chen, Z. Deformation Modes and Anisotropy of Anti-Perovskite Ti3AN (A = Al, In and Tl) from First-Principle Calculations. *Materials (Basel).* **2017**, *10* (4), 362.

(289) Quintela, C. X.; Campbell, N.; Shao, D. F.; Irwin, J.; Harris, D. T.; Xie, L.; Anderson, T. J.; Reiser, N.; Pan, X. Q.; Tsymbal, E. Y.; et al. Epitaxial Thin Films of Dirac Semimetal Antiperovskite Cu_3PdN. *APL Mater.* **2017**, *5* (9), 096103.

(290) Suetsugu, S.; Hayama, K.; Rost, A. W.; Nuss, J.; Mühle, C.; Kim, J.; Kitagawa, K.; Takagi, H. Magnetotransport in Sr3PbO Antiperovskite. *Phys. Rev. B* **2018**, *98* (11), 115203.

(291) Hausmann, J. N.; Oudah, M.; Ikeda, A.; Yonezawa, S.; Maeno, Y. Controlled Synthesis of the Antiperovskite Oxide Superconductor Sr3-XSnO. *Supercond. Sci. Technol.* **2018**, *31* (5), 055012.

(292) Benmalem, Y.; Abbad, A.; Benstaali, W.; Bentounes, H. A.; Seddik, T.; Lantri, T. Thermoelectric, Electronic and Structural Properties of $CuNMn_3$ Cubic Antiperovskite. *J. Comput. Electron.* **2018**, *17* (3), 881–887.

(293) Chern, M. Y.; Vennos, D. A.; Disalvo, F. J. Synthesis, Structure, and Properties of Anti-Perovskite Nitrides Ca_3MN, M = P, As, Sb, Bi, Ge, Sn, and Pb. *J. Solid State Chem.* **1992**, *96* (2), 415–425.

(294) Chi, E. O.; Kim, W. S.; Hur, N. H.; Jung, D. New Mg-Based Antiperovskites $PnNMg_3$ (Pn = As, Sb). *Solid State Commun.* **2002**, *121* (6–7), 309–312.

(295) Amara, K.; Zemouli, M.; Elkeurti, M.; Belfedal, A.; Saadaoui, F. First-Principles Study of $XNMg_3$ (X = P, As, Sb and Bi) Antiperovskite Compounds. *J. Alloys Compd.* **2013**, *576*, 398–403.

(296) Goh, W. F.; Pickett, W. E. Survey of the Class of Isovalent Antiperovskite Alkaline-Earth Pnictide Compounds. *Phys. Rev. B* **2018**, *97* (3), 35202.

(297) Chern, M. Y.; Disalvo, F. J.; Parise, J. B.; Goldstone, J. A. The Structural Distortion of the Anti-Perovskite Nitride Ca_3AsN. *J. Solid State Chem.* **1992**, *96* (2), 426–435.

(298) Emsley, J. *The Elements*, 3rd ed.; Oxford University Press: New York, 1998.

(299) Sreedevi, P. D.; Ravindran, P.; Vidya, R. First Principles Prediction of the Ground State Crystal Structures of Antiperovskite Compounds A_3PN (A= Be, Mg, Ca, Sr, Ba and Zn). *Mater. Today Proc.* **2019**, *8*, 294–300.

(300) Samsonov, G. V. *Handbook of the Physicochemical Properties of the Elements*; IFI-Plenum: New York, 1968.

(301) Kaye, G. W. C.; Laby, T. H. *Tables of Physical and Chemical Constants*, 15th ed.; Longman: London, 1993.

(302) Yu, S.; Siegel, D. J. Grain Boundary Softening: A Potential Mechanism for Lithium Metal Penetration through Stiff Solid Electrolytes. *ACS Appl. Mater. Interfaces* **2018**, *10* (44), 38151–38158.

(303) Rumble, J. R. *CRC Handbook of Chemistry and Physics*, 99th ed.; CRC Press: Boca Raton, 2018.